The Henryk Niewodniczański

INSTITUTE OF NUCLEAR PHYSICS

Polish Academy of Sciences

Kraków

April 2016

„Study of the Pygmy Dipole Resonances Using High-Resolution Gamma Spectrometers”

mgr inż. Mateusz Krzysiek

PhD thesis written under the supervision of

dr hab. Piotr Bednarczyk, prof. IFJ PAN

co-supervisor: dr hab. Maria Kmiecik, prof. IFJ PAN

CONTENTS

ABSTRACT

The excitation spectrum of atomic nucleus is, at high energies, dominated by the Giant Dipole Resonance (GDR), which is a collective oscillation of almost all neutrons vs. protons. Around neutron separation energy, well below the GDR, the presence of low-lying dipole strength have been reported in many nuclei and associated to so called Pygmy Dipole Resonance (PDR). In most simple picture it is interpreted as an oscillation of the excess neutrons forming the neutron-skin versus isospin saturated core of the nucleus. Many microscopic calculations have shown the relationship between the PDR strength and the neutron-skin thickness, which is determined by the symmetry energy of the equation of state (EOS). Furthermore, it was found that the PDR contribution to the cross-section of radiative neutron capture process is significant. Therefore, studies on PDR nature are attracting a lot of attention in recent years.

So far the experimental evidence of PDR was based on scattering of real photons (γ,γ'), inelastic scattering of electrons, protons and alpha particles, and on relativistic Coulomb excitations. In the present thesis, for the first time the inelastic scattering of heavy ions, combined with high-resolution gamma spectroscopy, was conducted.

General aim of the study, which is a subject of this thesis, was to investigate the properties of the dipole states in ^{140}Ce nucleus around particle threshold where the pygmy dipole states are expected to appear. Of particular interest was the possible isospin mixing observed in previous (γ,γ') and (α,α'γ) experiments. The more specific goal was to confront the experimental data with theoretical calculations using Distorted Wave Born Approximation (DWBA) based on a form factor obtained by folding the microscopically calculated transition densities which was done for the first time in this type of experiments.

The experiment using the inelastic scattering of ^{17}O at 20 MeV/u was performed in LNL-Legnaro in Italy. The scattered ions were detected by the two ΔE-E silicon telescopes of TRACE array in coincidence with the γ-rays emitted by the target nucleus. The gamma detection was done with a high energy resolution using the state-of-art AGATA array which is based on high-purity germanium (HPGe) detectors. To increase the detection efficiency in high energy region, nine large volume $LaBr_3$:Ce scintillator detectors of HECTOR+ array were additionally applied.

The results of the study allowed to confirm predominantly isoscalar character of the low-energy PDR states. For the first time, the fraction of isoscalar energy-weighted sum rule exhausted by the PDR and its strength was extracted for the ^{140}Ce. Comparison with the predictions of the theoretical models allowed shedding some new light into the structure of the pygmy dipole states. Furthermore, obtained results will enrich still very limited database of experimental results, what is necessary to gain complete knowledge of the PDR properties.

STRESZCZENIE

Widmo wzbudzeń jądra atomowego przy wysokich energiach jest zdominowane przez Gigantyczny Rezonans Dipolowy (GDR), który polega na kolektywnych drganiach prawie wszystkich neutronów względem protonów. W okolicy energii separacji neutronu, poniżej GDR, dla wielu jąder zaobserwowano wzrost funkcji nasilenia, który powiązany został z tzw. Pigmejskim Rezonansem Dipolowym (PDR). W najprostszym modelu, zjawisko to jest interpretowane jako oscylacje nadmiaru neutronów formujących tzw. skórkę neutronową względem rdzenia jądra składającego się z równej liczy protonów i neutronów. Liczne obliczenia mikroskopowe wykazały zależność pomiędzy nasileniem PDR, a grubością skórki neutronowej, która jest związana z energią symetrii w równaniu stanu materii jądrowej. Dodatkowo okazało się, że PDR ma istotny udział w przekrojach czynnych na radiacyjny wychwyt neutronów.

Dotychczasowe wyniki eksperymentalne potwierdzające istnienie PDR opierały się na rozpraszaniu rzeczywistych fotonów (γ,γ'), nieelastycznym rozpraszaniu elektronów, protonów oraz cząstek alfa, jak również relatywistycznych wzbudzeniach kulombowskich. W niniejszej pracy po raz pierwszy zastosowano nieelastyczne rozpraszanie ciężkich jonów w połączeniu z pomiarem spektroskopowym emitowanego promieniowania gamma przy wysokiej rozdzielczości.

Celem badań, będących przedmiotem niniejszej pracy, było określenie właściwości stanów PDR w jądrze ^{140}Ce. Szczególny nacisk położono na postulowane zmieszanie izospinu stanów pigmejskich, które było obserwowane w eksperymentach (γ,γ') oraz (α,α'γ). W tym celu porównano wyniki eksperymentalnie z obliczeniami metodą przybliżenia Borna fal zaburzonych (DWBA) z wykorzystaniem czynnika kształtującego obliczonego na podstawie gęstości przejść dla stanów pigmejskich. Takie podejście zastosowane zostało po raz pierwszy w tego typu eksperymentach.

Eksperyment z wykorzystaniem metody rozpraszania nieelastycznego jąder ^{17}O przy energii 20 MeV/u został przeprowadzony w LNL-Legnaro we Włoszech. Rozpraszane jądra były rejestrowane przy użyciu dwóch krzemowych detektorów typu ΔE-E z układu TRACE w koincydencji z pomiarem promieniowania gamma emitowanego przez wzbudzone jądra tarczy. Detekcja kwantów gamma prowadzona była z zastosowaniem zaawansowanego układu AGATA, składającego się detektorów germanowych (HPGe). Aby zwiększyć wydajność detekcji w zakresie wyższych energii, zastosowano dodatkowo dziewięć detektorów scyntylacyjnych, $LaBr_3$:Ce z układu HECTOR+.

Wyniki badań pozwoliły potwierdzić dominujący charakter izoskalarny stanów PDR, szczególnie ich składowej w obszarze niskich energii. Po raz pierwszy wyznaczono wartość izoskalarnej reguły sum ważonej energią odpowiadającą udziałowi stanów PDR i ich nasilenie dla jądra ^{140}Ce. Porównanie wyników z obliczeniami modelowymi stanowi istotny wkład w poznanie natury stanów PDR. Dodatkowo, uzyskane wyniki wzbogacają nadal ograniczoną bazę danych, której poszerzenie jest niezbędne dla pełnego poznania właściwości badanych stanów.

INTRODUCTION

From the discovery of the atomic nucleus by E. Rutherford in 1911, one of the main challenges was to see how it looks like and how it behaves in certain conditions. One of the most natural approaches is to shine a beam of photons on a nucleus and evaluate which frequency it absorbs. Another natural way is to heat up a nucleus and measure the frequency of photons that it emits. Such experiments have revealed a resonant behaviour of atomic nucleus, which is displayed as an absorption or emission of essentially monochromatic photons. The general feature of many-body quantum systems is to form collective modes. As one should expect, such behaviour is also exhibited by atomic nucleus, which is composed of protons and neutrons that can oscillate against each other in a resonant manner. When almost all nucleons participate in the process, it is described as so-called the Giant Resonances. The most studied example of such phenomenon is the Giant Dipole Resonance (GDR), which is a collective out-of-phase vibration of almost all neutrons *versus* protons. If one considers the dipole excitation spectrum of atomic nucleus, it is almost fully dominated at high energies by the GDR. However, around neutron binding energy, below the GDR, the presence of additional strength has been reported in many nuclei and associated to so-called the Pygmy Dipole Resonance (PDR). In the simplest picture, it was interpreted as an oscillation of the excess neutrons forming the neutron-skin *versus* core of the nucleus with equal number of protons and neutrons. Even though being much weaker than the GDR, the PDR was found to have a significant impact on many fundamental processes and quantities; just to mention the radiative neutron capture rates or neutron-skin thickness. Therefore, studies on electric dipole (E1) response, especially its low-lying component, are attracting a lot of attention in recent years.

So far the experimental evidence of the PDR was based on scattering of real photons, inelastic scattering of electrons, protons and alpha-particles, and on relativistic Coulomb excitation. The probes that interact with the nucleus exclusively by electromagnetic force were successfully applied to derive the total strength of the resonance for a broad range of nuclei. But the milestone to understand the underlying structure of the pygmy states was made when excitation *via* nuclear force was considered complementary. The comparison between (γ,γ') and $(\alpha,\alpha'\gamma)$ experiments, for a few stable nuclei, has demonstrated a complicated nature of the PDR, very much dependant on applied probe. It is predicted by theoretical models that the low-lying E1 component is actually a mixture of "real" pygmy states and the tail of the GDR. This was a strong motivation to make another step forward, and apply heavy ions as additional complementary probe, which is, however, very challenging.

In the present thesis, for the first time the inelastic scattering of heavy ions combined with high-resolution gamma spectroscopy was conducted. The experiment was performed in Legnaro National Laboratories (LNL) in Italy. The ^{17}O nuclei at the energy of 20 MeV/u were chosen to ensure sensitivity of probing the nuclear surface *via* mostly the nuclear interaction. This nucleus has also a low neutron binding energy (4.1 MeV), therefore for the excitation energies higher than 4 MeV, which is exactly the PDR region, the neutron evaporates and the projectile lives the reaction channel. As a result, the spectrum in PDR energy region is clean from projectile

excitation. A very precise identification of the inelastic scattering channel and measurement of the excitation energy was performed using two ΔE-E silicon telescopes, which were prototypes of the TRACE project. Additionally, the detectors were made of pixels, which allows for position sensitivity. As the PDR is expected to be composed of a number of 1^- states, one needs to be sensitive in such measurement to the spin of the excited states. A good solution is to measure the scattered heavy ions in coincidence with the de-excitation γ-rays. Furthermore, if one wants to examine the discrete structure of the resonance, it is necessary to use the detectors with very good energy resolution. It is difficult to imagine a better instrument than the AGATA array that was used in this measurement. It was the last experiment of very successful AGATA campaign in Legnaro, and the measurement fully profited from five triple clusters of segmented germanium detectors available at that time. Just to mention the innovative algorithms of pulse shape analysis and tracking, which allows to determine the point of interaction with remarkable precision and then to reconstruct the path of the γ ray within each crystal. As the PDR strength is relatively small, the nine large volume $LaBr_3$ detectors were additionally applied in order to increase the statistics in high-energy region. The scintillators are known to have worse energy resolution than germanium crystals, however, they are very efficient to detect high-energy γ rays.

The measurement was performed for several nuclei (^{208}Pb, ^{140}Ce, ^{124}Sn) from different mass regions and with different internal structure. What is important, for each nucleus, the data from different experiments: (γ,γ'), (p,p') or (α,α'γ) were available for direct comparison. The present thesis concentrates on the results for the ^{140}Ce, which is a spherical nucleus with a magic number of neutrons (N = 82). General aim of the study was to investigate the properties of the dipole states below particle threshold where the pygmy dipole states are expected to appear. The more specific goal was to confront the experimental data with theoretical calculations using Distorted Wave Born Approximation (DWBA), which is well-established method to describe the heavy ion inelastic scattering. For the first time, the microscopically calculated form factor was included in the analysis allowing to estimate the fraction of the PDR strength.

It is expected that the results of this study will open a new experimental perspective that can be further extended in gamma spectroscopy studies using new instrumentation, which is for example the PARIS gamma calorimeter. Experimental methods developed in the course of the project can be applied at facilities that are already operational, as LNL Legnaro (Italy), GANIL (France), RIKEN (Japan), HIL-Warsaw (Poland), Cyclotron Centre Bronowice at IFJ PAN in Krakow or are under construction: SPIRAL2 (France), HIE-ISOLDE at CERN, SPES (Italy).

In brief, Chapter 1 of the thesis gives necessary introduction to electric dipole response of nuclei and in particular the pygmy dipole resonance focusing on a brief overview of studies, both experimental and theoretical, that have been conducted on the PDR in ^{140}Ce. Then, the mechanism of inelastic scattering of heavy ions including the distorted wave Born approximation (DWBA) will be introduced in Chapter 2. Description of experimental technique and setup designed for the study is given in Chapter 3. Chapter 4 includes the details of complex data analysis process. The most important results of the study and their discussion are presented in Chapter 5. Last Chapter presents the final conclusions and outlook.

Chapter 1. ELECTRIC DIPOLE (E1) RESPONSE OF NUCLEI

One of the most fundamental problems of the nuclear physics is to determine the structure of the atomic nucleus and bulk properties of nuclear matter of dense astrophysical objects like neutron stars. The goal is to determine the parameters of the nuclear equation of state (EOS). Since an atomic nucleus is composed of two kinds of nucleons: protons and neutrons, the EOS contains a term – the symmetry energy - which is related to the asymmetry between proton and neutron densities. Accurate determination of the symmetry energy is now attracting a lot of attention from both experimental and theoretical points of view, as it allows predicting the properties of exotic nuclei with large differences in neutrons and protons numbers. In astrophysics, the symmetry energy is related to the properties of the neutron stars, such as the radius, mass or internal structure. The link was found between symmetry energy and so-called the dipole polarizability, which is related to the electric dipole (E1) response of nuclei. This is one, among other reasons why precise determination of E1 response is now attracting a lot of attention of experimental nuclear physicists. The other important reasons will also be presented later in the thesis.

The explanation what exactly is the E1 transition may come within the shell model that is successfully applied to illustrate the structure of a nucleus. In such approach, each state of the nucleus has definite values of energy, angular momentum (J) and parity (π). Atomic nucleus in an excited state can release its energy by emission of electromagnetic radiation in a process of γ-ray decay. Each photon can carry an exact integer number of angular momentum units ($\hbar$). The multipolarity of the emitted photon is a quantification of the amount of angular momentum between final (f) and initial (i) state, $l = |J_f - J_i|$ carried by the photon. For example, photon with $l = 0$, is called monopole, $l = 1$ dipole, $l = 2$ quadrupole, $l = 3$ octupole photon and so on. The transition may also change the parity of the state thus have the electric (E) of magnetic (M) type. The parity changes in the following way: $\pi_i\pi_f = (-1)^l$ for electric, and $\pi_i\pi_f = (-1)^{l+1}$ for magnetic transition. Thus, the electric dipole (E1) transition changes the parity and angular momentum of 1 unit. The γ transition can be described using so-called the reduced transition probability which is related to the nuclear matrix elements and does not depend on energy of the transition. This will be discussed in more details in sec. 1.1.1.

One of the ways to express the E1 response it is to use the strength functions, which will be briefly explained in sec. 1.1.3. Such typical E1 strength spectrum for the nuclei near closed shells in mass region around A = 140 is schematically shown in Fig. 1.1. The major part of the E1 strength is dominated by the Isovector Giant Dipole Resonance (IVGDR), which is very well studied collective phenomenon described as out-of-phase oscillations of nearly all protons versus neutrons, and located in the energy range well above neutron separation energy (10-20 MeV). Below IVGDR and around neutron separation energy (S_n), a fraction of discrete dipole states is

also observed and associated to the so-called Pygmy Dipole Resonance (PDR). It was found that this additional low-lying strength around neutron emission energy threshold is not only an interesting nuclear structure phenomenon that cannot be described with any simple model. It has also a very strong influence on properties of nuclei e.g. neutron skin thickness which is related to the symmetry energy or fundamental processes e.g. neutron capture rates. The lack of knowledge about the origin and properties of the PDR states has attracted a lot of attention to this phenomenon in recent years. The lowest E1 excitation, which is marked in pink, is related to the one-particle structure and identified as a two-phonon state, which originates from coupling of the quadrupole and octupole states ($2^+ \otimes 3^-$). These three excitation modes will be further described later in this chapter.

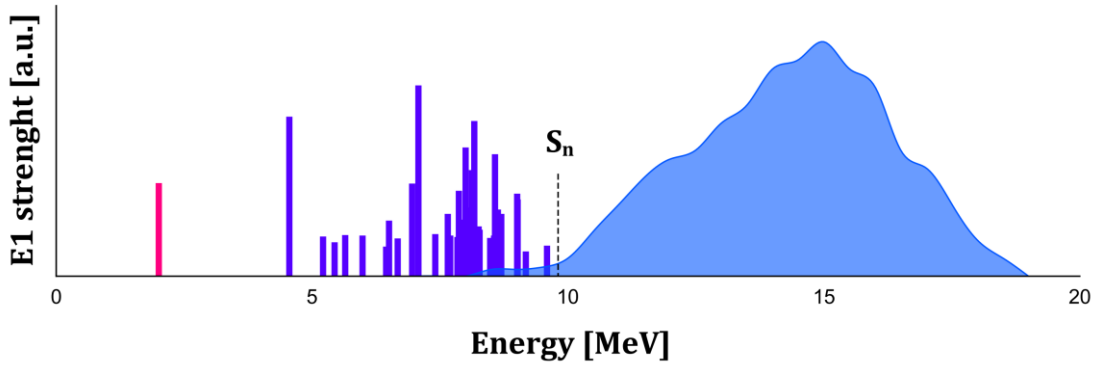

Figure 1.1: *Schematic illustration of the electric dipole (E1) response of nucleus. Energy of neutron emission is marked (S_n).*

Another useful approach to describe the electromagnetic response of nuclei is to use the so-called Energy-Weighted Sum Rules (EWSR) that are defined at the base of a strength functions and can illustrate well how energy absorbed in the reaction e.g. inelastic scattering is distributed to the nucleons in a given excitation mode. The GDR usually exhaust nearly 100% of EWSR while PDR does not exceed a few percent. This may give a quantitative description of the excitation mode collectivity. The concept of sum rules will be explained in more details in sec. 1.1.3.

One of very important aspects of studying the electromagnetic response is whether the excitation is related to the change of isospin vector. If the isospin changes, the excitation is considered as isovector, while no change is associated with isoscalar type. Very important insight into isospin nature of an excitation can be given by studying the so-called transition densities, which are very useful to illustrate the neutron and proton relative contribution to the excitation. This concept will be briefly introduced in sec. 1.1.2. The isospin properties of giant resonances are rather well established. Meanwhile, the question whether the PDR states are predominantly isoscalar or isovector is not yet fully answered. The present thesis attempts to shed light on this subject.

1.1. GENERAL FEATURES

The aim of this section is to introduce some basic concepts focusing on a description of the E1 response that will help to understand the features of different modes of excitations that will be considered in the thesis. Therefore, the definitions of reduced transition probability, transition density as well as strength functions and sum rules will be now briefly introduced based mostly on Refs. [Bor98, Har01].

1.1.1. Reduced Transition Probability

The reduced transition probability for the γ-decay between an excited state (i) and a lower energy state (f) is defined as:

$$B(\sigma\lambda, J_i \rightarrow J_f) = \sum_{\mu, M_f} \left|\langle \mathrm{J}_f \mathrm{M}_f | M(\sigma\lambda,\mu) | \mathrm{J}_i \mathrm{M}_i \rangle\right|^2 \tag{1.1}$$

where σ denotes electric (E) or magnetic (M) transitions, $M(\sigma\lambda\mu)$ is the electromagnetic transition operator of parity π (for electric transitions, $\pi_i\pi_f = (-)^{\lambda}$, for magnetic transitions $\pi_i\pi_f = (-)^{\lambda+1}$), multipolarity λ and magnetic component $\mu = M_i - M_f$.

According to the Wigner-Eckart theorem a matrix element of an operator $M(\sigma\lambda\mu)$ can be factorized:

$$\langle \mathrm{J}_f \mathrm{M}_f | M(\sigma\lambda,\mu) | \mathrm{J}_i \mathrm{M}_i \rangle = (J_i \lambda M_i \mu | J_f M_f) \langle J_f || M(\sigma\lambda,\mu) || J_i \rangle \tag{1.2}$$

where $(J_i \lambda M_i \mu | J_f M_f)$ is a Clebsh-Gordan coeffient.

Using the orthonormality of the Glebsch-Gordan coefficient, the Eq. 1.1 can be written as follows:

$$B(\sigma\lambda, J_i \rightarrow J_f) = \frac{1}{2J_i + 1} \left|\langle J_f || M(\sigma\lambda,\mu) || J_i \rangle\right|^2 \tag{1.3}$$

The reduced matrix elements $\langle J_f || M(\sigma\lambda,\mu) || J_i \rangle$ contain information about the nuclear wave functions. The reduced transition rates of an electromagnetic excitation (↑) are related to that of the γ-decay (↓) by:

$$B(\sigma\lambda) \uparrow = \frac{2J_i + 1}{2J_f + 1} B(\sigma\lambda) \downarrow \tag{1.4}$$

Reduced transition rates for the electric transitions are usually expressed in units of $e^2fm^{2\lambda}$ or Weisskopf units (W.u.). The latter is defined as [Bru77]:

$$B(E\lambda; I_i \rightarrow I_{g.s.})[W.u.] = \frac{1}{4\pi}(1.2)^{2\lambda}\left(\frac{3}{\lambda+3}\right)^2 A^{\frac{2\lambda}{3}} \left[e^2 fm^{2\lambda}\right] \tag{1.5}$$

One can see that W.u. depends not only on the multipolarity λ of the transition but also on the mass A of the nucleus.

1.1.2. Transition Density

Giant resonances are described as vibrational states, which means that an oscillation of the nucleon density around the ground state density $\rho^0(\vec{r})$ is expected. If one considers an excited vibrational state $|\nu\rangle$, the corresponding time-dependent wavefunction can be written as:

$$|\psi(t)\rangle = |0\rangle + c_\nu|\nu\rangle e^{-\frac{iE_\nu t}{\hbar}} \tag{1.6}$$

and the corresponding nucleon density is given by:

$$\rho(\vec{r},t) = \langle\psi(t)|\sum_{i=1}^{A}\delta(\vec{r}-\vec{r_i})\,|\psi(t)\rangle = \rho^0(\vec{r}) + \delta\rho(\vec{r},t) \tag{1.7}$$

with:

$$\delta\rho(\vec{r},t) = \langle 0|\sum_{i=1}^{A}\delta(\vec{r}-\vec{r_i})\,|\nu\rangle e^{-\frac{iE_\nu t}{\hbar}} + c.c \tag{1.8}$$

The transition density is the time-independent part of $\delta\rho(\vec{r},t)$, that is:

$$\rho^\nu(\vec{r}) = \langle 0|\sum_{i=1}^{A}\delta(\vec{r}-\vec{r_i})\,|\nu\rangle \tag{1.9}$$

where $\delta(\vec{r}-\vec{r_i})$ is the Dirac delta function.

Transition densities can be used to have an insight in the structure of a vibrational state, in particular regarding the spatial distribution of the oscillations, and can be calculated theoretically. Transition densities reflect the contribution of protons and neutrons to a given excitation. They illustrate well the idea of isoscalar and isovector excitations. As the isovector excitations are associated to the change of isospin (ΔT = 1), the relative motion of the neutrons vs. protons should be out-of-phase, which is reflected in the opposite sign of their transitions densities. On the contrary, the isoscalar states (ΔT = 0) are illustrated by the neutron and proton transition densities of the same sign. The examples of calculated transition densities characteristic for giant dipole resonance and pygmy dipole resonance will be introduced in sec. 1.3.2 and sec. 2.2.3.

It is difficult to experimentally probe the transition density directly. One can estimate that wavelengths of photons of energies up to ~20 MeV are larger than the typical values of nuclear radii. This means that a photon excitation involves the whole volume of the nucleus. In case of using hadronic probes, the collisions are mainly peripheral and the excitation is mainly superficial, because of the short range of the strong interaction, and states with transition densities peaked on the surface are favoured.

1.1.3. Strength Functions and Sum Rules

From a conceptual point of view the sum rule method provides a natural link between the quantum description of the collective phenomenon given by microscopic calculations and its macroscopic structure contained in classical models, emphasizing the crucial role played by bulk and/or surface parameters of the nuclear medium (incompressibility, symmetry energy, etc.). Example of the review on sum rule, among many others, can be found here [Lip89]. The following section will give only a brief summary.

In order to describe the sum rule, one may start from defining the *strength function* that characterize the response of the nuclear ground state $|0\rangle$ to the operator $\hat{F}$. As a result the nucleus reaches the excited state $|n\rangle$. Strength function is expressed as follows:

$$S_F(E) = \sum_{n\neq 0} \left|\langle 0|\hat{F}|n\rangle\right|^2 \delta(E - E_{n0}) \tag{1.10}$$

where n labels the complete set of eigenstates of the Hamiltonian $\hat{H}$, E_{n0} are the energies of such states relative to the ground state ($E_{n0}=E_n-E_0$) and $\delta(E - E_{n0})$ is the Dirac delta function.

In general, the operator $\hat{F}$ depends on spatial coordinates, spin and isospin. Therefore, very different electromagnetic responses can be expressed with the strength functions. The examples of the calculated E1 strength functions will be given in sec. 1.3.2 indicating the differentiation between isoscalar and isovector excitations. Very important example of strength function application is the relation with the dipole photoabsorption cross-section $\sigma_{E1}(E)$, which can be expressed as [Lit09b]:

$$\sigma_{E1}(E) = \frac{16\pi^{3e^2}}{9\hbar c} E S_F(E) \tag{1.11}$$

The example of photoabsorption cross-section with characteristic shape of giant resonance will be presented in sec. 1.2.

The *sum rules* can be derived starting from the strength function. One can define the moment of the strength function as:

$$M_k = \int_0^\infty S_F(E)\, E^k dE = \left\langle 0\middle|\hat{F}^\dagger\left(\hat{H}^k - E_0\right)\hat{F}\middle|0\right\rangle \tag{1.12}$$

where k is the order of the moment.

In principle, the infinite set of moments ($-\infty < k < \infty$) determines the exact strength function. In the case of resonance phenomena, however, only few moments are needed to obtain an adequate description of strength function.

Of particular importance is the first moment, so called the *Energy-Weighted Sum Rule (EWSR)* of the operator $\hat{F}$:

$$M_1 = \sum_n \left|\langle 0|\hat{F}|n\rangle\right|^2 (E_n - E_0) \tag{1.13}$$

In the case of atomic nuclei, general assumption can be made that $\hat{F} = \sum_k F(\overrightarrow{r_k})$ is a one-particle operator depending only on the spatial coordinates (that is true for electric transitions, $\hat{F} = \hat{M}(E\lambda\mu)$). If the Hamiltonian is velocity-independent (which is true for most effective interactions), one obtains that:

$$\sum_n \left|\langle 0|\hat{F}|n\rangle\right|^2 (E_n - E_0) = \frac{\hbar^2}{2m}\int \left|\vec{\nabla}\hat{F}\right|^2 \varrho(\vec{r})\, d\vec{r} \tag{1.14}$$

where $\varrho(\vec{r})$ is the nucleon density in the ground state of the nucleus.

This result can be understood intuitively when considering that an impulsive field $\hat{F}$ transfers a momentum $\vec{\nabla}\hat{F}$ to the particles which were on average at rest, meaning that they gain an average energy of $\hbar^2\left|\vec{\nabla}\hat{F}\right|^2/2m$. This is consistent with the fact that the EWSR does not depend on the interaction among the nucleons, because the energy is absorbed before the system is disturbed from equilibrium.

Simple physical meaning of the EWSR expressed by Eq. 1.13 is that the left side is related to the total energy absorbed by the nucleus, while the right side is related to the energy transferred to the nucleons. Thus, it is interesting to calculate the percentage of a sum rule that is related to a given excitation mode. Fraction of EWSR for a given excitation energy E_x, can be expressed as follows:

$$EWSR[\%] = \frac{E_x S_F}{M_1} \cdot 100\% \tag{1.15}$$

For example, the GDR usually exhaust around 100% of EWSR, which means that almost all nucleons are involved in the excitation. On the other hand, PDR usually exhaust up to a few percent of EWSR. The sum rules can be calculated for different types of excitations [Har01]. The sum rule for *isovector dipole* excitations (IVEWSR) can be expressed as follows:

$$\sum_n (E_n - E_0)B(E1, 0 \to n) = 14.8\frac{NZ}{A}\ [e^2 fm^2 \cdot \mathrm{MeV}] \tag{1.16}$$

The sum rule for *isoscalar dipole* excitations (ISEWSR) can be expressed as follows:

$$\sum_n (E_n - E_0)B([IS]E1, 0 \to n) = 0.008A(33\langle r^4\rangle - 25\langle r^2\rangle^2) \quad [\, e^2 fm^6 \cdot \mathrm{MeV}] \tag{1.17}$$

with: $\langle r^\lambda\rangle = \frac{3}{3+\lambda}R^\lambda$ and $R = 1.2A^{1/3}$

1.2. GIANT RESONANCES

The main subject of this thesis is the study of the electric dipole response, however, the brief general overview on all giant resonances will be here presented, following Refs. [Bor98, Har01].

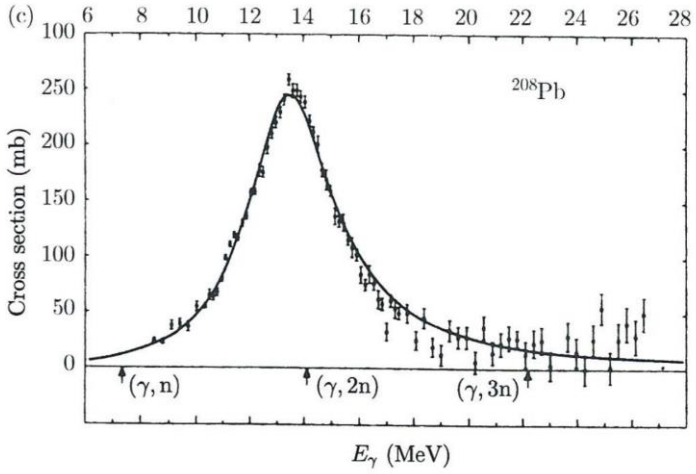

Figure 1.2: *Photo-absorption cross-section spectrum as a function of photon energy for ^{208}Pb nucleus. Taken from Ref. [Har01].*

The common feature of many-body quantum systems is to form collective modes. Giant resonances are basic modes of nuclei excitation, which correspond to a collective vibrational motion of almost all nucleons. Its study has provided very useful information on the nuclear structure but also on the effective nucleon-nucleon interaction as well as on the bulk properties of nuclear matter such as the compression modulus, the viscosity or the symmetry energy. In macroscopic picture, giant resonances can be considered as a high-frequency, damped, nearly harmonic vibrations of the density or shape of the nuclear system around an equilibrium value. Its vibration amplitude is of the order of a few percent of the nuclear radius. Giant resonance, as any other resonance, can be parametrized by tree values: the energy E_R, the width Γ_R, and the strength S_R. An example of GR can be observed in Fig. 1.2, where photo-absorption cross-section spectrum as a function of photon energy is plotted. The data are fitted with a Lorentzian function [Har01]:

$$\sigma(E) = \frac{\sigma_m \Gamma_R^2 E^2}{(E^2 - E_R^2)^2 + \Gamma_R^2 E^2} \tag{1.18}$$

where $\sigma(E)$ is the excitation cross-section, E_R is the resonance centroid energy and Γ_R is the resonance width. The cross section value at the maximum (σ_m) is related to the strength via a normalization factor.

The centroid energy of GR usually lies above the neutron separation energy at around 10-15 MeV depending on mass of nucleus, with a corresponding vibration frequency of the order of 10^{21} Hz.

The width of a resonance is of the order of 2-5 MeV. This means that after a few vibrations the resonance is completely damped. The strength of giant resonance is limited to the maximum allowed by appropriate sum rule (for details on sum rules see sec. 1.1.3) and is close to its 100%. This is a common feature for many quantum systems that the sum of all transition strengths for a given set of quantum numbers is determined by basic properties of the system. For the nuclear system, these would be for example the number of nucleons A and the atomic number Z. In case of giant resonances, which are collective motion of all nucleons, it is expected that its gross features do not depend on the detailed structure of the nucleus, but rather on its bulk structure. Indeed, studies of giant resonances have shown that the parameters of a given resonance vary smoothly with the number of nucleons A. However, it was also shown that the width of the resonance is also dependent on the microscopic structure of the nucleus, due to direct particle emission and to the coupling to more complex configurations.

1.2.1. Classification

Isovector Giant Dipole Resonance is the most studied one, however, it is known that there are many other types of giant resonances, which can be classified according to the multipolarity L, the spin S and the isospin T quantum numbers:

- *Electric (ΔS=0) isoscalar (ΔT=0)* vibrations where protons and neutrons oscillate in phase according to a multipole pattern defined by λ=0, 2,… To first order (λ=1) vibration corresponds to a translational motion of the nuclear centre of mass (CM) and is not an intrinsic excitation; however, there is a higher-order λ=1 vibration.
- *Electric (ΔS=0) isovector (ΔT=1)* vibrations where protons oscillate against neutrons. For the same multipolarity, isovector modes have a higher excitation energy due to the extra energy required to separate the protons from the neutrons.
- *Magnetic or spin-flip (ΔS=1) isoscalar (ΔT=0)* modes where nucleons with spin up oscillate against nucleons with spin down
- *Magnetic (ΔS=1) isovector (ΔT=1)* modes where protons with spin up oscillate against neutrons with spin down and vice versa.

Various types of resonance for multipolarity λ=0,1,2 is shown schematically in Fig. 1.3.

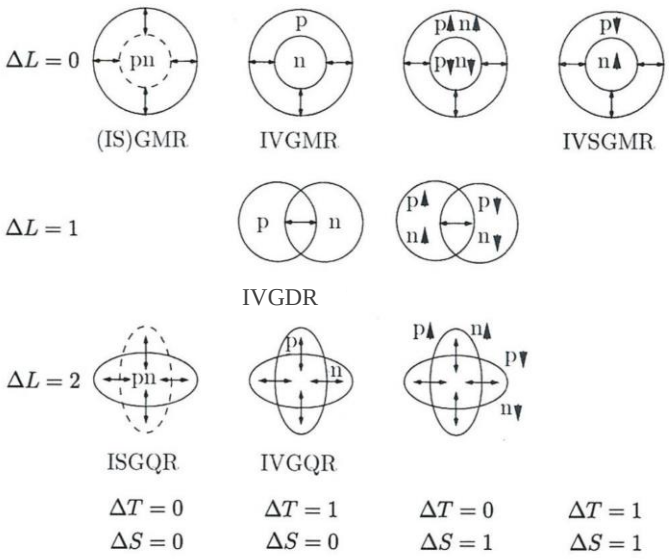

Figure 1.3: *Classification of giant resonances according to the multipolarity, spin and isospin quantum numbers, taken from Ref. [Har01].*

1.2.2. Microscopic Description

At the microscopic level, giant resonances can be treated as a coherent superposition of particle-hole excitations coupled to the same angular momentum, spin and isospin of the resonance. If one considers the operation on the ground state of the nucleus of one-body operator, the resulting giant resonance state can be written as:

$$|\psi_{GR}^{\lambda,\sigma,\tau}\rangle = O^{\lambda,\sigma,\tau}|\Psi_{g.s.}\rangle \tag{1.19}$$

where λ is the multipolarity of the resonance, σ its spin and τ its isospin.

As an example, the electric isoscalar transition operator is defined as:

$$O^{\lambda,0,0} = \sum_{i=1}^{A} r^{\lambda} Y_{\lambda,\mu}(\Omega_i), \lambda \geq 2 \tag{1.20}$$

where the sum is performed over all the nucleons and the functions $Y_{\lambda,\mu}(\Omega_i)$ are the spherical harmonics in the coordinates of the nucleon i.

In the schematic shell-model picture for the single-particle motion (see Fig. 1.4), the single-particle wave functions in following shells: N, N+1, N+2… have alternating parity and energy difference $\Delta E = \Delta N * 1\hbar\omega$. The operator $O^{\lambda,0,0}$ can only induce transitions with $\Delta N \leq \lambda$. Then, parity considerations imply that dipole ($\lambda = 1$) vibrations are composed by $\Delta N = 1$ excitations, while giant resonances with a quadrupole character ($\lambda = 2$), are composed by $\Delta N = 2$ excitations. The $\Delta N = 0$ excitations correspond to low-lying collective vibrations.

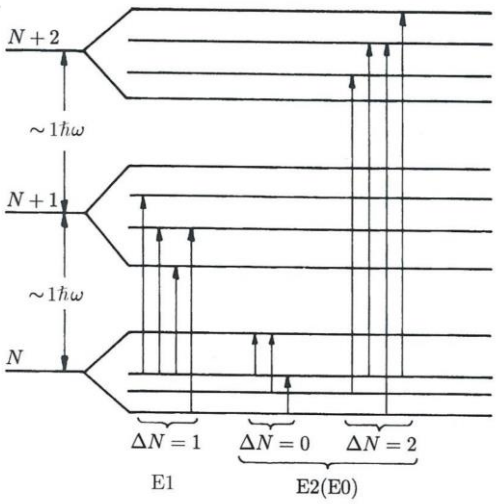

Figure 1.4: *Schematic representation of E1 and E2 particle-hole states in a shell model. Taken from Ref. [Har01].*

More accurately, giant resonances can be described using mean field models and effective nucleon-nucleon interactions. In such approach, one may describe the ground state of the nucleus by generating a self-consistent mean field from the effective two-body interaction using the Hartree-Fock method. Then, the ground state is a Slater determinant of single-particle orbitals where all the states below the Fermi surface are fully occupied and all the state above are unoccupied. It is therefore possible to induce a small-amplitude density fluctuation around the equilibrium configuration using an external field. The fluctuations can be described with the time-dependent Hartree-Fock equation In the small-amplitude limit, it is possible to derive the Random-Phase Approximation (RPA) equations, which allow to diagonalize the residual interaction in the complete space of 1p-1h (1 particle - 1 hole) configurations. Second order RPA calculations include 2p-2h to account for the coupling of the resonance to more complex configurations. RPA can be extended in order to take into account the coupling to the continuum states (CRPA) or the effects of pairing correlations (QRPA, quasiparticle RPA).

In order to describe the properties of the nuclei near the β-stability, mean field approaches have been successfully applied. However, with the improvement in experimental techniques it became possible to study the nuclei far from stability. In such cases, the Relativistic Mean Field (RMF) models have been demonstrated to better reproduce the experimental data, especially the spin-orbit term, which is derived from the Lagrangian in RMF. Furthermore, it is possible to study collective vibrations in a relativistic framework by building a self-consistent Relativistic RPA (RRPA) on top of a RMF description of the ground state. This can be further extended to include the coupling to continuum states (CRRPA), which is very important with weakly bound exotic nuclei, and to include the pairing effect (QRRPA).

1.2.3. Decay Mechanism of Giant Resonances

As mentioned before, giant resonances can be treated as a well-ordered, collective motion of all the nucleons, which is a coherent sum of many 1p-1h excitations. The decay of a giant resonance is explained by more coexisting mechanisms, each causing a part of the total width of the resonance. Therefore, the total width (Γ) composes of different contributions:

- $\Gamma^{\downarrow}$: *damping width*, caused by the coupling of the 1p-1h state of the giant resonance to more complex configurations. It is the dominant contribution to the total width
- $\Gamma^{\uparrow}$: *escape width*, which accounts for the direct emission of particles, since the 1p-1h state lies above the particle emission threshold; typically $\Gamma^{\uparrow}/\Gamma \sim 10^{-1}$
- Γ^{γ}: *photon emission width*, which is much smaller contribution than the escape width because particle emission is favoured. $\Gamma^{\gamma}/\Gamma \sim 10^{-4}$

This damping mechanism is a basic example of the process in which well-ordered collective excitation dissolves into a disordered motion of internal degrees of freedom in fermionic quantum many-body systems. For the high excitation energies of the resonance, there is a high density of 2p-2h configurations with the same spin and parity as the resonance. The 1p-1h states can mix with 2p-2h states, which in turn mix to 3p-3h, states, in a process that goes up in a hierarchy of complexity that ends in a state in which the excitation energy has been spread over all degrees of freedom and a compound nucleus is eventually formed.

As it will be shown later in the thesis (sec. 5.1), the applied technique of ^{17}O inelastic scattering allows to excite the GRs. It was expected that the experimental setup designed for this study would allow to observe the γ decay of the GRs. Such data is desired especially for the ISGQR, which is not much studied yet. This is however very challenging, as the photon emission channel is less probable than the particle emission ($\Gamma^{\gamma}/\Gamma^{\uparrow} \sim 10^{-3}$).

1.3. PYGMY DIPOLE RESONANCE

First experimental studies on the low-lying dipole states dates back to the late 1950's and 1960's when the Bartholomew et al. showed an enhancement of the γ-rays strength around 5-7 MeV by studying systematically the thermal neutron capture followed by γ-rays emission [Bar61]. The term "pygmy resonances" was first used probably by Brzosko et al. who studied the possible influence of this new mode of excitation on neutron capture cross sections [Brz69]. Over the years, the low-lying dipole states were intensively studied using various techniques, including scattering of real photons, inelastic scattering of electrons, protons and alpha particles, and on relativistic Coulomb excitations.

First theoretical interpretation of this new mode was based on the incompressible three fluids hydrodynamical model [Moh71]. This allowed to extract two independent electric dipole resonances: one originating from the oscillations of all neutrons *versus* all protons (GDR) and energetically lower-lying mode, where only neutrons excess oscillate against the isospin saturated core. Within this simple picture, the phenomenon is often denoted as Pygmy Dipole Resonance (PDR). Since then a lot of attention was given to the theoretical calculations, especially based on macroscopic models.

The low-lying dipole strength is not only an interesting nuclear structure phenomenon but it also has different implications and applications in different areas.

1.3.1. Experimental Studies

The dipole states lying around particle threshold energy have been intensively studied in recent years using various experimental techniques and for the broad range of nuclei. This section will briefly introduce a few examples of different experimental methods, following mostly an overview that has been recently given in Ref. [Sav13]. Particular interest will be given to results regarding the ^{140}Ce nucleus, which is a subject of this thesis.

Real photon induced experiments

The first group of studies is based on a real photon induced experiments. Among them, the (γ,γ') Nuclear Resonance Fluorescence (NRF) method has been widely used for a broad range of stable nuclei allowing to study the dipole states below neutron separation energy. It is however interesting to study the PDR states also above particle threshold, which is possible in photo-dissociation (γ,n).

Table 1.1: *Excitation energies of 1^- pygmy states for ^{140}Ce nucleus, reduced transition probability B(E1)↑ obtained in NRF experiments and differential cross sections obtained in (α,α'γ).*

E_x [keV]	Excitation	B(*E1*)↑ [10^{-3} e^2fm^2]		dσ/dΩ [mb/sr]
		S. Voltz et al. [Vol06]	R.-D. Herzberg et al. [Her97]	J. Endres et al. [End09]
3643.8	(γ,γ') and (α,α'γ)	21.7 (33)	18.2 (23)	0.176 (20)
4173.6	(γ,γ') and (α,α'γ)	5.1 (10)	3.2 (4)	0.140 (19)
4354.9	(γ,γ')	4.3 (9)	3.8(5)	-
4514.9	(γ,γ') and (α,α'γ)	5.3 (10)	3.7 (5)	0.109 (19)
4787.8	(γ,γ') and (α,α'γ)	5.2 (10)	4.3 (6)	0.084 (21)
5157.3	(γ,γ') and (α,α'γ)	3.7 (7)	3.5 (6)	0.116 (25)
5190.2	(γ,γ') and (α,α'γ)	4.6 (9)	4.6 (7)	0.165 (28)
5211.6	(γ,γ') and (α,α'γ)	2.7 (7)	3.7 (6)	0.067 (24)
5337.3	(γ,γ') and (α,α'γ)	4.8 (10)	4.2 (7)	0.347 (37)
5548.4	(γ,γ') and (α,α'γ)	7.9 (14)	7.5 (14)	0.203 (27)
5573.8	(γ,γ') and (α,α'γ)	4.5 (10)	3.9 (7)	0.141 (28)
5659.9	(γ,γ') and (α,α'γ)	26.0 (40)	23.5 (46)	0.341 (35)
5928.6	(γ,γ') and (α,α'γ)	5.4 (1.1)	5.1 (11)	0.127 (35)
6119.1	(γ,γ')	8.2 (14)	6.1 (-2.0, +1.5)	-
6130.6	(γ,γ')	3.8 (8)	3.1 (-1.1, +0.7)	-
6161.7	(γ,γ') and (α,α'γ)	5.2 (12)	4.3 (-1.6, +1.1)	0.354 (37)
6273.6	(γ,γ')	5.0 (9)	4.4 (-2.0, +1.2)	-
6295.3	(γ,γ')	11.4 (20)	10.5 (-4.9, +2.6)	-
6327.8	(γ,γ')	4.0 (15)	1.9 (-1.0, +0.5)	-
6343.3	(γ,γ')	6.6 (13)	7.3 (-3.9, +1.9)	-
6352.7	(γ,γ')	7.4 (14)	-	-
6397.2	(γ,γ')	17.4 (28)	19.1 (-11.2, +4.9)	-
6439.9	(γ,γ')	9.1 (16)	10.4 (-6.6, +2.8)	-
6449.9	(γ,γ')	5.4 (11)	-	-
6458.5	(γ,γ')	4.8 (10)	-	-
6484.8	(γ,γ')	4.7 (10)	7.8 (-5.5, +2.1)	-
6497	(γ,γ')	14.3 (24)	21.9 (-15.7, + 6.1)	-
6535.8	(γ,γ')	21.1 (33)	28.7 (-22.6, +8.2)	-
6549.1	(γ,γ')	3.7 (8)	5.9 (-4.7, +1.7)	-
6574.9	(γ,γ')	4.0 (8)	6.2 (-5.2, +1.9)	-
6605.5	(γ,γ')	6.5 (11)	10.4 (-9.1, +3.1)	-
6616.2	(γ,γ')	6.0 (11)	-	-
6781.9	(γ,γ')	4.9 (11)	-	-
6841.8	(γ,γ')	5.2 (14)	-	-
6862.4	(γ,γ')	16.5 (29)	-	-
6905.9	(γ,γ')	8.8 (19)	-	-
6932.6	(γ,γ')	7.5 (16)	-	-
6960.4	(γ,γ')	8.2 (17)	-	-
7206.0	(γ,γ')	11.0 (19)	-	-
7214.8	(γ,γ')	10.2 (17)	-	-
7341.5	(γ,γ')	3.7 (14)	-	-
7673.4	(γ,γ')	3.8 (9)	-	-

The gamma beam that is needed for such studies can be produced using different techniques: bremsstrahlung, tagged photons or laser Compton back-scattering (LCB). Important advantages of the *photon scattering* are the selectivity to dipole states excitations predominantly as well as known mechanism of such excitations including only the electromagnetic force. Therefore, intrinsic properties like spin, parity or transition strengths can be extracted from the measured quantities (angular distribution, cross section etc.) in a model independent way. In ^{140}Ce nucleus the excitation of 1^- states was studied in high-resolution photon scattering experiments at the bremsstrahlung facility of the electron accelerator S-DALINAC at TU Darmstadt [Her97, Vol06]. The Table 1.1 shows the energies of ground-state dipole excitations and their reduced transition probability, B($E1$; $1^- \rightarrow 0^+$) obtained in two NRF experiments. These values will be used later in the thesis when calculating the cross sections for the excitation of the PDR states using the DWBA method.

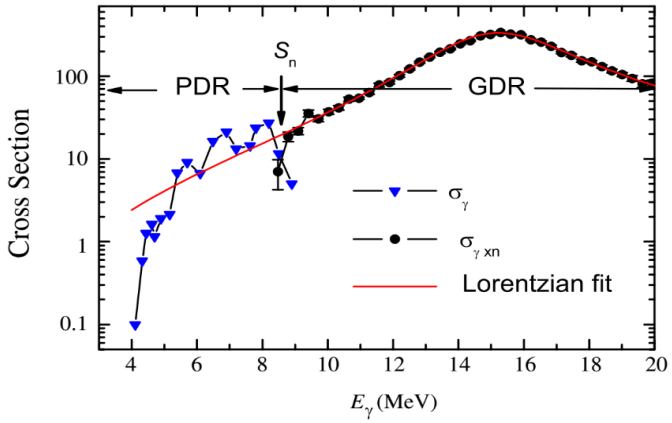

Figure 1.5: *Photo-absorption cross sections in ^{138}Ba below the neutron separation energy obtained in an NRF experiment with LCB photons combined with the GDR data. Taken from Ref. [Ton10].*

The NRF method is limited only to energy up to the neutron separation. It is however interesting to study the PDR states above particle threshold and this is possible using the *photo-dissociation* (γ,n) technique. For the energy region of pygmy excitations, the neutron energies in such reaction are very low and, thus, prompt detection is difficult. In addition, the daughter nucleus often has low-energy excited states and, therefore, measuring the neutron energy alone does not allow reconstructing the excitation energy. This requires extracting the energy information from the incoming photon beam. The beams from LCB facilities have been used in two kinds of experiments. First approach would count the neutrons in the (γ,n) reaction after moderation using a high-efficiency neutron counter [Uts03, Uts06]. Second approach bases on determination of the number of produced nuclei using off-line γ-ray spectroscopy of daughter nucleus [Son09]. Fig. 1.5 shows the total photo-absorption cross section for ^{138}Ba below neutron separation energy [Ton10] in combination with data above the threshold [Ber70] in a larger excitation energy region. An enhancement due to the PDR of the cross section at energies between 5 MeV and 8 MeV compared to a Lorentzian extrapolation of the GDR is observed.

Inelastic proton scattering

Most of the available methods are able to probe only part of the dipole strength. The technique that should potentially be suited to extract the full dipole strength for stable nuclei is the inelastic scattering of protons at forward angles. The method has been successfully applied to study the electric and magnetic dipole response of ^{208}Pb using high-intensity polarized proton beam at E_p = 295 MeV at RCNP-Osaka in Japan [Tam13]. In case of inelastic excitation using protons, at very forward angles the cross section for nuclear excitation is small and the measured yield is dominated by E1 transition due to Coulomb excitation and nuclear M1 spin-flip transition. It is possible to use multipole-decomposition methods taking into account for E1 Coulomb plus nuclear interaction (including interference), while for M1 and E2 pure nuclear interaction is assumed. In this way the authors extracted the cross section related to electromagnetic excitation. Since M1 transitions are suppressed in Coulomb excitation, and the E2 contribution to the cross section is small it was possible to derive the B(E1) distribution as shown in Fig. 1.6.

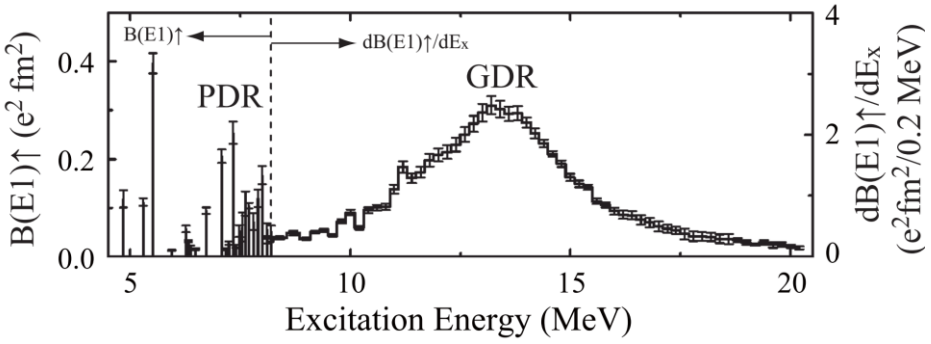

Figure 1.6: *Total B(E1) strength distribution of ^{208}Pb. The bump centred at ~13 MeV corresponds to the giant dipole resonance, and the strength concentration at around 7-9 MeV to the pygmy dipole resonance. Taken from Ref. [Tam13].*

Relativistic Coulomb excitation

One of the advantages of using heavy-ion induced electromagnetic excitation in the study of the dipole response of nuclei is its selectivity. Moreover, the method is applicable to inverse-kinematics measurements, which allow to investigate the short-lived nuclei by the use of relativistic radioactive beams. The large cross sections in the order of one barn for exciting the giant dipole resonance at beam energies above 500 MeV/nucleon make experiments possible even with rather low beam intensities. Another advantage is the straightforward relation of the measured Coulomb excitation cross-section to the photo-absorption cross-section and thus strength distributions. Higher-order corrections due to two-photon absorption can be easily taken into account. The complications due to contributions of different multipolarities and the nuclear contribution to the cross section become important only for precision measurements. In

such a case, a precise angular distribution and/or different beam energies have to be measured in order to allow the extraction of the B(E1) distribution.

First experimental evidence for a low-lying dipole resonance in neutron-rich unstable nuclei was provided from a measurement of the electromagnetic excitation of ^{130,132}Sn nuclei above the neutron threshold investigated with the FRS-LAND setup at GSI [Adr05, Kli07]. The results were deduced from Coulomb dissociation of secondary Sn beams with energies around 500 MeV/u, produced by in-flight fission of a primary ^{238}U beam. The results for both nuclei indicating the PDR and GDR excitation are shown in Fig. 1.7. The PDR strength was located at around 10 MeV and exhausted around 5% of the energy-weighted sum rule.

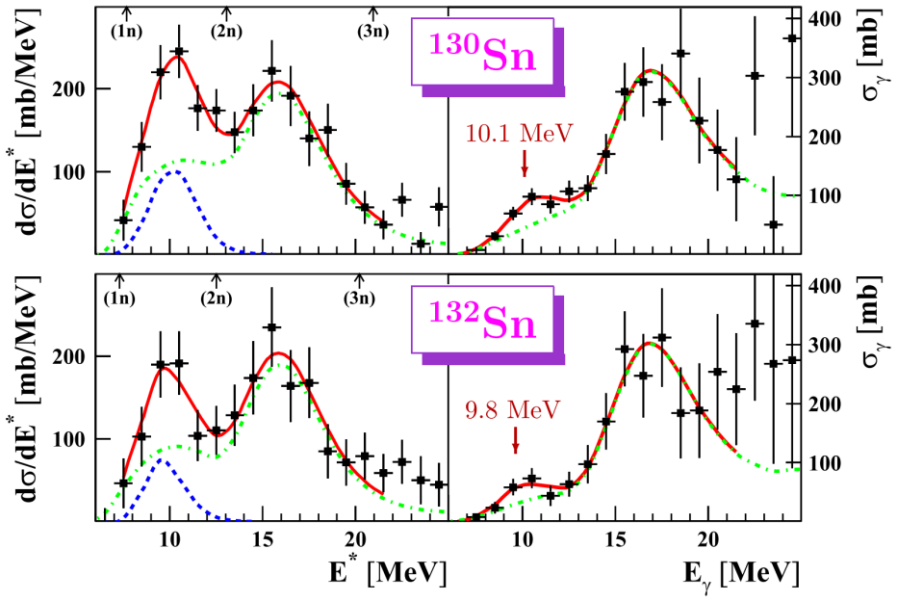

Figure 1.7: *Electromagnetic dissociation cross-sections (left panels) and deduced photo-neutron cross-sections (right panels) for ^{130}Sn and ^{132}Sn [Adr05, Kli07]. The dashed and dash-dotted curves show the fitted Gaussian and Lorentzian distributions assigned to the PDR (centroid indicated by an arrow) and GDR, respectively.*

Another method based on heavy-ion induced electromagnetic excitation has been employed by the RISING collaboration. In an experiment performed at GSI, the γ decay of ^{68}Ni projectiles at 600 MeV/u has been measured after excitation on gold target nuclei [Wie09]. As can be seen in Fig. 1.8, a peak-like structure was observed in the Doppler corrected γ spectrum above a background stemming mainly from statistical decay of the giant dipole resonance excited in the target nuclei or in the projectile. The authors estimated the PDR strength in ^{68}Ni for the 11-MeV peak corresponding to about 5% of the energy-weighted sum rule.

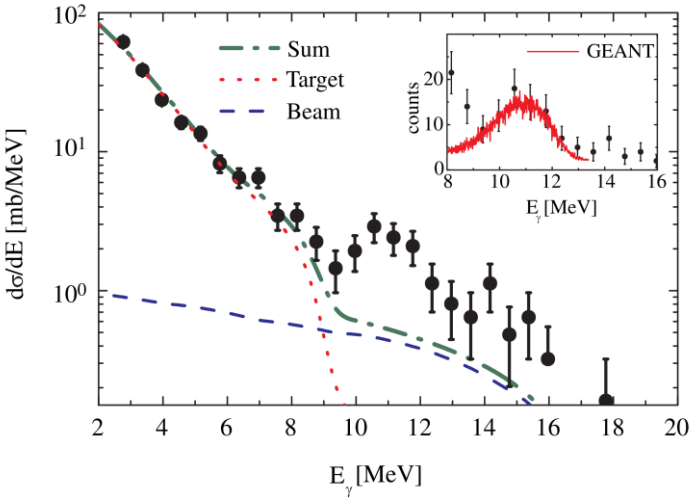

Figure 1.8: *Cross-section for electromagnetic excitation and photon decay for ^{68}Ni at 600 MeV/u on an Au target. Taken from Ref. [Wie09].*

Hadronic interactions in ion collisions

The experiments studying the dipole strength using the electromagnetic interaction are typically providing the energy and strength of electromagnetic transition. However, to obtain more information on the structure of excited states, it is possible to use the hadronic probes like alpha particle or heavy ions as complementary tools.

The first attempt has been done using the inelastic scattering of alpha particles at E_α = 137 MeV at forward angles for a different nuclei including ^{140}Ce [Sav06, End09], in order to make a comparison with the NRF data. The experiment has been performed at the Big-Byte spectrometer (BBS) at the AGOR cyclotron facility of KVI. Because of the isoscalar character of the α particles, one should expect mostly isoscalar excitations *via* nuclear interaction. However, the hadronic interaction is much less selective to the multipolarity of the transitions. Thus, it is not trivial to select only dipole transitions to the ground state. This is usually solved by measuring the scattered particles in coincidence with the emitted γ rays. The Table 1.1 shows the energy of excited dipole states, the reduced transition probabilities from NRF experiments and differential cross sections for their excitations using alpha scattering. The combined data from gamma and alpha scattering experiments for ^{140}Ce are shown in Fig. 1.9, indicating the characteristic feature of pygmy dipole states which is the splitting into two groups: low- and high-energy. Such effect was observed for different nuclei e.g. ^{94}Mo, ^{124}Sn, ^{138}Ba, and interpreted according to the isospin properties of applied probes and the sensitivity to radial transition densities of excited states. Conclusion was that the low-energy states are expected to have more isoscalar character and their transitions density is peaked on the surface, while high-energy states are of isovector nature and associated to the transitions towards the tail of the IVGDR. The microscopically calculated transition densities for the pygmy dipole states compared to the GDR will be introduced in next section (Fig. 1.10, right panel).

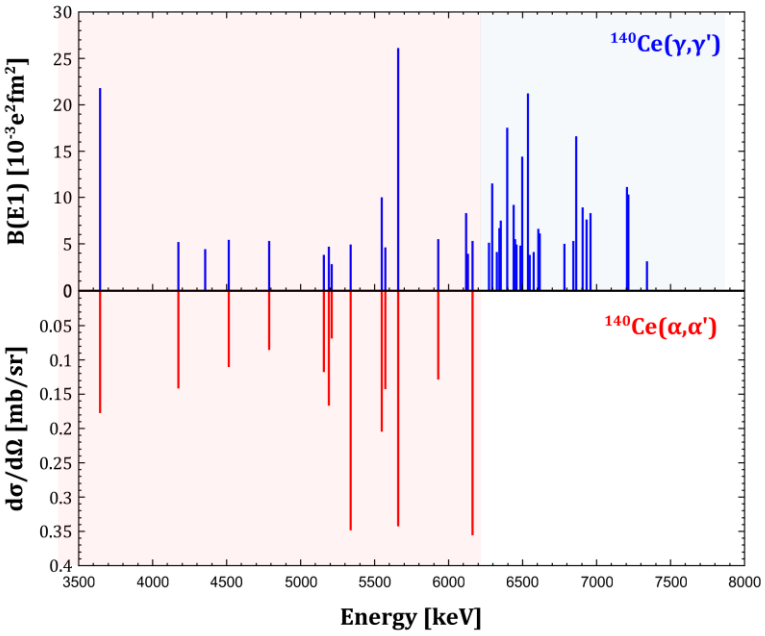

Figure 1.9: *The reduced transition probabilities B(E1) obtained in NRF experiment for ^{140}Ce (top panel) [Vol06] (top panel) compared to differential cross section for the excitation of pygmy dipole states using (α,α'γ) [End09] (bottom panel).*

This was a strong motivation to make another step forward, and apply heavy ions as another complementary probe. The detailed calculations [Bra15] performed for the systems: α + ^{90}Zr,^{208}Pb and ^{17}O + ^{90}Zr,^{208}Pb have shown much higher nuclear contribution to the excitation of isoscalar GDR as compared to Coulomb interaction. Furthermore, it was demonstrated that the excitation using ^{17}O at 20 MeV/u is dominated by nuclear interaction. This allowed to conclude that the ^{17}O at 20 MeV/u can be considered as an effective isoscalar probe. The beam of ^{17}O nuclei at the energy of 20 MeV/u was used in the experiments in LNL-Legnaro as an isoscalar probe to study the properties of pygmy dipole states with AGATA-Hector$^+$-TRACE setup. The method was applied to study a few nuclei (^{90}Zr [Cre15], ^{124}Sn [Pel14a], ^{140}Ce [Krz14, Krz16a] and ^{208}Pb [Cre14]) from different mass regions and of different internal structure. The overview of the method has been recently given by Bracco et al. [Bra15]. The particular case of spherical, semi-magic ^{140}Ce nucleus is the subject of this thesis. The details of inelastic scattering of heavy-ions with the focus on ^{17}O projectile will be discussed in Chapter 2.

1.3.2. Theoretical Models

First macroscopic approach to describe the low-lying dipole mode was the incompressible three fluid model (protons + neutrons of the core + excess neutrons) [Moh71]. This allowed to reproduce the energy of the pygmy dipole resonance known from experiments, however the PDR strength was too weak. Within modified model [Suz90], assuming existence of two fluids: core and neutron excess, it was possible to find reasonable agreement between the PDR strength and experimental data existed at that time for a few nuclei with N=82-126 [Iga86]. More recent approach was based on the model where the nucleus is treated as a spherical space of elastic continuous medium [Bas08] and investigated the PDR in terms of elastodynamics excitation mechanism suggesting the isoscalar nature of the mode.

The low-lying dipole modes were also intensively studied using different microscopic models (for an overview see [Paa07]):

- the Hartree-Fock plus random phase approximation (RPA) with Skyrme interactions or quasiparticle RPA (QRPA) [Sar04];
- the relativistic RPA (RRPA) [Vre01];
- the relativistic Hartree-Bogoliubov (RHB) plus the relativistic quasiparticle RPA (RQRPA) [Paa05];
- the relativistic quasiparticle time blocking approximation (RQTBA) [Lit08];
- the RRPA plus phonon coupling (PC) [Lit07];
- the QRPA plus the quasiparticle phonon coupling (QPM) [Tso04, Tso08].

The PDR in ^{140}Ce nucleus was studied [Paa09] using the fully self-consistent RQRPA based on the RHB using DD-ME2 effective nucleon-nucleon interaction. The left panel of Fig. 1.10 shows the calculated total E1 transition strength (solid line) and after selection of only isoscalar contribution (yellow area). There is a clear separation of the two structures above and below neutron separation energy (S_n). Calculated proton and neutron transition densities for these peaks are shown in right panel of Fig. 1.10 suggesting completely different underlying structure of studied excitation modes. While the state at higher energy reveals typical behaviour of isovector giant dipole resonance, which arise from neutrons oscillating out-of-phase versus protons, the lower lying state is more complex. In the interior of nucleus protons and neutrons oscillate in-phase, however, at the surface only neutron part contributes. This picture supports the interpretation of the strong isospin mixing of the PDR states. However, one may expect, that the PDR states should be much more fragmented that it is shown using RQRPA calculations.

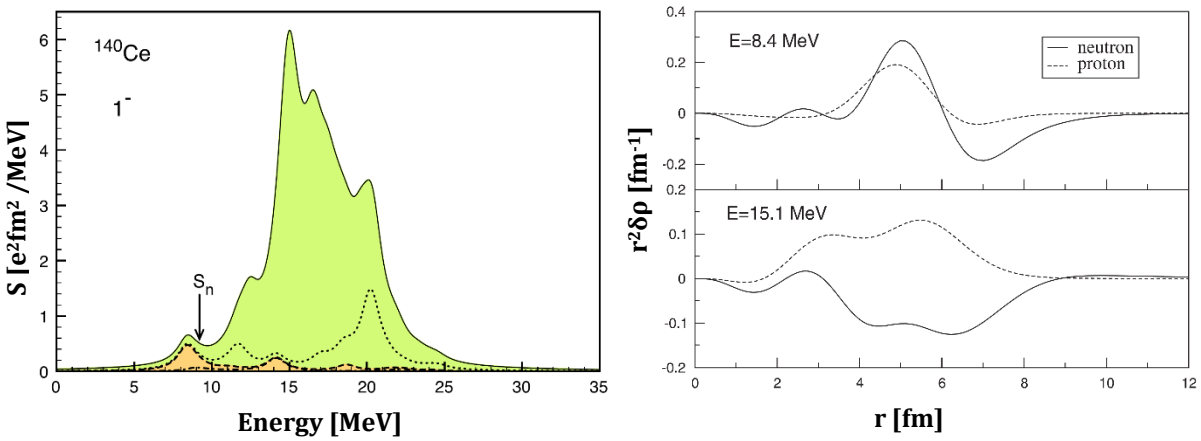

Figure 1.10: *Left panel: The total RHB + RQRPA E1 transition strength for ^{140}Ce. Yellow area indicates the isoscalar part of E1 excitations; Right panel: The RQRPA neutron and proton transition densities for the peaks at 8.4 MeV and 15.1 MeV excitation energy in ^{140}Ce.. Taken from Ref. [Paa09].*

Indeed, as already discussed by Paar et al [Paa09] the RQRPA does not include the effect of coupling to low-energy surface phonons which would enhance the effective nucleon mass and result in much more fragmented states and shifted to lower energies. This effect is included in RQTBA model and the additional calculations have been done for the purpose of the study presented in the thesis [Lit15]. The RQTBA calculations were done using NL3 effective nucleon-nucleon interaction. The crucial point is to determine well the lowest 2^+ phonon state (see also sec. 1.4) in order to correctly include the coupling effect between phonon and PDR states which causes the fragmentation of PDR. As it was revealed, in the case of ^{140}Ce the relativistic models are not able to reproduce well the lowest 2^+ (phonon) state, overestimating its value of around 1.5 MeV. Fig. 1.11 presents the comparison between RQRPA (black line) and RQTBA (red line) strength distributions for the ^{140}Ce [Lit15]. As expected, there is a shift of the pygmy dipole states to lower energies in RQTBA as compared to RQRPA (see Fig. 1.11), but it is still around 2 MeV above the experimental data (see Fig. 1.9). Also fragmentation of the PDR states is still not satisfactory in isoscalar channel, which was expected taking into account the difficulties with reproducing the lowest 2^+ state. It was further possible to adjust the energies of phonons and finally obtain higher fragmentation of the PDR strength as shown with blue lines in Fig. 1.11. Such fragmentation results in evolution of the transition densities starting from lower to higher energies.

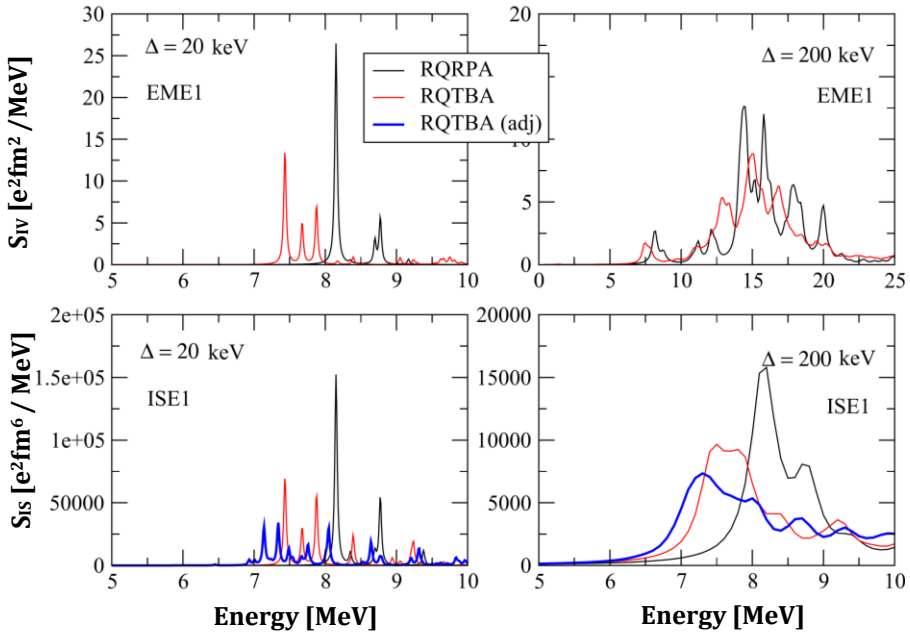

Figure 1.11: *Isovector (S_{IV}) (top panels) and isoscalar (S_{IS}) (bottom panels) strength distributions for ^{140}Ce obtained using RQRPA (DD-ME2) and RQTBA (NL3) models. Different smearing, Δ=20 keV (left panels) or 200 keV (right panels) are assumed [Lit15].*

It was discussed e.g. for ^{116}Sn case [Lit09b] and very similar behaviour was shown (see Fig. 1.12), that for the lowest RQTBA states the transition densities look similar to the RQRPA one, but because of the fragmentation, the amplitude of the density oscillations is about factor 3 smaller. However, since there are more states, in total they can effectively give a similar contribution to the cross section. Therefore, it should be reasonable enough to use RQRPA transition densities. The results from RQRPA (Table 1.2) will be therefore used in this thesis to estimate: the microscopic form factor for the excitation of 1^- pygmy states, the isoscalar energy-weighted sum rule (ISEWSR) of the PDR states and its strength (S_{IS}).

Table 1.2: *The excitation energy (E_x) of 1^- pygmy state in ^{140}Ce, the corresponding isoscalar energy-weighted sum rule (ISEWSR) and its strength (S_{IS}) and also reduced transition probability, B(E1), calculated with the RQRPA model [Paa09].*

E_x [MeV]	ISEWSR [%]	S_{IS} [e²fm⁶]	B(E1) [e²fm²]
8.39	4.14	$1.2 \cdot 10^4$	1.04

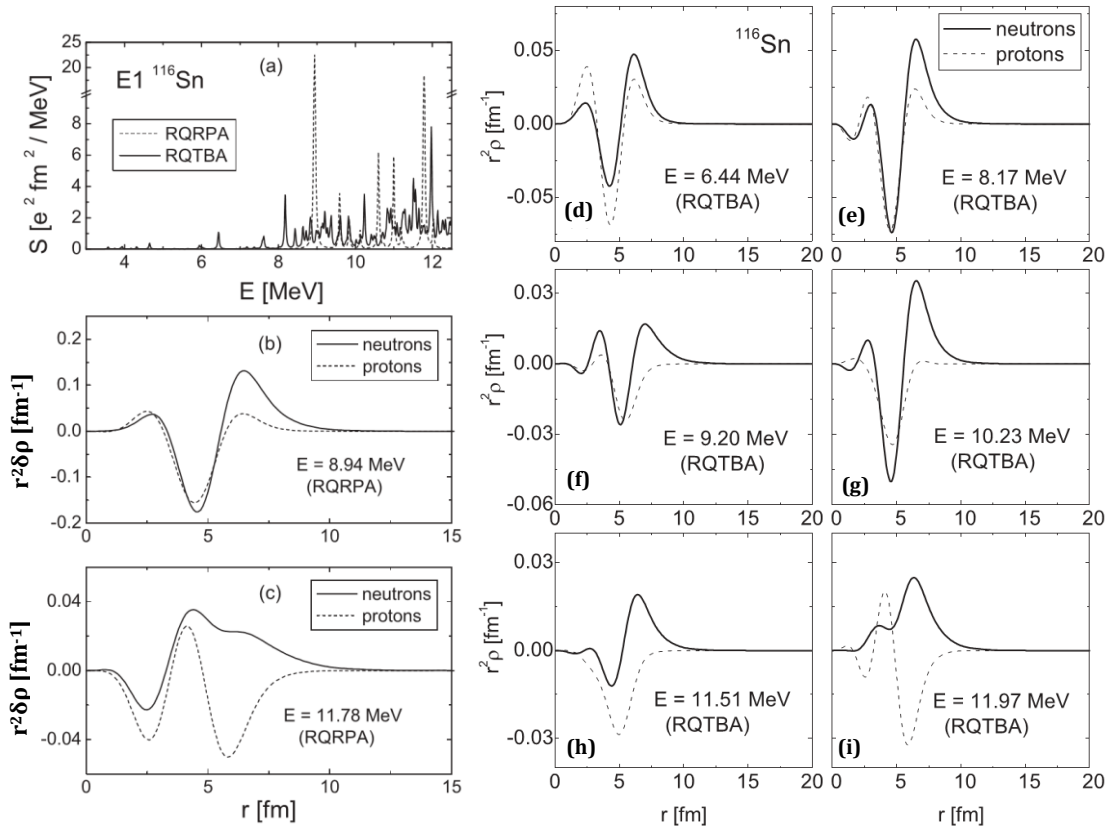

Figure 1.12: *(a) Low-lying part of the dipole spectrum in ^{116}Sn, calculated in RQRPA and RQTBA models. (b) RQRPA transition densities for the most intensive peaks at 8.94 MeV and (c) 11.78 MeV. RQTBA transition densities for states at 6.44 MeV (d), 8.17 MeV (e), 9.2 MeV (f), 10.23 MeV (g), 11.51 (h), 11.97 MeV (i). Taken from Ref. [Lit09b].*

Another interesting picture of low-lying E1 strength was obtained by analysing the current transition densities, which are analogous to the velocity fields (schematically shown in Fig. 1.13) [Rep13]. The aim was to investigate the interplay between the PDR, toroidal resonance (TR) and anisotropic compression resonance (CR). The authors performed calculations for ^{208}Pb using RPA with Skyrme forces in a fully self-consistence manner. The final conclusion was that the low-lying dipole strength has two regions of different structure: lower-lying of dominantly isoscalar vertical toroidal mode, and higher-lying with a mixed toroidal/compression/linear flow. Unfortunately, it is very difficult to experimentally probe the toroidal mode so this is definitely a challenge for the future experiment.

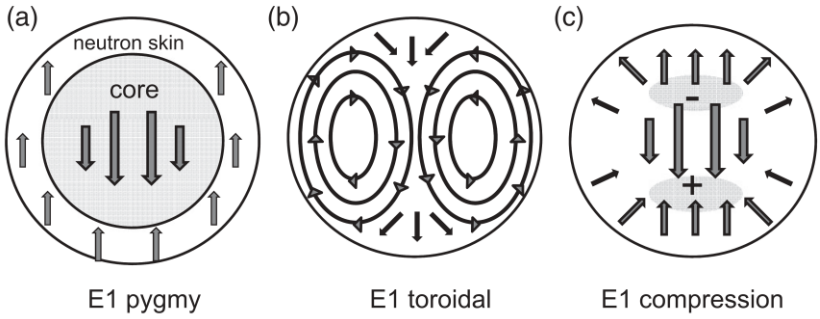

Figure 1.13: *Schematic velocity fields for the E1 pygmy (a), toroidal (b), and high-energy compressional (c) flows. In (c), the compression (+) and decompression (−) regions, characterized by increased and decreased density, are marked. Taken from Ref. [Rep13].*

The PDR properties have been also studied along isotopic chains. Example of such investigation is shown in Fig. 1.14 where RHB + RQRPA calculations for the isotopes of three spherical nuclei: Sn, Te and Xe are summarized. It can be observed in left panel that the PDR strength increases up to certain mass, then it decreases until the shell closure at N = 82. Afterwards, it increases rapidly. This allows to conclude that the PDR strength is strongly correlated with the number of valence neutrons above the closed shells. Furthermore, the average PDR energy, when considered as one peak, decreases with increasing mass (right panel of Fig. 1.14).

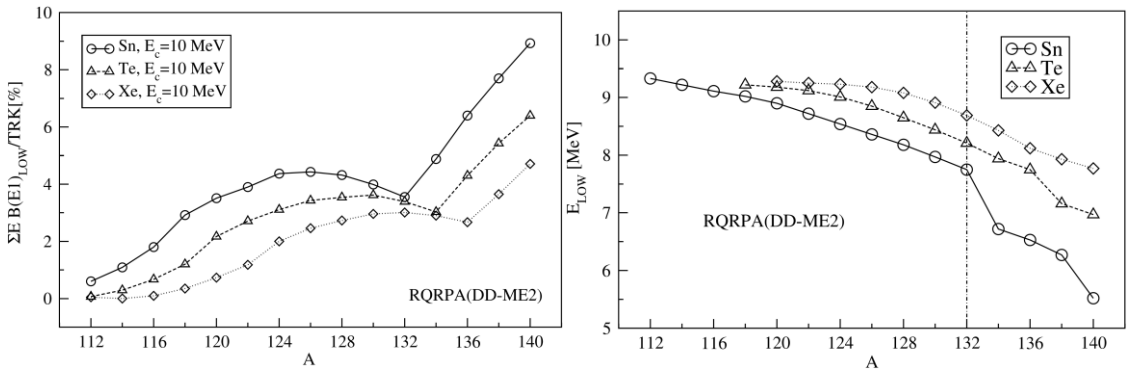

Figure 1.14: *Left panel: The RHB + RQRPA energy-weighted dipole strength, integrated up to the energy cut-off E_c = 10 MeV, and plotted in per cent of the TRK (Thomas-Reiche-Kuhn) sum rule; Right panel: The calculated PDR peak energies (E_{LOW}) for Sn, Te and Xe isotopes. Taken from Ref. [Paa07].*

1.3.3. Implications and Applications

The gross feature of E1 response, which is mainly related to the IVGDR, is well described in many microscopic models. Meanwhile, the fine structure connected with the PDR is much more dependent on the details of the nuclear force, thus the microscopic description of this mode differs very much between models. This stimulated an intensive growth in many microscopic calculations. However, the PDR is not only an interesting nuclear structure phenomenon. It has also many important implications to different subjects.

One of the basic applications of low-lying E1 strength comes from possible relation between the PDR strength and thickness of the neutron-skin, which is formed by excess of neutrons outside the core of nucleus [Piek11]. The neutron-skin is determined by the symmetry energy of the equation of state (EOS) and directly linked to its parameters [Bro00]. This is of importance, as the EOS describes dense astrophysical objects such as the neutron stars [Piek12]. At the base of E1 strength, it is possible to determine the dipole polarizability, which can be described as follows:

$$\propto_D = \frac{\hbar c}{2\pi^2 e^2} \int \frac{\sigma_\gamma}{\omega^2} d\omega \qquad (1.20)$$

where σ_γ is the photo-absorption cross section, ω is the excitation energy.

It has been shown [Piek11, Bro00, Rei10] that this parameter can be used to determine the neutron-skin thickness (see right panel of Fig. 1.15). The advantage of using the dipole polarizability is that the PDR strength doesn't have to be separated from other contributions like the tail of the GDR, which is a very difficult experimental task. Furthermore, it is less sensitive to the structure of the low-lying E1 strength.

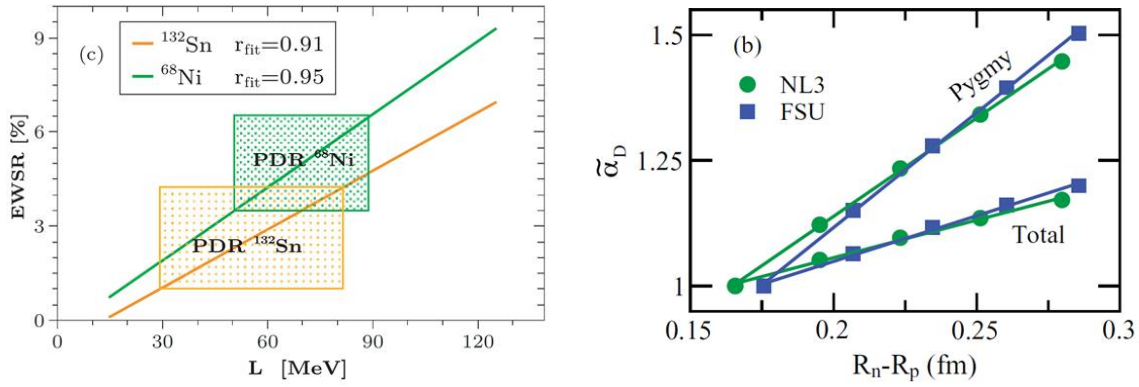

Figure 1.15: *Left panel: The correlation between slope parameter of the symmetry energy, L and the percentage of the TRK sum rule exhausted by PDR for ^{68}Ni and ^{132}Sn [Car10]; Right panel: Fractional changes in dipole polarizability for ^{68}Ni as a function of neutron skin thickness of ^{208}Pb [Piek11].*

On the other hand, the slope of the correlation between the PDR fraction of dipole polarizability and neutron-skin thickness is steeper as compared to the total dipole polarizability (see Fig. 1.15, right panel) [Piek11]. Another example is the relation between PDR and the symmetry energy, which is presented in left panel of Fig. 1.15. The authors were able to show a correlation between percentage of EWSR exhausted by PDR and the so-called slope parameter (L) of the symmetry energy [Car10].

Another key role of the low-lying dipole strength is its influence on reaction rates in the astrophysical r-process [Gor98, Gor04, Lit09a] which synthetizes about 50% of the abundance of the elements heavier than iron. Important ingredient in calculation of the neutron capture cross-sections is the photo-absorption cross-section σ_γ, which is directly connected to the γ-ray strength function. In particular, the shape of σ_γ in the region of particle separation energy is important in calculation of the neutron capture cross sections [Lit09a].

Finally, the observed additional *E1* strength might affect several astrophysical processes: the synthesis of nuclei in explosive stellar burning phases [Gor04], the photo-disintegration of ultra-high-energy cosmic rays [Kha05] and may be important for generating neutrons in stars [Ber69].

1.4. TWO-PHONON STATE

The lowest excited states of nuclei with near closed shells are usually a 2^+ and 3^- corresponding to quadrupole and octupole oscillations of the nuclear surface. In the frame of hydrodynamic nuclear model, to these collective surface vibrations one associates phonons with specific multipolarities. Coupling of the two different phonons ($2^+ \otimes 3^-$) may result in observation of 1^- state. The energy of such state should be the sum energy of the single-phonon constituents. Systematics of the ratio between energy of the 1^- state and the sum energy of 2^+ and 3^- state for a broad mass range has been shown to be equal to 1 within 10% uncertainty [Wil98] (see Fig. 1.16, right panel). Moreover, the existence of very harmonic quadrupole-octupole coupling was shown for the ^{142}Nd, ^{144}Nd, ^{144}Sm nuclei [Wil98], by observing the *E2* transition to the single-phonon 3^- state and demonstrating the B($E2$; $1^- \rightarrow 3^-$) to be equal to B($E2$; $2^+ \rightarrow 0^+$). These results are illustrated in left panel of Fig. 1.16.

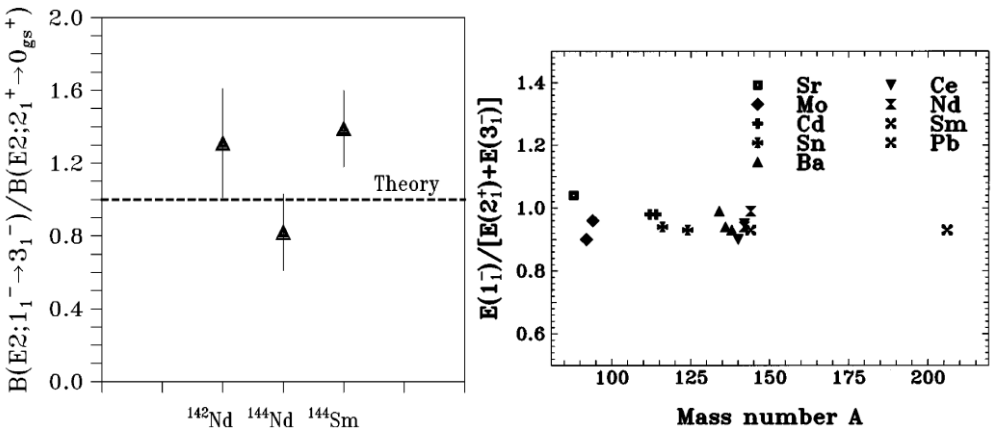

Figure 1.16: *Left panel: The ratio of the experimental B(E2; 1⁻ → 3⁻) relative to the B(E2; 2⁺ → 0⁺) value of the A=140 mass region; Right panel: Systematics of the ratio between energy of the 1⁻ state and the sum energy of 2⁺ and 3⁻ state versus the mass number A [Wil98].*

In the case of ^{140}Ce, the interpretation of the first 1^- state as two-phonon is not as evident as in previous cases. Fig. 1.17 shows the partial level scheme of ^{140}Ce including the discussed 2^+ and 3^- phonon states as well as first 1^- state.

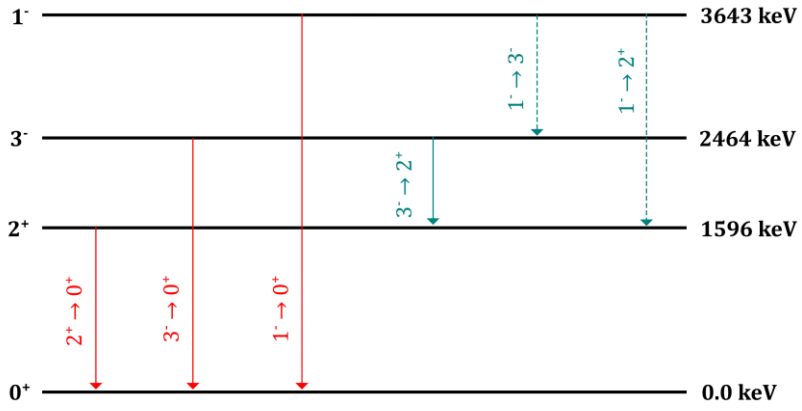

Figure 1.17: *Partial level scheme showing the first quadrupole and octupole states and the candidate for the 1⁻ two-phonon state in ^{140}Ce. Gamma-transitions to the ground state are marked in red.*

Gamma transitions to the ground state are marked in red. The candidate for the two-phonon state is found at the energy of 3643 keV. The sum energy of the 2^+ and 3^- single-phonon components is 4060 keV, which is ~10% higher than the energy of the two-phonon. This is consistent with the systematics for other nuclei in this mass region [Wil98] (See Fig. 1.16, right panel). However, this shift in energy is an indication of anharmonicity, which is due to the coupling among states of one-, two- and three-phonon states [Fal03]. The experiments using the

Nuclear Resonance Fluorescence (NRF) technique have not found for ^{140}Ce [Vol06, Her97] the γ-transitions from two-phonon state to the single-phonon constituents, which would show the pure harmonic coupling of the two phonons. The theory expects the branching ratio between $1^- \rightarrow 2^+$ and $1^- \rightarrow 0^+$ to be 0.45% [Gri94]. Such branching is very difficult to observe. Another support for the quadrupole-octupole nature of these state comes from the observation of *E1* γ-transition, between 3^- and 2^+ states. A close correlation between the *E1* transition strengths of the $1^- \rightarrow 0^+$ transition and the $3^- \rightarrow 2^+$ transition has been demonstrated for many nuclei around N = 82 including ^{140}Ce [Pie99].

The issue of two-phonon 1^- state will be addressed in the thesis.

Chapter 2. INELASTIC SCATTERING OF HEAVY IONS

In case of the experiment, which is a subject of this thesis, the inelastic scattering of ^{17}O at the bombarding energy of 340 MeV (20MeV/u) in the laboratory frame was used to excite the high-lying states. The general introduction to the process of heavy ions scattering will be briefly given in sec. 2.1, focusing on introduction to the concept of the cross sections and differentiation between elastic and inelastic scattering as well as Coulomb and nuclear scattering. Then, the brief explanation of the Distorted Wave Born Approximation (DWBA) as a method to describe the heavy-ions scattering will be given (sec. 2.2). Finally, the procedure of calculating the microscopic form factors that are necessary to describe the excitation of pygmy dipole states with the DWBA approach will be presented.

2.1. INTRODUCTION TO HEAVY-IONS SCATTERING

The brief introduction to the heavy-ions scattering will be given in this section, taking profit mostly from Ref. [Kra88].

A nuclear reaction can be written as:

$$a + A \rightarrow b + B \tag{2.1}$$

where a is the projectile hitting the target A (usually stationary in laboratory frame of reference), and b and B are the projectile-like target-like products respectively.

If the incident and outgoing particles (a and b) are the same as the nuclei A and B, it is a scattering process, that can be elastic if b and B are in the ground state, or inelastic if b or B are in excited state.

In order to estimate the relative probability for the reaction to occur, the concept of the cross section has been introduced. One may consider the geometry that is shown in Fig. 2.1. A detector, that measures the outgoing particles b emitted in a direction (θ, ϕ) with respect to the beam direction, defines a solid angle $d\Omega$ at the target nucleus. The reaction cross section can be expressed as follows:

$$\sigma = \frac{R_b}{I_a N} \ [b] \tag{2.2}$$

where I_a is the number of incident particles per unit time, N is the number of target nuclei per area unit shown to the beam and R_b is the rate of outgoing particles.

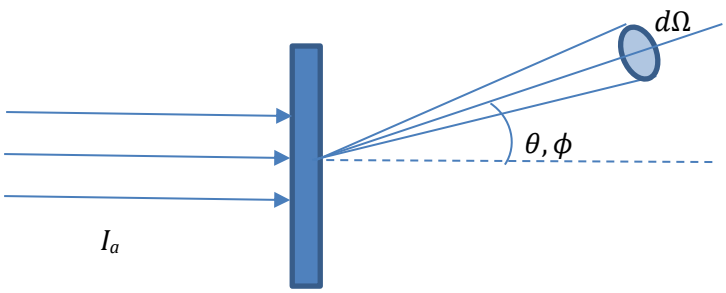

Figure 2.1: *Reaction geometry showing incident beam, target, and outgoing particles.*

It is convenient to use a unit of barn: 1 b = 100 fm^2, which is a geometrical area of typical nucleus with radius R = 6 fm.

Because the detector sees only a part of outgoing particles, only a fraction of R_b is detected. Furthermore, the probability of particles emission is not uniform in all direction, so there is some angular distribution that can be expressed as a function $r(\theta, \phi)$. Then $R_b = r(\theta, \phi)d\Omega/4\pi$ and the differential cross section can be defined as follows:

$$\frac{d\sigma}{d\Omega} = \frac{r(\theta, \phi)}{4\pi I_a N} \quad [\frac{b}{sr}] \tag{2.3}$$

The reaction cross section can be obtained by integrating the differential cross section over all angles. As $d\Omega = \sin\theta d\theta d\,\phi$, the reaction cross section is:

$$\sigma = \int \frac{d\sigma}{d\Omega} d\Omega = \int_0^{\pi} \sin\theta d\theta \int_0^{2\pi} d\,\phi \frac{d\sigma}{d\Omega} \tag{2.4}$$

The scattering may occur due to the electric (Coulomb) or nuclear interaction. These two kinds of scattering processes will now be briefly discussed.

2.1.1. Coulomb scattering

The scattering of a charged particle may occur due to the repulsion of the electric field of a target nucleus. Such scattering can be either elastic or inelastic.

Elastic Coulomb scattering is called a *Rutherford scattering*. The geometry that illustrates such reaction is shown in Fig. 2.2. The particle approaches the target nucleus along the straight line then it would pass at a distance *b (impact parameter)* from the nucleus without a repulsive force. The scattered particle due to a Coulomb interaction follows the hyperbolic path. Very far from the nucleus the incident particle has negligible Coulomb potential energy. When passing close to the target nucleus, the particle reaches the minimum separation distance r_{min}, which depends on b. For the head-on collision ($b = 0$), the particle reaches the point in which it has exchanged

all initial kinetic energy for Coulomb potential energy. This distance denoted as d is called *distance of closest approach*. Because the Coulomb force is symmetric, the scattering has cylindrical symmetry and the cross section is independent of the azimuthal angle ϕ.

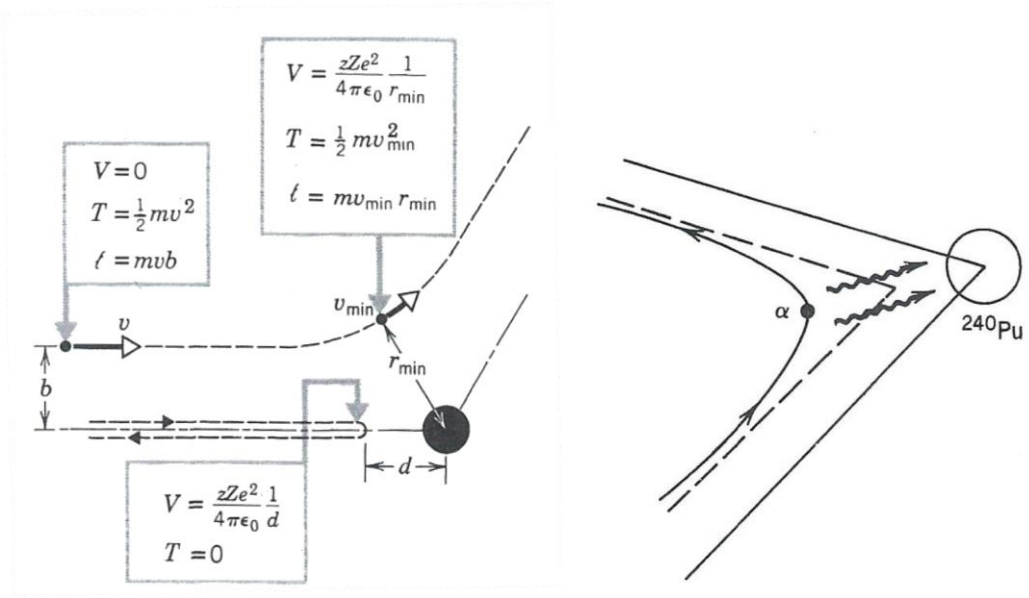

Figure 2.2: *left panel: Geometry of the Rutherford scattering; right panel: Scheme of the inelastic Coulomb scattering. The projectile exchanges energy with the target through the Coulomb interaction and both reaction partners can be driven to the excited state. Taken from Ref. [Kra88].*

The formula for a differential cross section for Rutherford scattering [Kra88]:

$$\frac{d\sigma}{d\Omega} = \left(\frac{zZe^2}{4\pi\varepsilon_0}\right)^2 \left(\frac{1}{4T_a}\right)^2 \frac{1}{sin^4\frac{\theta}{2}} \tag{2.5}$$

where ze is the charge of the projectile and Ze of the target, T_a is the kinetic energy of the projectile, and θ is the scattering angle.

Inelastic Coulomb scattering is called *Coulomb excitation*. The nucleus encountered during this process is left in an excited state from which it de-excites by γ-rays emission. For fast beams (E > 10MeV/u) this process can be considered as the emission and absorption of virtual photons, with most likely mode being E2. This process can be successfully applied e.g. to study the first excited 2^+ states in even-Z, even-N nuclei. The example of such process is shown schematically in right panel of Fig. 2.2.

2.1.2. Nuclear scattering

The *elastic nuclear scattering* of particles is similar to the diffraction of light by an opaque disk in optics. In the optical case, diffraction at the sharp edge results in a series of maxima and minima (see left panel of Fig. 2.3). The minima are almost equally spaced and the maxima are steadily and substantially decreasing intensity. The nucleus is strongly absorbing object for nucleons, thus the analogy with the opaque disk is valid. In the case of charged particles scattering, there is an interference between nuclear and Coulomb scattering. In order to observe only the nuclear scattering, one can use neutrons as scattering particles as they are uncharged. Fig 2.3 (right panel) presents the results of an elastic neutron scattering showing very similar diffraction pattern as in optical case. However, in the case of nuclear scattering, the minima do not fall into zero, which is a result of the diffuseness of the nuclear surface (nuclei does not have a sharp edges).

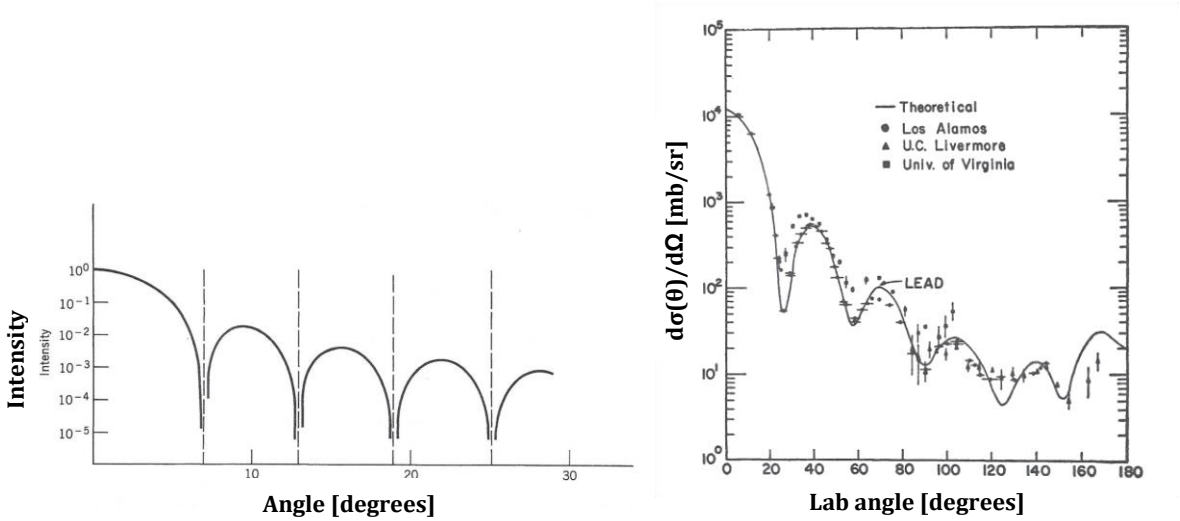

Figure 2.3: *Left panel: Diffraction pattern of light incident in a circular aperture ; Right panel: Elastic scattering of 14-MeV neutrons on Pb. Taken from Ref. [Kra88].*

The *inelastic nuclear scattering* occurs when nucleus absorbs energy from the projectile and reaches the excited state. The measurement of scattered particles energy at a given angle shows a single elastic peak (highest energy of scattered particles) and inelastic peaks corresponding to specific excited states of target nucleus. The location of the peaks gives information about relative energy of the excited states while their relative height about the relative cross sections for excitation of these states. The measurement of angular distributions of scattered particles for a given excited state allows to learn the spin and parity of this state.

2.2. DISTORTED WAVE BORN APPROXIMATION (DWBA)

The scattering process at the intermediate energies, 10-100 MeV/u, is accurately described within the Distorted Wave Born Approximation (DWBA). The brief overview of the model will be given in this section, taking profit from Ref [Bass80]. In the thesis, the DWBA analysis was performed to calculate the cross sections at the preparatory phase of the experiment and also for the analysis of the different excitations especially in the PDR energy region to be compared with experimentally obtained values.

Basic assumption of all distorted wave theories is that when two nuclei collide, the dominant processes that occur are: elastic scattering and absorption. These two phenomena can be described by the optical model potential. In such model, the elastic process is described exactly, within limitations of optical models, while other reaction channels are treated as perturbation. In the DWBA, the *differential cross section* is related to the transition coefficient T_{fi} defined as follows:

$$\frac{d\sigma}{d\Omega} = \left(\frac{\mu}{2\pi\hbar^2}\right)^2 \left(\frac{k_f}{k_i}\right) \sum \left|T_{fi}\right|^2 \tag{2.6}$$

where μ is a reduced mass, k_f and k_i are the wavenumbers of final and initial states.

The $\sum\left|T_{fi}\right|^2$ means summation over final state quantum numbers an averaging over initial state quantum numbers. The *transmission coefficient* is expressed as:

$$T_{fi} = \int d^3\vec{r}\, \chi_f^{(-)*}\left(\overrightarrow{k_f}, \vec{r}\right) \langle \psi_f^* | V_{if} | \psi_i \rangle \chi_i^{(+)}\left(\overrightarrow{k_i}, \vec{r}\right) \tag{2.7}$$

where $\chi_i^{(+)}$ and $\chi_f^{(-)}$ are the "distorted waves", that describe the relative motion of the fragments in the initial and final channels under the influence of the deformation-independent part of the two-body interaction.

These functions are calculated as a numerical solution of the Schrödinger equation with appropriate *optical model potentials*. The matrix elements $\langle \psi_f^* | V_{if} | \psi_i \rangle$ link the intrinsic wave functions in the initial and final states via the interaction V_{if} which induces the transition. The radial part of the matrix element is called the *form factor* $F_\lambda(r)$. If the nucleus is deformed collective degrees of freedom have to be considered. For a collective transition of multipole order L, form factor is expressed as:

$$F_L(r) = \frac{4\pi[B(EL)\uparrow]^{1/2}}{2L+1} \frac{Z_p e}{r^{L+1}} + \delta_V(L) \frac{dV(r)}{dr} + i\delta_w(L) \frac{dW(r)}{dr} \tag{2.8}$$

where Z_p is the atomic number of the projectile, $B(EL)\uparrow$ is the reduced transition probability, δ_V and δ_w are the deformation lengths, V(r) and W(r) are the real and imaginary part of the optical potential.

The deformation lengths are matrix elements between the states involved in the transition determining the strength of the nuclear excitation and are related to deformation parameter (β). The first term is related to the Coulomb part of the interaction while second and third term are associated to the nuclear part represented by the optical potential (real and imaginary parts).

In this thesis, the DWBA calculations were performed with the widely used FRESCO code [Tho88]. The approach requires the optical potential to describe the incoming and outgoing waves and a form factor containing the information on the nuclear structure aspects of the reaction. The idea of calculating the cross sections for the elastic scattering and inelastic excitation will be briefly discussed following Refs. [Bass80, Hor91].

2.2.1. Elastic scattering

For the calculation of elastic scattering, the FRESCO uses the standard *optical model*. In this model the interaction between the projectile and target is described in terms of a complex potential, whose real part accounts for the elastic process and imaginary part accounts for the loss of flux in the elastic channel going to any other channels.

The elastic scattering cross section is evaluated from the expression:

$$\frac{d\sigma}{d\Omega}(\theta) = |f(\theta)|^2 \tag{2.9}$$

where $f(\theta)$ *is the scattering amplitude.*

The scattering amplitude is related to the scattering wave function:

$$\psi(K,R) \rightarrow e^{iKR} + f(\theta)\frac{e^{iKR}}{R} \tag{2.10}$$

where K denotes the incident angular momentum of the projectile (in centre of mass system) and R is the relative coordinate between projectile and target.

This in turn is calculated from the Schrodinger equation for the complex potential *U(R)*:

$$\left[\frac{\hbar^2}{2\mu}\nabla^2 + U(R) - E\right]\psi(K,R) = 0 \tag{2.11}$$

where μ is the reduced mass and E is the energy in the centre of mass system.

The potential is composed of the two components: nuclear and Coulomb potential. The *nuclear potential* was assumed to be of a Woods-Saxon type (see Fig. 2.4):

$$U(r) = -Vf(x_V) - iWf(x_W) \tag{2.12}$$

and:

$$f(x_V) = \frac{1}{1 + e^{\frac{r-R_V}{a_V}}} \ , \qquad f(x_W) = \frac{1}{1 + e^{\frac{r-R_W}{a_W}}} \tag{2.13}$$

$$R_V = r_V \left(A_p^{1/3} + A_t^{1/3} \right) , \qquad R_W = r_W \left(A_p^{1/3} + A_t^{1/3} \right) \tag{2.14}$$

where *V, W are depths, R_v, Rw are the radii and a_v, a_w are diffuseness of the real and imaginary potential respectively. A_p and A_t are the masses of the projectile and target nuclei respectively.*

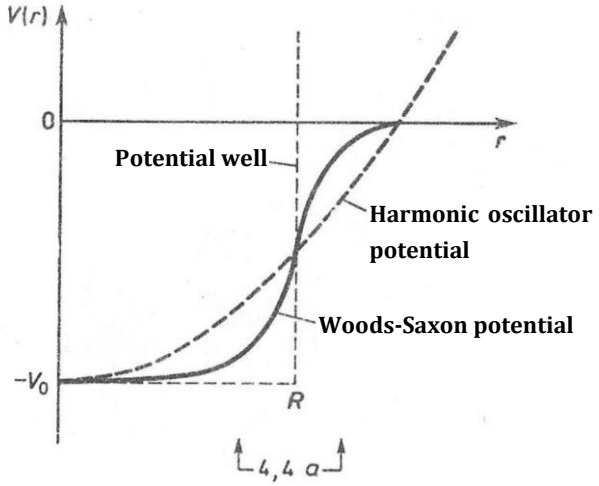

Figure 2.4: *Woods-Saxon potential (solid line) with depth (V_0), radius (R) and diffuseness (a) parameters compared to harmonic oscillator potential and potential well.*

The *Coulomb potential* was also added and assumed to be of a point charge interacting with a uniform charge distribution having radius:

$$R_C = r_C \left(A_p^{1/3} + A_t^{1/3} \right) \tag{2.15}$$

where r_C is the charge radius parameter.

In the case of ^{140}Ce which is a subject of this thesis, the optical model parameters were evaluated at the base of the ones deduced from the experimental cross sections of elastic scattering for similar reaction: ^{16}O+^{90}Zr,^{208}Pb at 22 MeV/u [Sjo84] presented in Table 2.1.

Table 2.1: *Optical model potential parameters evaluated for scattering of ^{16}O at E_{beam} = 400 MeV [Sjo84].*

reaction	**V** [MeV]	**R_v** [fm]	**r_c** [fm]	**a_v** [fm]	**W** [MeV]	**R_w** [fm]	**a_w** [fm]
^{16}O + ^{90}Zr at 25 MeV/u	40	1.15	1.2	0.671	26	1.15	0.671
^{16}O + ^{208}Pb at 25 MeV/u	60	1.17	1.2	0.665	38	1.17	0.665

The results of comparing the experimental and calculated differential cross sections divided by the Rutherford cross sections are shown in Fig. 2.5. It shows a characteristic behaviour of the elastic scattering, which up to certain angle, which is called grazing, is close to the Rutherford type but then the cross section drops which is due to nuclear component of the interaction.

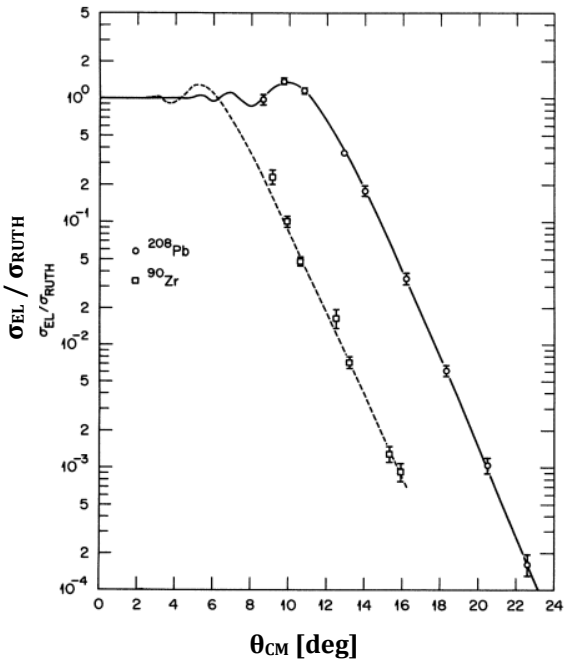

Figure 2.5: *Elastic scattering angular distributions for the 400 MeV ^{16}O ions on ^{208}Pb and ^{90}Zr compared with optical model calculations. Taken from Ref. [Sjo84].*

As in previous cases, for ^{140}Ce case the real and imaginary parts of radii and diffuseness were set equal. The depth of the real and imaginary parts, as well as the radii and diffuseness of the potential were calculated just by assuming their proportion to the mass of a nucleus. The obtained parameters as well as the results for ^{140}Ce will be discussed later in sec. 5.4.1.

2.2.2. *Inelastic scattering*

The cross sections calculations for the excitation of states with different angular momentum were also performed with DWBA approach using the *deformed optical model*. It uses the same parameters of the optical model that are evaluated for the elastic scattering but takes into account the deformation parameters. The model constitutes of the Coulomb (H_L^C) and nuclear (H_L^N) parts for the angular momentum transfer L.

Nuclear transition potential is considered as:

$$H_L^N = -\delta_V(L)\frac{dV(r)}{dr} - i\delta_W(L)\frac{dW(r)}{dr} \tag{2.16}$$

where V(r) and W(r) are the real and imaginary part of the optical potential that were used for the elastic scattering data. $\delta_V(L), \delta_w(L)$ *are the real and imaginary deformation lengths.*

In this particular calculations, the real and the imaginary deformation lengths are assumed equal: $\delta_V(L) = \delta_w(L) = \delta_L$.

Coulomb interaction can be treated as a multipole expansion between a point charge and a uniformly charged sphere with radius R_C, in a form:

$$H_L^C = \frac{4\pi Z_p e}{2L+1}[B(EL)\uparrow]^{1/2} \times \begin{cases} {r^L}/{R_C^{2L+1}} & , r < R_C \\ {1}/{r^{L+1}} & , r \geq R_C \end{cases} \tag{2.17}$$

where Z_p *is the atomic number of the projectile and the* $B(EL)\uparrow$ *is the reduced transition probability.*

In terms of the collective model the reduced transition probability can be directly related to the Coulomb deformation length $\delta_C(L)$ as follows:

$$[B(EL)\uparrow]^{1/2} = \frac{3}{4\pi} Z_t e \delta_C(L) \tag{2.18}$$

where Z_t *is the atomic number of the target*

In order to calculate the inelastic excitations, the FRESCO code bases on collective model for the nuclear part of the effective interaction as well as the deformation of the excited level. As seen from Eq. 2.18, the Coulomb deformation is related to the square root of reduced transition probability. For the nuclear deformation, the so-called reduced deformation length, *RDEF(L)* is introduced and expressed as follows:

$$RDEF(L) = \sqrt{B(E, 0 \to L)} \cdot \frac{4\pi}{3ZR^{L-1}} \tag{2.19}$$

where $R = 1.2A^{1/3}$

In the analysis presented in the thesis, the $B(EL)\uparrow$ values are taken from other literature. For the pygmy dipole states, the $B(EL)\uparrow$ is manly from the NRF experiments (see Table 1.1).

2.2.3. Microscopic Form Factors

As it was introduced in the previous section, the standard FRESCO calculations of the inelastic excitations use the deformed optical model. In this model, the form factor that takes into account the specific formation of the excitation bases on the collective rotor model. This model was demonstrated to well reproduce the data of the IVGDR excitation. As it will be presented in the thesis, the standard collective model form factor is not relevant for DWBA cross section calculations of the 1^- pygmy states excitation that are located below the tail of the GDR. These become obvious when one considers completely different character of transitions densities associated to these different modes. In order to use relevant form factor, which would take into account a specific nature of the PDR, the double-folding procedure [Sat83] was applied to calculate the appropriate form factor that takes into account the neutron and proton transition densities. The procedure will now be briefly recalled following Ref. [Lan15].

The double-folding potential between two heavy ions is obtained by integrating the nucleon-nucleon interaction over the densities of the two nuclei. In a similar way the form factors are constructed by using the density of one nucleus on one side and the transition densities of the exited nucleus on the other side. The internal structure of the nucleus can be described by means of many-body models (often HF plus RPA calculations), which give microscopic neutron and proton transition densities. Then, the isospin-dependent part of the nucleon-nucleon interaction should be additionally included:

$$v_{12} = v_0(r_{12}) + v_1(r_{12})\tau_1 \cdot \tau_2 \tag{2.20}$$

where v_0 is the isoscalar part that generates an isoscalar ion-ion potential and the v_1 is an isovector term that gives an isospin-dependant folding potential. τ_1 and τ_2 are the isospins of the nucleons.

Finally, the form factor having the isoscalar (F_0) and isovector (F_1) components is given by:

$$F_0 = \iint \left[\delta\rho_n^A(r_1) + \delta\rho_p^A(r_1)\right] \times v_0(r_{12})\left[\rho_n^B(r_2) + \rho_p^B(r_2)\right] r_1^2 dr_1 r_2^2 dr_2 \tag{2.21}$$

$$F_1 = \iint \left[\delta\rho_n^A(r_1) - \delta\rho_p^A(r_1)\right] \times v_1(r_{12})\left[\rho_n^B(r_2) - \rho_p^B(r_2)\right] r_1^2 dr_1 r_2^2 dr_2 \tag{2.22}$$

where $\delta\rho_n$ and $\delta\rho_p$ are the neutron and proton transition densities of the state under study of nucleus A which is excited by the mean field of nucleus B, ρ_n and ρ_p are the neutron and proton densities of the nucleus B.

In specific case when ρ_n/ρ_p=(N/Z), then the isovector form factor is zero when one or both partner of the reaction have N=Z [Sat83].

This procedure, using as a potential the Reid-type version of M3Y nucleon-nucleon interaction, was applied to calculate the inelastic scattering of ^{17}O at 20 MeV/u [Bra15]. The most detailed calculations were done for a ^{90}Zr nucleus. The calculated proton and neutron transition densities for the PDR, IVGDR and ISGDR are shown in Fig. 2.6. The corresponding form factors are shown in Fig. 2.7.

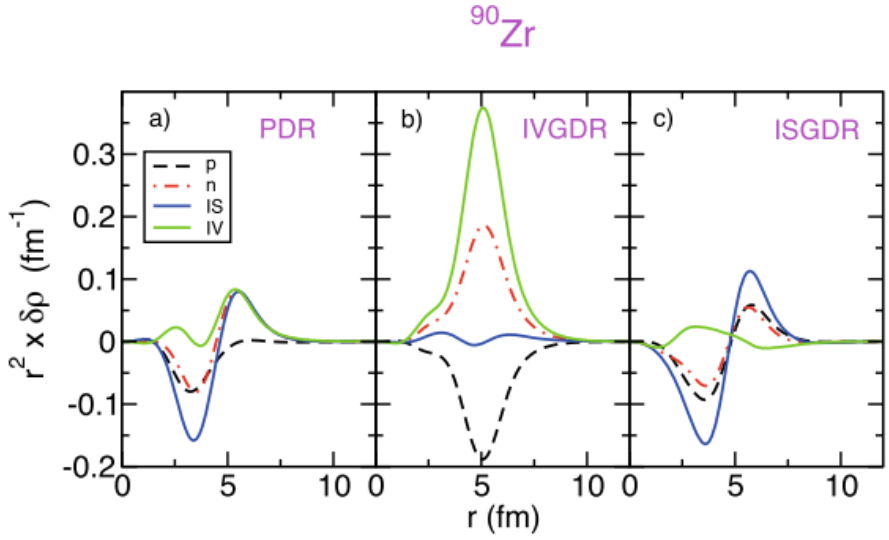

Figure 2.6: *Transition densities for the low-lying dipole state (PDR) (a), for the IVGDR (b) and for the ISGDR (c) for the ^{90}Zr isotope. The proton, neutron, isoscalar and isovector components are shown as indicated in the legend. Taken from Ref. [Bra15].*

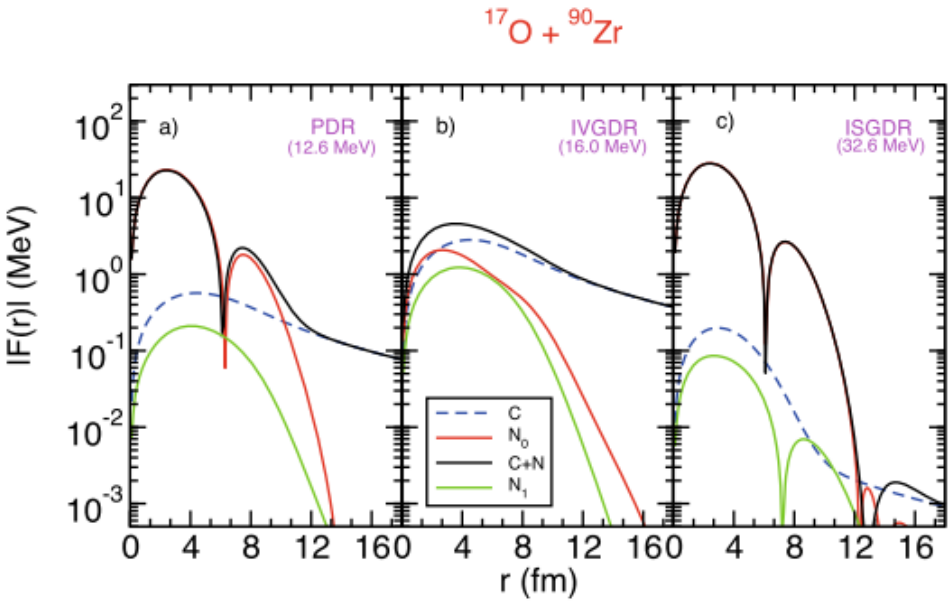

Figure 2.7: *Form factors for the system ^{17}O + ^{90}Zr for the PDR state (panel (a)), the isovector GDR (panel (b)) and for the ISGDR (panel (c)). In each frame there are reported the nuclear and Coulomb (blue dashed line) contributions, as well as the total one (black solid line). For the nuclear part there are the two contributions: isoscalar (red solid line) and isovector (green solid line); in the legend they are indicated as N0 and N1, respectively. Taken from Ref [Bra15].*

As it was discussed in sec. 1.3.2, the transition densities of the IVGDR and PDR are rather different. This is also reflected in very different character of the calculated form factors. An important difference is especially observed on the surface of the nucleus. This is the reason why this is very interesting to study excitation of the nuclear surface in order to examine the surface part of the transition densities. One can also observe, that there is much higher nuclear contribution with respect to Coulomb contribution in excitation of PDR states. These observations justify that the experiments with isoscalar probes interacting mainly on the surface of the nucleus would give important information of underlying structure of PDR states.

As it was mentioned in sec. 1.3.2, the proton and neutron transition densities for the PDR state at 8.39 MeV in ^{140}Ce were calculated using RQRPA [Paa09] and are shown in left panel of Fig. 2.8. The corresponding form factor calculated using the double-folding procedure is shown in the right panel of Fig. 2.8. Similarly to the previously discussed ^{90}Zr case, the form factor is dominated by the nuclear excitation. The shape of the form factor stresses the importance of the surface contribution. This form factor, scaled for a given excitation energy and corresponding percentage of ISEWSR, will be applied to the DWBA calculations of the PDR states. The procedure will be further discussed in sec. 5.4.4.

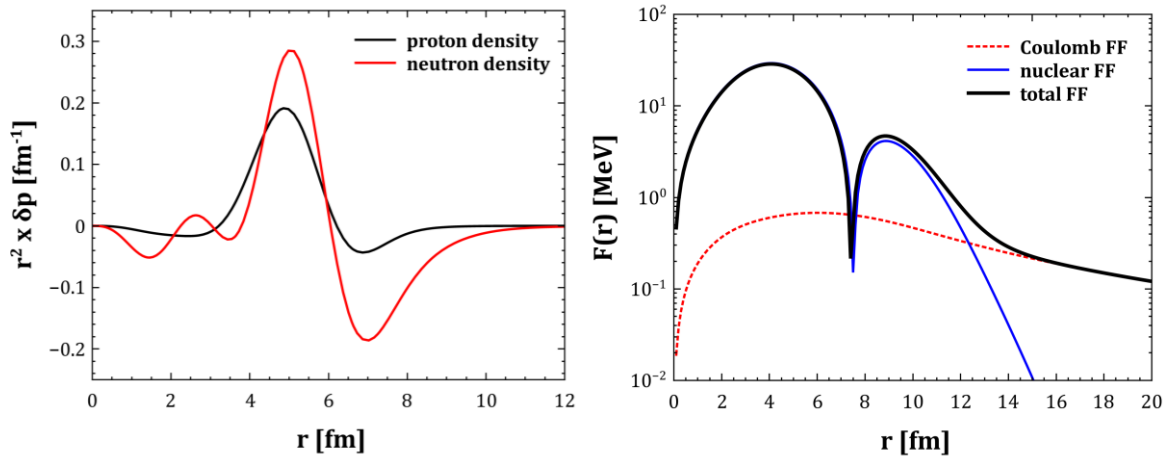

Figure 2.8: *Left panel: Neutron and proton transition densities for the pygmy dipole state at 8.39 MeV in ^{140}Ce calculated with the RQRPA (top panel) [Paa09].; Right panel: Form factor obtained with the double folding procedure for the PDR state in ^{140}Ce [Krz16b].*

Chapter 3. EXPERIMENTAL TECHNIQUE

The experiment, which is a subject of this thesis, was done in 2011 as a last one of AGATA Campaign in Legnaro National Laboratories (LNL), Italy. The high-lying collective states in ^{140}Ce were excited *via* inelastic scattering of ^{17}O beam at the energy of 20 MeV/u (in laboratory frame) and followed by subsequent γ-rays emission. The ^{140}Ce target placed inside the scattering chamber of 2.5 g/cm^2 thickness was enriched to 99%. The picture of experimental setup designed for the study is presented in Fig. 3.1 and its scheme is shown in Fig. 3.3.

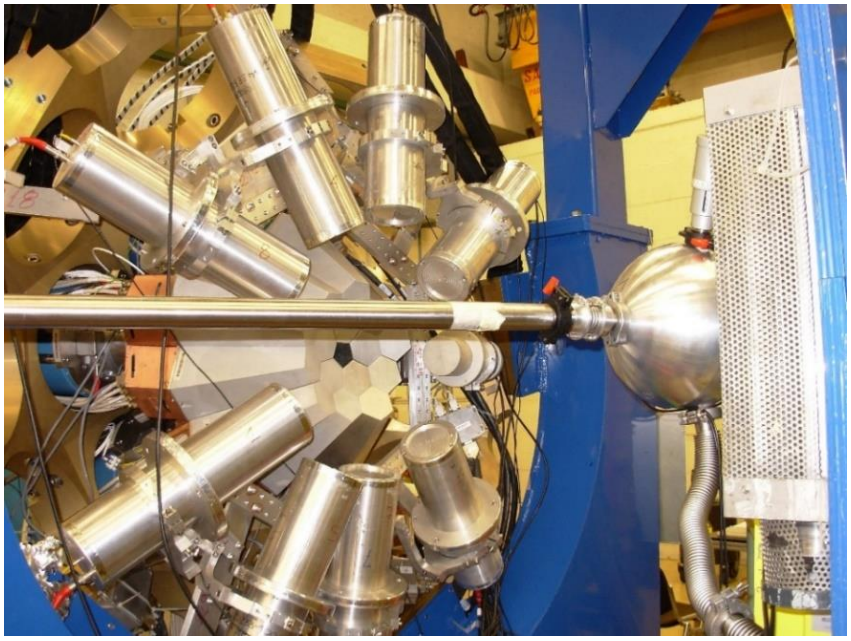

Figure 3.1: *Picture showing the experimental setup. The beam pipe is connected with the target chamber which is surrounded be the AGATA and HECTOR+ arrays. The TRACE array is mounted inside the target chamber.*

Inelastic scattering of heavy ions can be successfully used to study the highly-excited states e.g. giant resonances [Bor98, Har01]. One of the major problems needed to be considered is that the differential cross section for inelastic excitation as a function of scattering angle does not illustrate well the spin of excited states. Therefore it is advisable to measure the scattered heavy ions in coincidence with the de-excitation γ-rays in order to obtain a clear identification of the spin of excited states. Another difficulty of using heavy-ion scattering can come with the excitation of the projectile, which may become a major source of background in the energy region of interest in particular study. Such case is illustrated in the right panel of Fig. 3.2, where the excitation spectrum of ^{208}Pb target bombarded with the ^{16}O is presented. The region marked in blue corresponds to the energy range dominated by the projectile excitations. This problem can

be overcome when using the projectile with a small neutron separation energy (S_n), such as ^{17}O (S_n=4.1 MeV). Then, if the excitation energy higher than S_n is transferred to the projectile, the neutron emission dominates and the event is removed from the inelastic scattering channel. This is presented in the left panel of Fig. 3.2, which shows the similar excitation spectrum of ^{208}Pb target but bombarded with ^{17}O. Clearly, the background coming from the projectile excitation is greatly reduced.

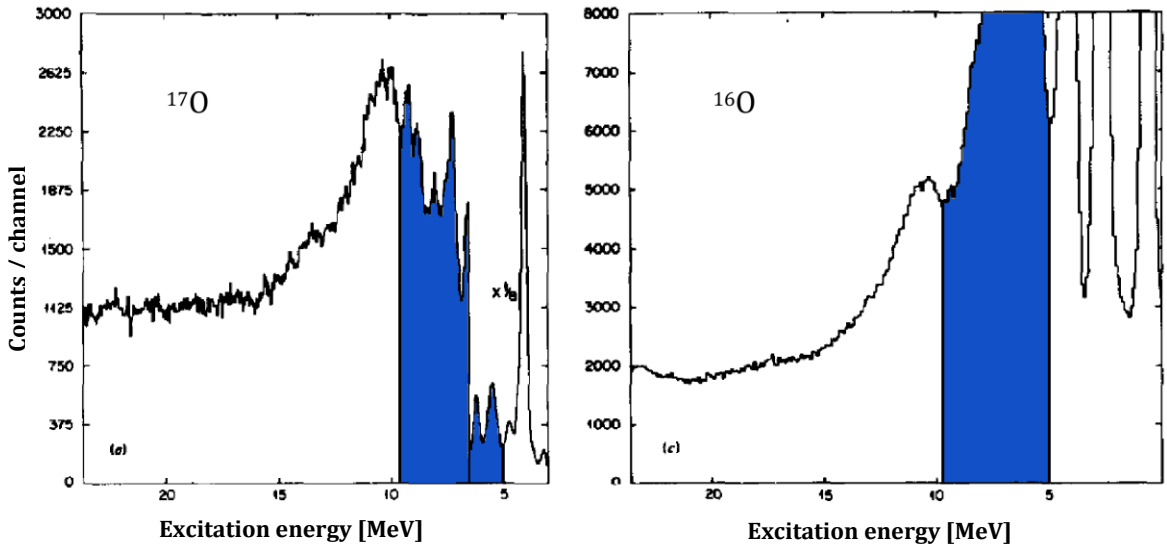

Figure 3.2: *Excitation spectra of ^{208}Pb target bombarded with a ^{17}O (left panel) and a ^{16}O (right panel) beam; the background in the blue area of the ^{16}O spectrum is caused by projectile excitation and is completely removed with the ^{17}O beam. Adapted from [Bert88].*

The ^{17}O beam at the energy of 340 MeV and average current of 0.5 pnA was produced with the PIAVE-ALPI accelerator system [Pug10]. PIAVE is a superconducting radiofrequency quadrupole, and was used as an injector for the superconducting linear accelerator ALPI. The maximum current was limited by the counting rate on AGATA detector.

The scattered ^{17}O ions were detected by the two ΔE-E silicon telescopes, mounted inside the scattering chamber and placed on the left and right side with respect to the beam axis, which were prototypes of the TRACE (TRacking Array for Light Charged particle Ejectile) project [Men14].

The γ rays were detected by the two independent systems. One of them was AGATA (Advanced GAmma Tracking Array) [Akk12, Gad11], which consisted of five triple clusters of high-purity germanium (HPGe) detectors. The array takes profit from the powerful algorithms of γ-rays tracking and pulse shape analysis (PSA) which will be presented in sec. 3.2. The second one

contained nine large volume $LaBr_3$:Ce scintillators of HECTOR+ array [Gia13], which aim was to increase the detection efficiency in the high energy region.

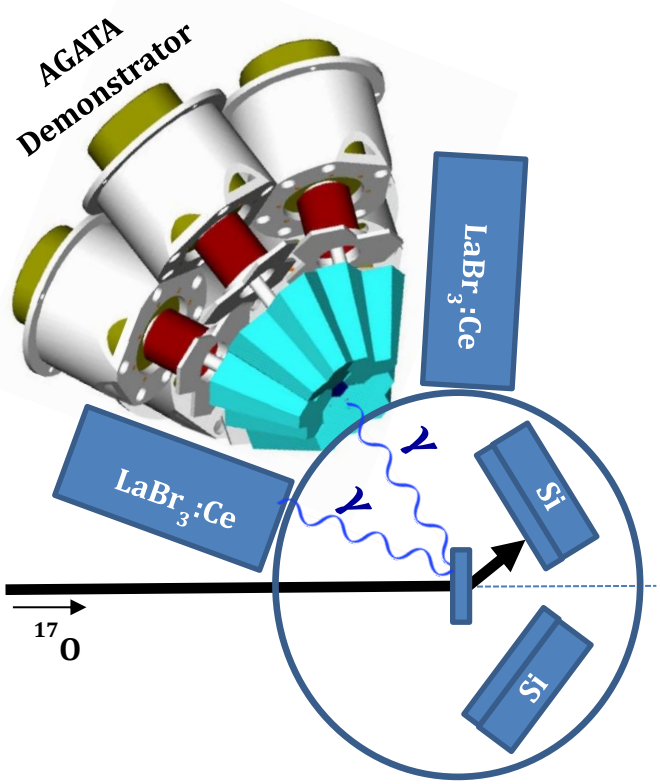

Figure 3.3: *Scheme of the experimental setup.*

3.1. THE SILICON TELESCOPE DETECTORS

The detectors used for this experiment are the prototypes for the TRacking Array for light Charged particle Ejectiles (TRACE) [Men14], a 4π array of segmented ΔE-E silicon telescopes. The TRACE was designed for the detection of light charged particles produced in fusion-evaporation reactions as well as the direct reactions with high efficiency, high counting rate and high energy resolution. Its high granularity and modularity allows for application in many different purposes, among them for identification of heavier ions up to oxygen.

Each ΔE-E silicon telescope consists of the two separate detectors (schematically shown in the right panel of Fig. 3.4):

- *ΔE*, of 200 μm thickness which corresponds to the energy loss of around 70 MeV for the ^{17}O beam @340 MeV;
- *E*, of 1mm thickness, which is enough to stop the beam completely.

The detectors are made of 60 pixels, 4x4 mm^2 each which gives total area of 20 x 48 mm^2. This results for each pad in a much better energy resolution compared to a non-segmented Si detector of the same total area: the electrical noise of a solid-state detector is proportional to its capacity,

which is in turn proportional to the detector surface area for a planar geometry. The left panel of Fig. 3.4 shows the picture of one Si detector and the scheme of Si telescope and identification of the ions is shown in the right panel.

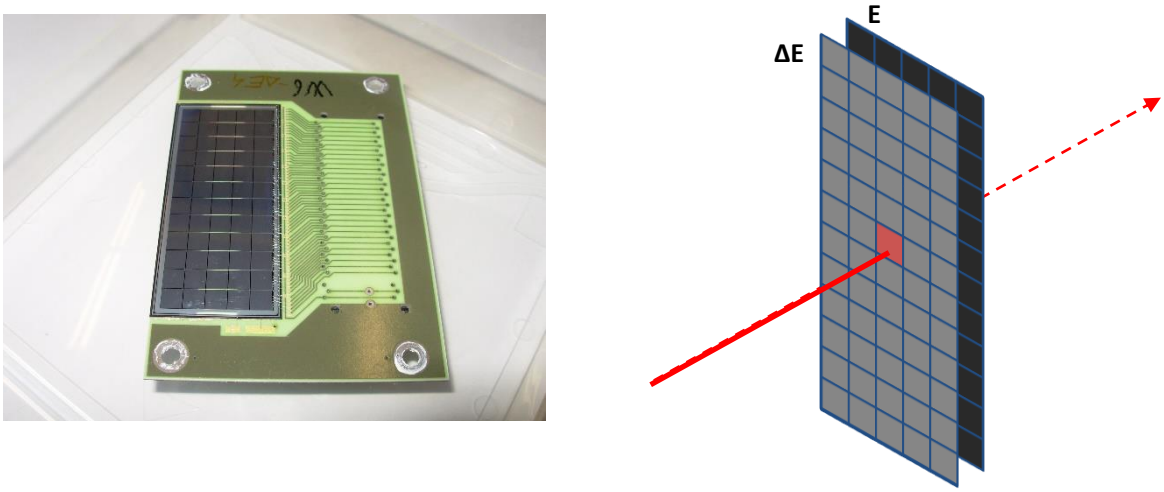

Figure 3.4: *Left panel: Picture of one Si detector; Right panel: The scheme illustrating track of the ion detected in one pad (marked in red) of ΔE-E silicon telescope.*

In the experiment, two ΔE-E telescopes were mounted inside the scattering chamber at ~7 cm from the target on the left and right side with respect to the beam axis, covering a solid angle of ~100 msr per telescope and an angular range of ~25°. The picture of the scattering chamber with the telescopes inside is shown in Fig. 3.5. Each detector has 61 output channels (one for each pad and one from the non-segmented back side). This would require a large number of 244 channels of front-end electronics to cover all 4 detectors. However, for the purpose of this experiment, such angular range was not required, therefore it was possible to use the adapter that selects the 32 pads closest to the beam direction (see Fig. 4.9). This allowed to reduce the number of needed electronics by a factor of 2, without losing physical data. Then, each detector was connected to a custom 32-channels charge preamplifier. The preamplifiers were mounted as close to the detectors as possible and placed on a metallic board to allow heat dispersion. The preamplifiers worked under vacuum, and were connected through high-density cables to a flange and then to an active circuit splitting the signals of each into 2 standard flat cables that were the input of a CAEN N1568 16-channel spectroscopic amplifier, set with a shaping time of 2 μs. The output of the amplifiers was then sent to the CAEN V879 ADCs (Analogue to Digital Converters) for data acquisition. Each amplifier channel also had a built-in CFD (Constant Fraction Discriminator), which was sent to the CAEN V878 TDCs (Time to Digital Converters). Finally, the amplifiers also have an "OR" output that is the logical "OR" of all the 16 CFD channels, and is used to build the trigger condition (see sec. 3.5).

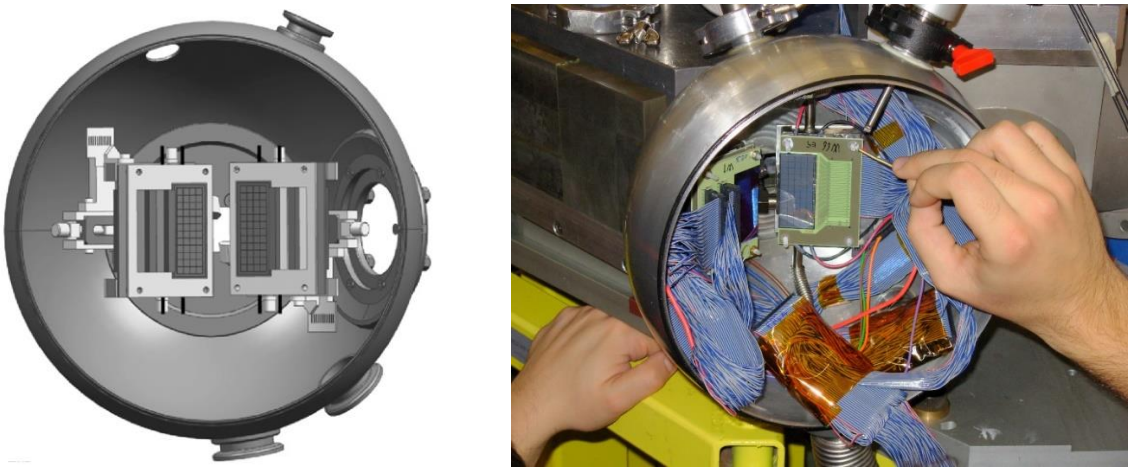

Figure 3.5: *Scheme (left panel) and picture (right panel) of the ΔE-E silicon telescopes of TRACE array placed inside the scattering chamber.*

Each of the telescopes was cooled into temperature of about -20 °C by two Peltier cells placed behind. Good heat transfer was guaranteed thanks to mounting the detectors in aluminium oxide PCBs (Printed Circuit Boards) and brass dices were used to fix the ΔE detector to the E detector. The hot side of the Peltier cells was in turn cooled by a refrigerant liquid kept at ∼10 °C by a chiller system.

3.2. THE AGATA ARRAY

The Advanced GAmma Tracking Array (AGATA) is the European project aiming to develop and operate the next generation 4π γ-ray spectrometer [Akk12]. The array is based on the technique of γ-ray tracking in electrically segmented high-purity germanium (HPGe) crystals. This requires the precise information on the energy, time and position of each interaction of γ-ray within the volume of detector. They are determined with the pulse shape analysis (PSA). With this new approach the traditional Compton-suppression shields become unnecessary resulting in large gain of efficiency and energy resolution.

One of the aims of the collaboration was the mobility of the array, taking profit from the beams and instrumentation of different laboratories. It started operation in LNL, Legnaro as a Demonstrator phase, utilising the wide range of stable beams. Afterwards, it operated in GSI, Germany and now in GANIL, France and later at the new radioactive beams facilities such as FAIR, SPIRAL2, SPES and HIE-ISOLDE. The constant expansion of the spectrometer geometry should result in full 4π system consisting of 180 crystals in total.

This section will briefly describe the detectors construction and dedicated digital electronics with the focus on coupling to ancillary detectors that were applied in the experiment. Then, the algorithms of PSA and tracking will be presented and some of the properties of the array such as the detection efficiency and energy resolution. Finally, the Demonstrator phase of AGATA at LNL will be presented.

3.2.1. Design

The possible configurations of the array were investigated using the GEANT4 code based on the Monte Carlo simulations. In order to maximize the detection efficiency and to minimize the development and maintained cost, the full configuration was decided to consist of 180 hexagons of 3 slightly different shapes. This is presented in Fig. 3.6 with different colours (red, blue, green). To minimise the passive parts of array, composite detectors are grouped in clusters with the same cryostat.

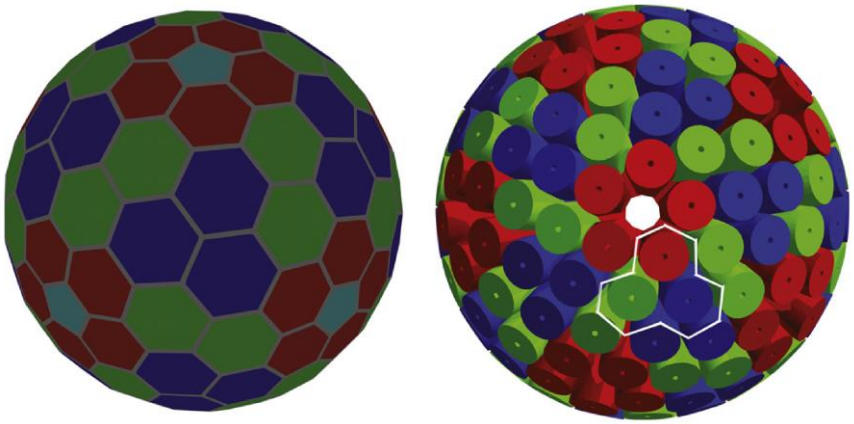

Figure 3.6: *Computer aided design images of the 180 crystal configuration of AGATA. One triple cluster is marked. Taken from Ref. [Akk12].*

3.2.2. Detectors

The heart of each AGATA detector is an encapsulated and electrically segmented closed-end coaxial n-type germanium (HPGe) crystal. In order to fit the final 4π array configuration, there are three different shapes of crystals, arranged in triplets with identical triple cryostat.

Each single HPGe crystal is subdivided into 6 rings and each of them is also subdivided into six sectors (see Fig. 3.7). The total energy deposited in each crystal is collected to the central contact (core) which gives a total number of 37 signals per crystal.

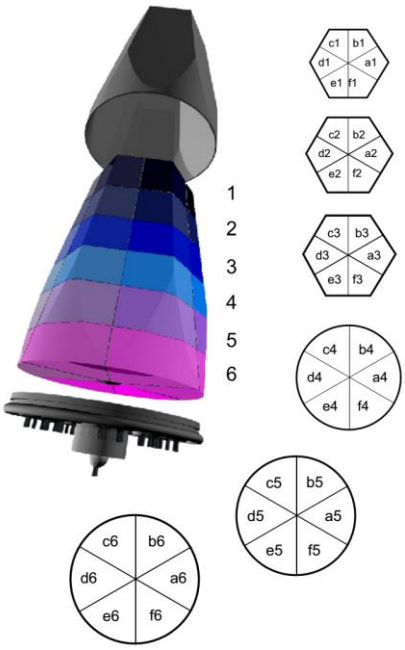

Figure 3.7: *Scheme of segment labelling of the AGATA HPGe crystal. Taken from Ref. [Akk12].*

3.2.3. Front-end Digital Electronics and Coupling to Ancillary Detectors

The purpose of the front-end electronics (FEE) is to digitise the signals from each segment, mark the time of detection with a timestamp, extract the amount of γ-ray energy deposited during each interaction and determine the total energy from the core signal. The design of the AGATA FEE needs to handle the high counting rates that are specified for the system [Akk12].

The AGATA electronics consists of the following components for each crystal:

- One digitiser comprising six segment cards, one core card, two power-supply cards and two control cards;
- Two pre-processing carrier cards in the ATCA (Advanced Telecommunication Computing Architecture) card format, each containing four Common Mezzanine Cards (CMC) with PCI Express readout to the PSA farm. Seven CMC mezzanines correspond to the sig segment and one core card in the digitiser and one contains the interface to the global trigger and clock system.

The elements of FEE are connected with optical fibres which ensures appropriate data-transmission rates and also a good electrical isolation.

One of the very important issues is to couple the AGATA array with complementary detectors, like HECTOR+ and TRACE in the case of this experiment. However, these systems are based on conventional analogue readout electronics, thus special interface to the GTS system has been developed at IFJ PAN [Cze05]. The interface is called AGAVA (AGATA VME Adapter) [Baz05]. The AGAVA interface is developed in the VME standard with full compatibility with VXI readout mode.

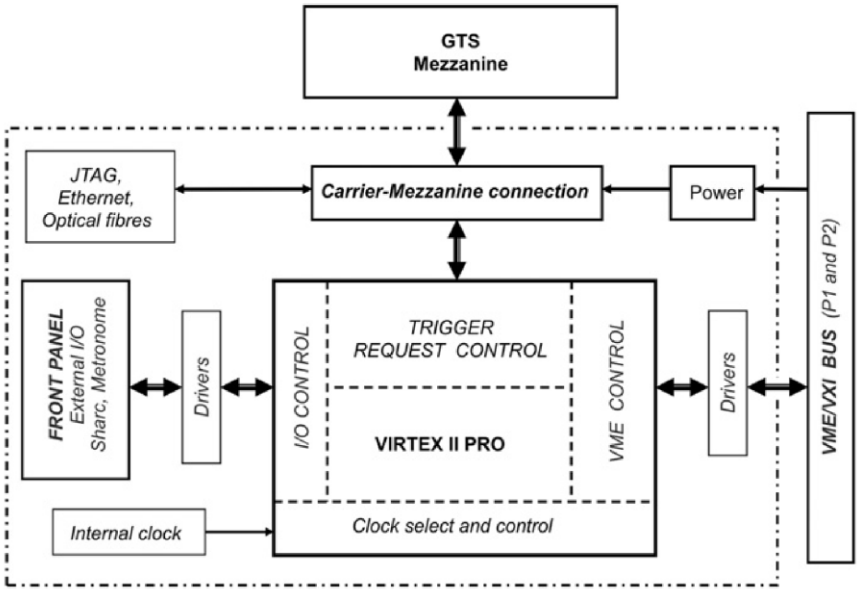

Figure 3.8: *Block diagram of the AGAVA interface. Taken from Ref. [Akk12].*

The AGAVA interface is the carrier board for the GTS mezzanine card used in AGATA for the global trigger and timestamp distribution. Its main task is to merge the AGATA timestamp with conventional readout based on VME or VXI. As seen on the block diagram of the interface presented in Fig. 3.8, AGAVA has necessary connectors to interface with VME Metronome and Shark [Laz01]. The logic process is controlled by an FPGA (Field Programmable Gate Array) of the Virtex II Pro type. The AGAVA module includes all necessary connections to the trigger cycle and for a total readout system [Laz01]. It is also directly linked to the GTS mezzanine card by passive Ethernet interface.

3.2.4. Pulse Shape Analysis (PSA)

The main aim of the pulse-shape analysis (PSA) is to identify the individual interaction point and the energy of the γ-ray within the crystal. Typically, a γ-ray may interact several times within a segment and/or can be scattered to another segment/crystal. This determines that the precision of position identification must be better than 5 mm (FWHM). As it is not relevant to obtain such precision by physical segmentation the HPGe detector electrode, it is possible to extract this information by analysing the shape of the detector signal.

Pulse shape analysis techniques are based on the comparison between digitized pulses with a basis of reference signals, each of them corresponding to a well-localised single interaction point. The input data for the PSA process consists of 37 signals $S_j(E,t)$ with $j = 0, 1, \ldots, 36$ as an output from the HPGe detector preamplifiers (36 segments + core). Since the detector response is linear, the input data can be written as the superposition of the signals associated to the single hits of the gamma weighted by their energy release:

$$S_j(E,t) = \sum_{i=1}^{N} E_i S_j(x_i, y_i, z_i, t) \tag{3.1}$$

where N is the number of interactions inside the segment and $E = \sum_{i=1}^{N} E_i$.

In the case when N=1, Eq. 3.1 reduces to:

$$S_j(E,t) = E S_j(x_i, y_i, z_i, t) \tag{3.2}$$

In order to solve this equation, one has to find the interaction point that best reproduces the measured signal shape. This is done by comparing the measured signal shape with so called a signal basis, which is a set of shapes corresponding to known interaction points. Good position resolution can be achieved if not only the net-charge signal of a segment is compared with the basis, but also the transient shapes in neighbouring segments are also compared to a basis for transient signals. If *N>1*, there is the added complication of disentangling the single interactions of each segment, all with an unknown energy deposit and unknown position.

It is a very demanding task to compare the waveforms, especially when decomposition of each signal shape in multiple interaction points is needed, because it requires a large quantity of memory and of CPU time. Therefore, fast and efficient PSA algorithms are needed. There are several approaches of PSA:

- adaptive grid search [Rec09],
- neural networks, matrix inversion [Ola06],
- genetic algorithms [Krö06],
- recursive subtraction [Cre07],

In the experimental campaign in LNL, it has been decided to use a grid search algorithm because it is the only one method with processing times small enough to be used in real-time applications. The algorithm bases on the assumption that the size of a segment is small enough that multiple interactions inside the same segments can be ignored. Therefore, the PSA is performed under the simpler case of Eq. 3.1 (N = 1). Even though, it is not a realistic approximation, its effect on the overall performance of the detector has been found negligible [Rec06].

Another important factor that influences the quality of the PSA are the signal basis that are used for the decomposition for the measured shapes and it is independent from chosen algorithm. The most accurate would be to build an experimental signal basis, but although a large effort in this matter [Bos07, Vet00, Koj07], it is not available yet due to the long times needed to build up the necessary statistics while achieving a good precision on the reference positions. At the moment, the basis obtained *via* detailed calculations of the charge transport through the detector are used [Krö01].

As a result of PSA, the interaction points with the corresponding energy and time are determined and the events need to be reconstructed according to their timestamp. It is achieved with the

tracking algorithm (see sec. 3.2.5), which allows to match the coincident interaction points and to determine the total energy and the emission direction of the γ-rays that have been fully absorbed in the germanium array. At this stage, the absolute position of individual crystals and target position corrections are included.

3.2.5. Gamma-ray Tracking

The purpose of tracking algorithms is to reconstruct the path of the γ-ray inside the detector determining its energy and direction. This is done by establishing a proper sequence of the interaction points in the detector. There are two groups of algorithms: clusterization or forward tracking [Sch99] and back tracking [Mar99].

Forward tracking. The first step of these algorithms is to identify the clusters of interaction points that may belong to single γ-ray. Clusters are identified as a set of interaction points with an angular distance $\leq \theta_0$ between each other (link algorithm) or with respect to given point (leader algorithm), by looking at the forward peaking of Compton scattering cross-section. During second step, the following criteria are applied in order to evaluate whether the cluster contains all the interaction points belonging to a single γ-ray:

1. *If the interaction points satisfy the Compton scattering formula*, the tracking algorithm uses the angle-energy relation of Compton scattering to determine the most likely scattering sequence from the position and energy of the interaction points:

$$\chi^2 = \sum_{j=i}^{N-1} W_j \left(\frac{E_{\gamma\prime} - E_{\gamma\prime}^{pos}}{E_\gamma}\right)_j^2 \tag{3.3}$$

   where E_γ is the sum of the deposits from j to N-1, and $E_{\gamma\prime}^{pos}$ is the energy of the scattered photons according to the Compton scattering formula.

   For a cluster of *N* interaction points, the *N!* permutations are tested, and the cluster is defined as "good" if the χ^2 is below a predetermined threshold.

2. *If the cluster is composed by a single interaction point and the energy satisfy photoelectric conditions*, the algorithm evaluates the compatibility between γ-ray energy and interaction depth in the detector. If the compatibility is reached, a Monte Carlo-like approach is taken to decide whether to consider the interaction point as an actual photo electric event or if to discard it as an isolated Compton scattering event.
3. *If the interaction point corresponds to a pair production event,* there are two γ–rays of energy equal to 511 keV and an interaction point in the middle with energy greater than 1022 keV. Then, the three energies are summed and considered as a single γ–ray.

Finally, some of the clusters are wrongly identified so that the algorithm tries to recover it. For example, it is likely to misidentify cluster because of a single γ ray being separated into two

clusters. Such γ–ray can be correctly identified by tracking together all pairs of bad clusters. When the result gives a small χ^2, the γ ray is recovered by adding the two clusters. The clusters, which do not satisfy any of the above criteria, are rejected improving the P/T (peak to total) ratio of the spectra without the need for Compton suppression shields. If a large solid angle is covered with segmented germanium detectors, the combination of PSA and γ–ray tracking allows for a very high photopeak efficiency together with a good P/T ratio. Example of tracking performance for a high multiplicity event is shown in Fig. 3.9. The coloured dots represent single interaction points of γ-rays inside a 4π detector shell. The red circles correspond to clusters of interaction points identified by the tracking as belonging to a single γ ray, while the green squares correspond to clusters that are discarded. The forward tracking algorithm is the basis for the Mars Gamma-ray Tracking (MGT) code [Baz04] that was used both for the experimental data and the GEANT4 simulations.

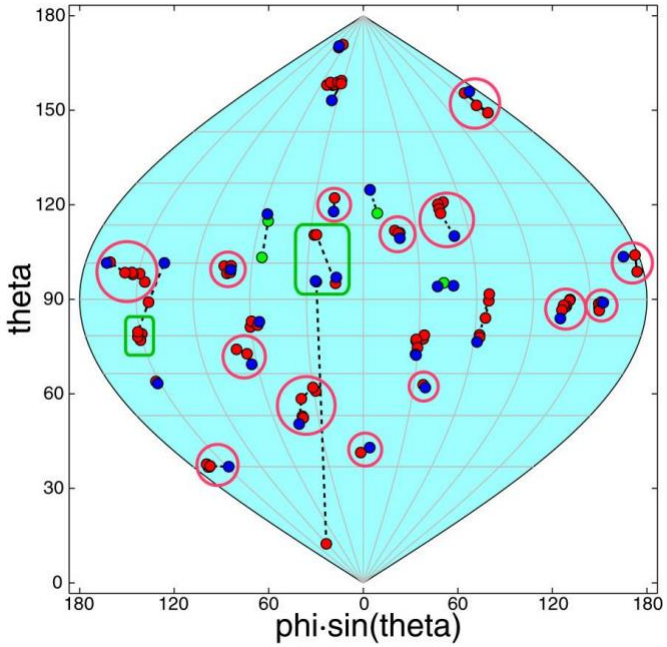

Figure 3.9: *Simulated interaction points of 30* γ-rays *of E_γ = 1 MeV detected in an ideal 4π HPGe shell and reconstructed with the tracking algorithm. Correctly reconstructed transitions are grouped with red circles while green rectangles represent badly reconstructed background events. Taken from Ref. [Baz91].*

Backtracking. The second algorithm takes advantage from the fact that the photoelectric energy deposition is almost independent from the incident energy and is peaked around 100-250 keV. Firstly, it is assumed that the interaction points of a given deposited energy from the interval $e_{min} \leq e_i \leq e_{max}$ are the last interaction (in time) of a fully absorbed γ-ray. Then the algorithm finds the closest interaction to the photoelectric one and computes the scattering angle based on the incident and scattered energies. Finally, along this direction, the algorithm searches for the other previous interactions and it is iterated until the direction points directly to the target. This

method showed a worse P/T ration and was found to be less efficient [Lop04] thus was not used in the analysis of this experiment.

3.2.6. Efficiency and Energy Resolution

One of the most important property of the detector is the energy resolution, which is the ability to accurately determine the energy of the γ –ray. Another important property of an array is the detection efficiency, which refers to the total photopeak absorption probability over the 4π solid angle. Both of them will be discussed in this section.

Energy resolution

The energy resolution of the AGATA HPGe detectors was evaluated by measuring the γ –rays in the range from 2 – 9 MeV emitted by the Am-Be-Fe source (see Fig. 3.10) [Cre13]. Core of the source is made of ^{9}Be and alpha-unstable ^{241}Am which is placed in 7 x 7 x 20 cm iron slab with a drilled hole of 3 x 3 cm, and surrounded by a paraffin wax of a 20 x 20 cm cylindrical shape. The alpha particles emitted by the ^{241}Am are likely to be captured by ^{9}Be resulting in creation of ^{12}C via ^{9}Be(α, n)^{12}C reaction. The emitted neutrons of the energies between 400 keV and 5 MeV are thermalized in the paraffin, which works as a moderator and shielding. The neutrons are then captured by the iron isotopes. The reaction populates also the ^{12}Ce in its first excited state at 4.4 MeV. Velocity of the ^{12}C is 10% speed of light thus the gamma decay from this level is broaden due to Doppler effect. The reaction ^{54}Fe(n, γ)^{55}Fe reaction produces γ rays up to 9 MeV.

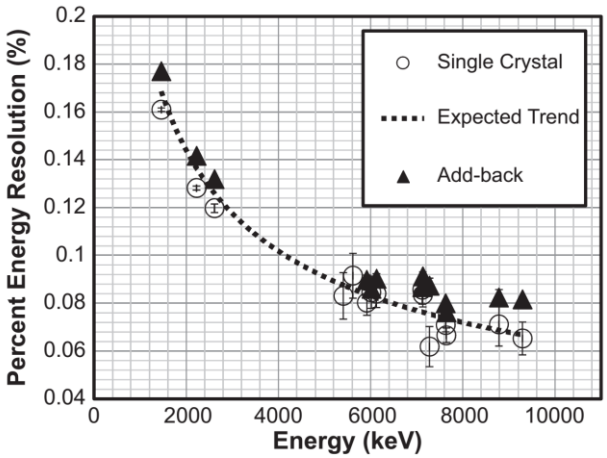

Figure 3.10: *Relative energy resolution of the AGATA detectors estimated for the Am–Be–Fe source data. The data for the best performing single detector are shown by empty black circles. The black triangles represent the data for the add-back procedure, performed among all crystals that responded in each event. The expected $E^{-1/2}$ trend is indicated by the dashed black line. Taken from Ref. [Cre13].*

Efficiency

The detection efficiency depends on the energy of the detected γ–ray. The relative detection efficiency of the AGATA array can be obtained using simulated and in-beam data. For the experiment, which is the subject of this thesis, the crucial point is the detection of the high-energy γ–rays, thus it was necessary to evaluate the efficiency of tracking algorithm and the add-back procedure of the AGATA Demonstrator [Cre13, Avi11].

This was studied using the Am-Be-Fe source for the 2 – 9 MeV energy γ–rays as well as the 15.1 MeV produced using the $d(^{11}B,n\gamma)^{12}C$ at E_{beam} = 19.1 MeV and showed that the add-back procedure is more efficient at high-energies (see Fig. 3.11) [Avi11]. This is due to the fact that the 15.1 MeV γ-ray has multiplicity 1, background level is low and the tracking algorithm was optimized in the energy range between 0 – 4 MeV where Compton scattering is dominant while at the 15 MeV, the main interaction mechanism is the pair production [Cre13]. Since this experiment aimed to study the high-energy γ–rays, with multiplicity 1 and relatively low background level, the add-back procedure was a good alternative to standard tracking algorithm. The add-back efficiency curve extracted from simulated data is shown in Fig. 3.12 [Far10].

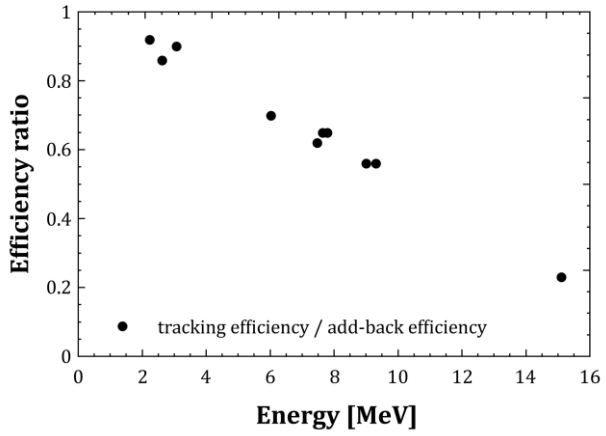

Figure 3.11: *Ratio between the tracking and add-back detection efficiency as a function of γ-rays energy for experimental data. Adopted from Ref. [Avi11]*

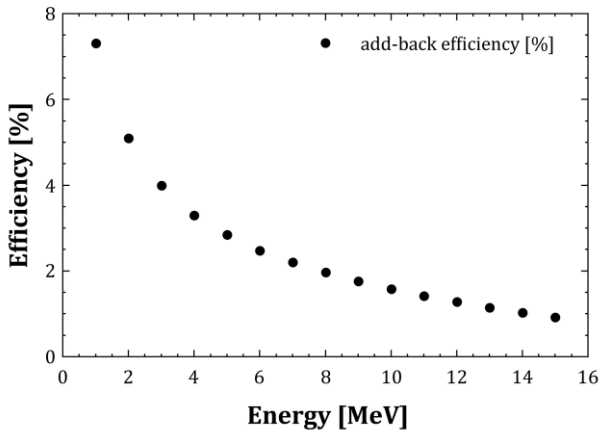

Figure 3.12: *Absolute efficiency of 5 triple cluster of AGATA obtained from simulated spectra using the add-back procedure, adopted from Ref. [Far10].*

3.2.7. AGATA-Demonstrator at LNL

The Demonstrator phase of AGATA project aimed to operate 5 triple clusters of HPGe detectors. It was installed in LNL in 2008 together with its digital electronics, DAQ and full on-line processing of the digitized data and operated between 2009 and 2011. This experimental campaign was aimed to demonstrate the effectiveness of the γ-tracking method in real physical measurements. The Fig. 3.13 the AGATA-Demonstrator phase in LNL, consisting of five triple clusters of HPGe detectors.

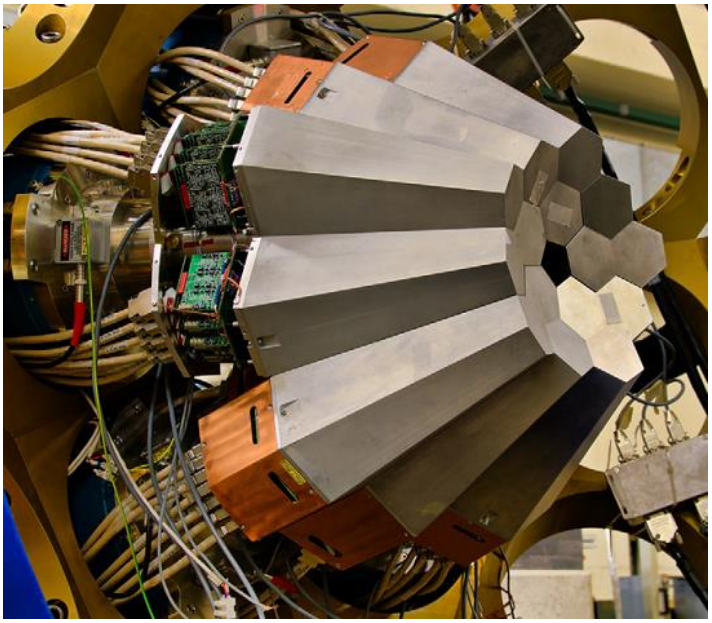

Figure 3.13: *Photo of five triple clusters of AGATA-Demonstrator in LNL [Akk12]*

3.3. THE HECTOR+ ARRAY

In this experiment, one cylindrical 3" x 3" and 8 cylindrical 3.5" x 8" $LaBr_3$:Ce detectors of HECTOR+ array [Gia13] were placed around the AGATA-Demonstrator. First $LaBr_3$:Ce detectors were produced in 2001. This type of scintillator has not only high efficiency and good time resolution but also the best energy resolution of all scintillators.

The signal from each crystal was sent to be processed by a channel of a LaBrPro module [Boi08]. This is a custom spectroscopy amplifier developed by group from University of Milan, in order to shape the $LaBr_3$:Ce signals. It consists of 16 channels giving the fast and slow outputs for each of them, which corresponds to a fast and slow components of the signal, as well as a time output obtained by a Constant Fraction Discriminator (CFD).

The properties of the $LaBr_3$:Ce scintillator will be briefly discussed in following section.

3.3.1. Efficiency and Energy Resolution

As indicated previously for the germanium array, the efficiency and energy resolution are the important properties for the γ-rays detection. Most significant data will be given following the series of test measurements for 3.5" x 8" volume $LaBr_3$:Ce detectors, fully described in Ref. [Gia13].

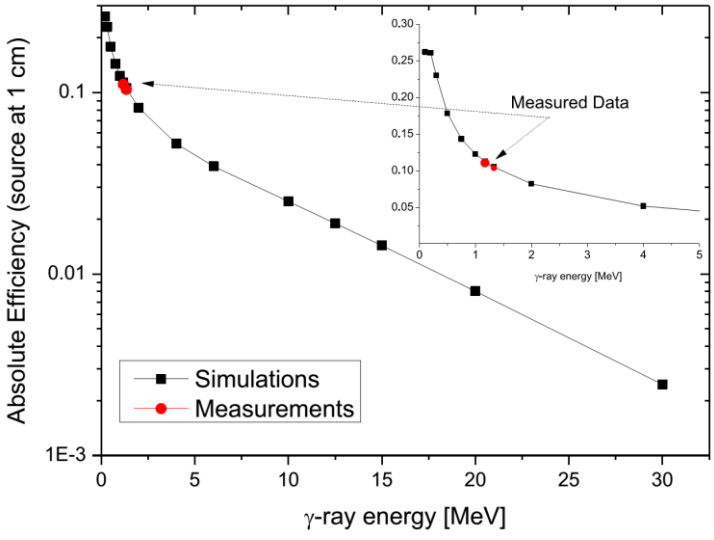

Figure 3.14: *Absolute full energy peak efficiency for a large volume 3.5″ 8″ LaBr3:Ce detector measured with a ^{60}Co source positioned 10 mm away from the detector surface together with simulated values. The inset plot shows the results up to 5 MeV energy range. Taken from Ref. [Gia13].*

Efficiency

In order to estimate the absolute γ –ray detection full energy peak efficiency, the "sum peak" technique was applied using the ^{60}Co source placed at the distance of 10 mm. The idea of the technique is to compare the energy spectrum counts in the two full energy peaks at 1173 and 1332 keV emitted from the ^{60}Co source with the counts in the sum peak at 2505 keV. Necessary assumption is that the two detector efficiencies at 1173 and 1332 keV are almost equal which is true for large volume detectors. The experimental efficiency and Geant3 simulations are compared in Fig. 3.14 and showing very good agreement.

Energy resolution

Energy resolution of 3.5" x 8" volume $LaBr_3$:Ce detectors was studied in ATOMKI Laboratories, Debrecen (Hungary) in wide energy range of γ–rays between 1 – 22.6 MeV. It was possible using different radioactive sources: ^{60}Co, ^{133}Ba, ^{137}Cs, ^{152}Eu, ^{88}Y and an Am-Be-Ni, as well as accelerator-driven nuclear reactions (p,γ).

Fig. 3.15 shows the FWHM energy resolution of the $LaBr_3$:Ce detector as a function of γ–ray energy using analogue electronics. It is clear that estimated values differ from strictly statistical behaviour, i.e. $E^{1/2}$ asymptotic curve (dashed line); for the high-energy γ–rays there is a saturation of energy resolution at constant value of 0.5 – 1%. It is possible to interpret the experimental data (red line) by taking into account three components as in the following equation [Gia13]:

$$ER_{FWHM} = \sqrt{a + bE + cE^2} \tag{3.4}$$

First term (a), is associated to the electronic noise which is unrelated to the energy and the second term (b) is related to the statistical generation noise. The last term (c) modulates the all gain drift effects.

Good energy resolution and high efficiency of the 3.5" x 8" volume $LaBr_3$:Ce scintillators for the detection of high-energy γ –rays (> 5 MeV) makes the HECTOR+ array a complementary tool coupled to AGATA-Demonstrator to study the high-energy states i.e. pygmy and giant resonances.

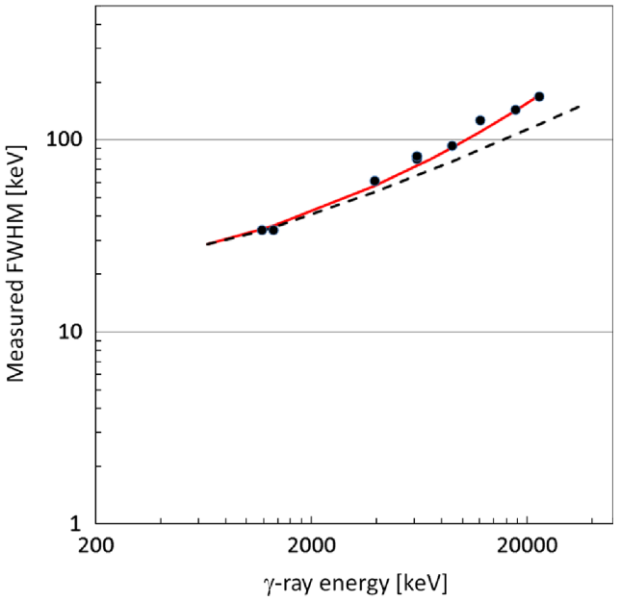

Figure 3.15: *The energy resolution (FWHM) of one $LaBr_3$:Ce detector in the range between 1 and 22.6 MeV. The dashed line corresponds to the energy estimation based only on statistical and electronic noise contribution. Red line represents the function of Eq. 3.4, which takes into account the saturation effects at the high γ–rays energy. Taken from Ref. [Gia13].*

3.4. DATA ACQUISITION SYSTEM (DAQ)

The electrical contacts of each AGATA detector are segmented 36-fold, as mentioned in sec. 3.2.2, and the digitizers sample the pulses from each segment at 14 bit precision with a frequency of 100 MHz. Thus, a pulse trace of 60 samples is extracted and acquired for each accepted event. A counting rate of 50 kHz per crystal results in the dataflow at the level of 100 MB/s for each detector (with zero suppression). The online analysis during experiment requires the PSA to be performed in real time for each acquired traces and followed by tracking algorithms in order to reconstruct the detected γ-rays. This requires from the Data Acquisition System (DAQ) to be able to:

- handle large quantities of data,
- control a computing farm for the PSA and tracking algorithms,
- coordinate the flow of information between the digitizers, the computing farm, and the disk server where all the data are written.

In this experiment, the NARVAL-based DAQ [Gra05] software was applied to handle the tasks required for AGATA and independent DAQ based on KMAX environment [Kmax] was used to control the ancillary detectors (TRACE and HECTOR+). The latter was connected with the VME crate *via* an optical fibre and with NARVAL *via* TCP/IP. NARVAL stands for "Nouvelle Acquisition temps-Reel Version 1.2 Avec Linux". All the Linux processes are performed by an abstract class named Actor which is responsible for each task. In case of the tasks running on the different

computers the dataflow is handled with TCP/IP socket connection, while on the same machine with UNIX fifo.

There are three categories of actors:

- *producer*: it collect data from hardware;
- *intermediary*: it perform operations on the data receiving input and sending output from/to one or more other actors;
- *consumer*: they can only receive input from the other actors, and store the data to disk or act as histogrammers.

Each crystal, which consists of the 36 segments + core, is treated as a separate entity. With the use of the AGATA Global Trigger and Synchronization (GTS) hardware with a common 100 MHz digital clock, the data from the crystals are synchronized for each detector. Fig. 3.16 schematically presents the DAQ data flow which comes from the front end electronics. A producer actor for each AGATA detector reads the pulse traces from the front end electronics which are sent together with the timestamp information to an intermediary in order to perform the PSA and to write them to the disk by consumer. Then, the PSA data from all detectors are matched using timestamp information by an intermediary (event builder).

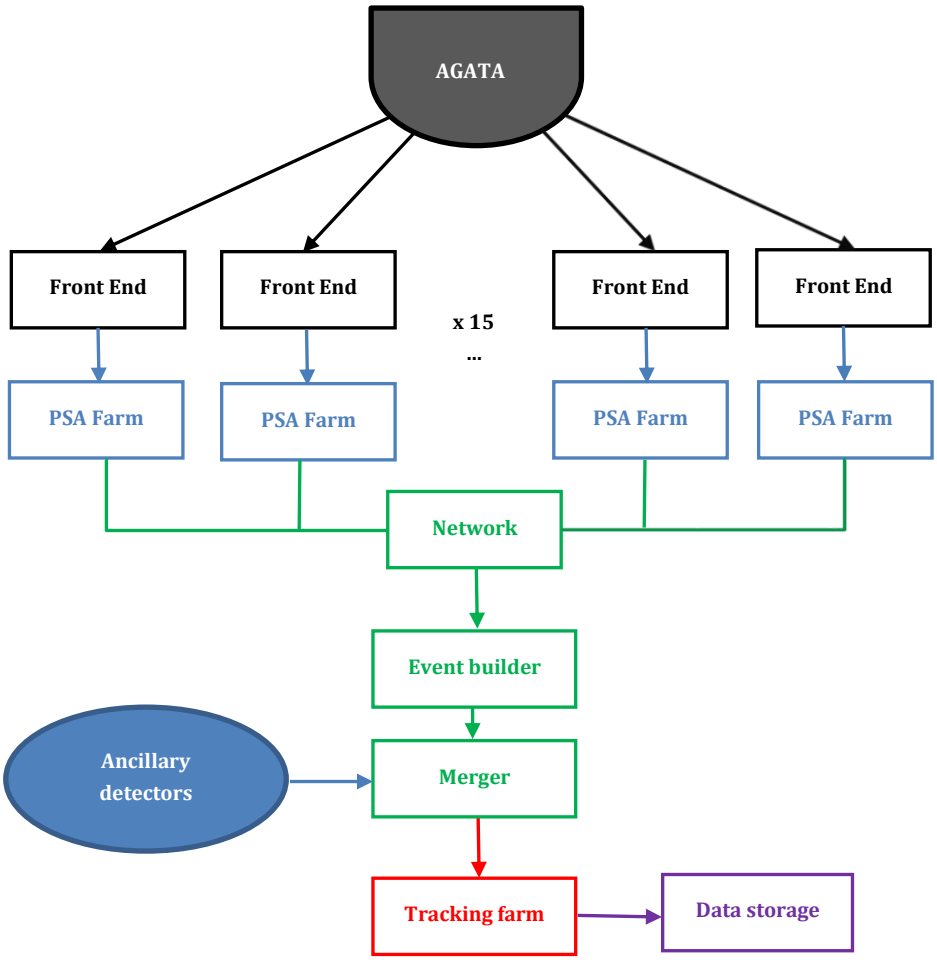

Figure 3.16: *Scheme presenting the experimental data flow. Adopted from Ref. [Gra05].*

The data from ancillary detectors are received from the KMAX acquisition by producer actor and synchronized to the GTS via the AGAVA (AGATA Ancillary VME Adapter). The VME data are sent to consumer that writes them to disk and to intermediary in order to decode the VME words and send only the actual data words to the event builder (without VME header and trailer words). Then, the ancillary data are merged with the AGATA data and send to last intermediary that performs the tracking process online.

Trigger conditions

Standard NIM electronics was used to build the master gate, which was sent *via* AGAVA as a trigger request, and had the software trigger validate it. The master gate is schematically described in Fig. 3.17 and is the logical "OR" of four conditions:

- the coincidence between TRACE and AGATA,
- the coincidence between TRACE and the scintillators,
- the TRACE scaled-down singles,
- the scintillators scaled-down singles.

The AGATA trigger was made using the analogue output of each AGATA detector (present for debug purposes), sent to standard CFD (Constant Fraction Discriminator) modules and to a logical OR. The TRACE trigger was the OR of all the pads of the two E detectors, taken from the amplifiers; and the scintillator trigger was the OR of all the HECTOR+ detectors, taken from LaBrPro. In order to separate the different classes of event, 4 channels of the TDCs were used as markers.

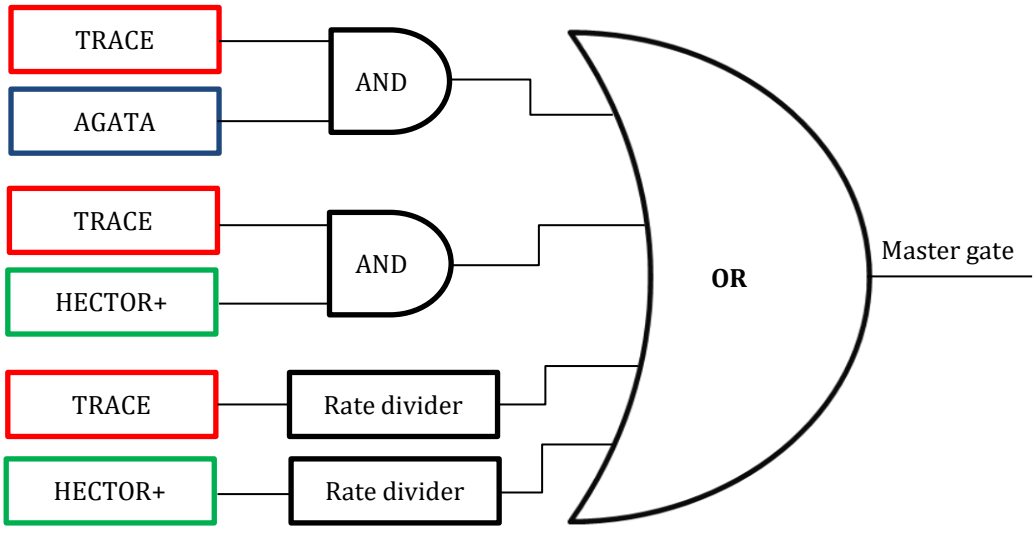

Figure 3.17: *Logic view of the trigger conditions.*

Chapter 4. DATA ANALYSIS

This chapter will briefly guide through the whole process of complex data analysis. First step was to proceed with so called the "replay" of AGATA data in order to obtain a better pulse shape analysis (PSA), compared to on-line procedure performed during experiment, and then followed by the tracking algorithm. This procedure also allowed to integrate the results from AGATA and ancillary detectors as well as to significantly reduce the amount of data, which will be described in sec. 4.1. Then, the analysis of the time spectra for each detector, with discussion of the different triggering conditions was performed (sec. 4.2). Next section (sec. 4.3) leads through the energy calibration procedure. After correction of the energy drift in silicon detectors, the selection of desired reaction channel by identification of the ions was possible (sec. 4.4). Then, the procedure of Doppler correction for the emitted γ-rays was applied (sec. 4.5) and γ-transitions only to the ground state were selected (sec. 4.6). Finally, the additional procedure of background subtraction to the γ-rays energy spectra was applied (sec. 4.7).

4.1. REPLAY OF AGATA DATA

During the experiment, PSA and γ-ray tracking (for algorithms description see sec. 3.2.4 and sec. 3.2.5) were performed in real time by the NARVAL Data Acquisition (DAQ) system, which was described in sec. 3.4. This procedure can be also applied after the experiment with a C++ emulator of NARVAL because the DAQ writes to disk a list-mode file for each detector, containing the digitized pulse signals from the segments and the timestamp information for each event. NARVAL emulator processes all the files, performing again the PSA and matching the data from different crystals, as well as matching the AGATA and ancillary data. From the point of view of the data processing it is essentially a repetition of the experiment that is why the procedure is called a "replay".

In case of the experiment which is a subject of this thesis, the calibration used online was based on a short run at the beginning of the data collecting, thus being not very accurate. Performing replay procedure allowed to apply a better calibration to the segments. It was also possible to make use of improvements in the PSA that were not available at the time of the experiment, such as the correction for neutron damage (see [Akk12]).

The replay was performed in two steps:

- At first, energy calibration and the PSA for all AGATA detectors were performed and the data consisting of γ-rays energy, position, and time information for all the segments were saved to disk.

- In the second step, the data from all the segments were merged and the tracking was performed. The data from HECTOR+ and TRACE arrays were calibrated and combined with AGATA data for each event.

The PSA is a very time consuming process, using a large amount of computing power and memory. In case of this experiment, it took about one week to perform it using 10 computers working in parallel. In contrast, once having the PSA done, tracking is much faster and thus can be repeated several times with different parameters.

The result of the PSA and tracking is given as a list-mode file in ROOT tree format. Such file contains the list of reconstructed γ-rays, together with their energy, timestamp information and the position of the first interaction, as well as the data of the ancillary detectors received from the VME crate. A dedicated sorting code was developed for the analysis of the list-mode data [Nic12].

4.2. TIME SPECTRA

This section presents the results of the time spectra analysis performed for each detector: TRACE, AGATA, and HECTOR+. This step is crucial in appropriate selection of the different coincidence conditions. This allows first to reject all random coincidences within each detector and second to extract the desired coincidences between different types of detectors in particular γ–ion detection coincidence or "singles".

4.2.1. TRACE

During the experiment, two VME Time-to-Digital Converters (TDCs) acquired a time signal for each pad of the silicon detectors. It worked in "common start" mode: each TDC channel was started by the master trigger (see sec. 3.4) and was stopped by the delayed time signal of the silicon pad. As a result, the start of all the TDCs is given by the E detectors in case of a TRACE-γ coincidence.

The obtained time spectra for one pad of ΔE and E detectors without any gating conditions are shown at Fig. 4.1. In both spectra, the strongest peak marked in blue corresponds to a coincidence between detected gammas and TRACE detectors. The peak marked in red results from self-coincidence spike corresponding to the events in which the detector opened the master gate in a "TRACE singles" event.

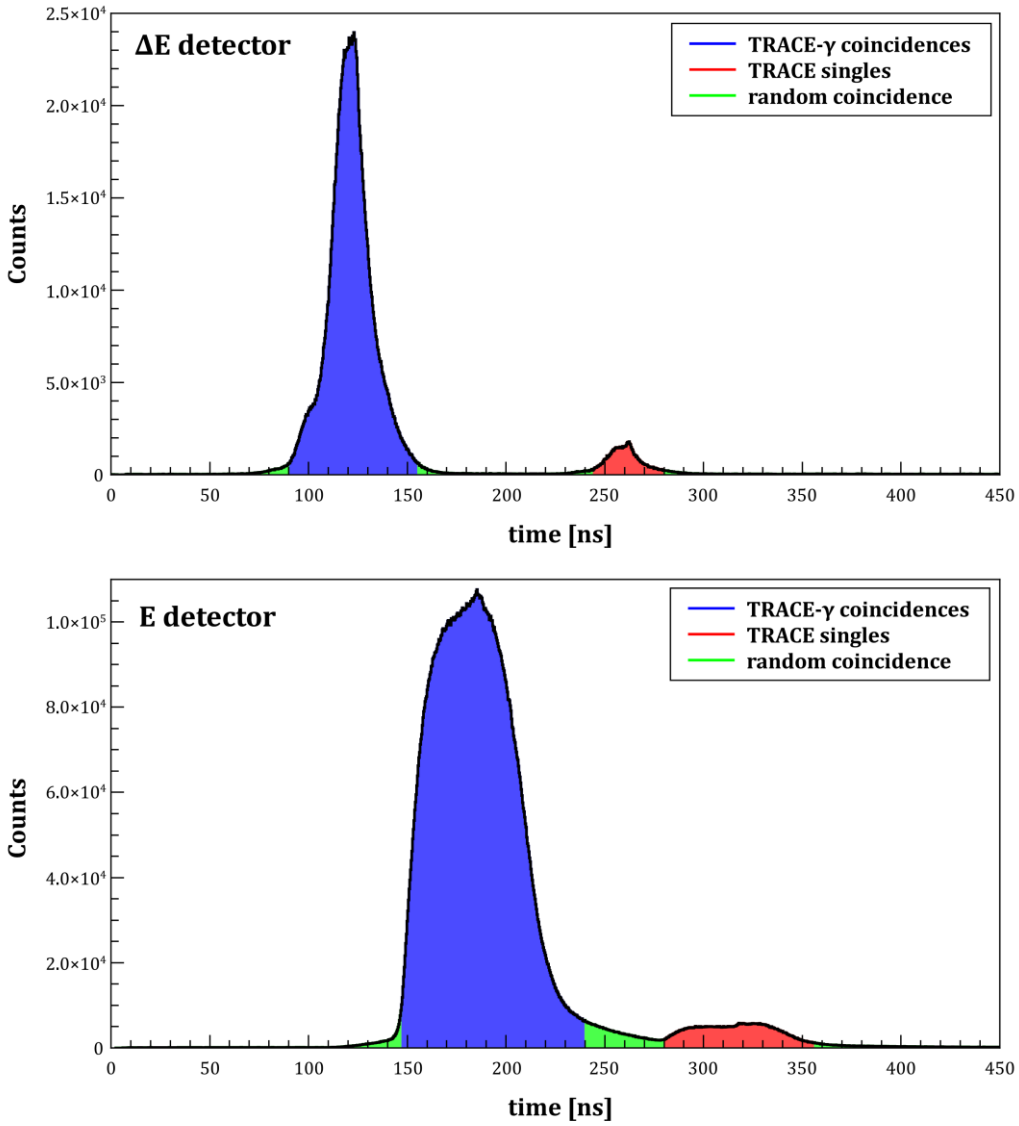

Figure 4.1: *Time spectrum for one pad of ΔE (top panel) and E (bottom panel) detectors. Black line corresponds to the spectrum without any gating conditions.*

Due to a large spread in energy and time-of-flight of the different reaction products, the timing of the silicon detectors is affected. Fig. 4.2 shows the time spectra obtained by gating on the ^{17}O scattering channel (for details on selecting reaction channels see sec. 4.4) for one pad of ΔE (left panel), and E (right panel). The FWHM of such peaks was ~11 ns for ΔE and ~21 ns for E detector. In further analysis, all TRACE spectra were gated on the time peak of the E detector.

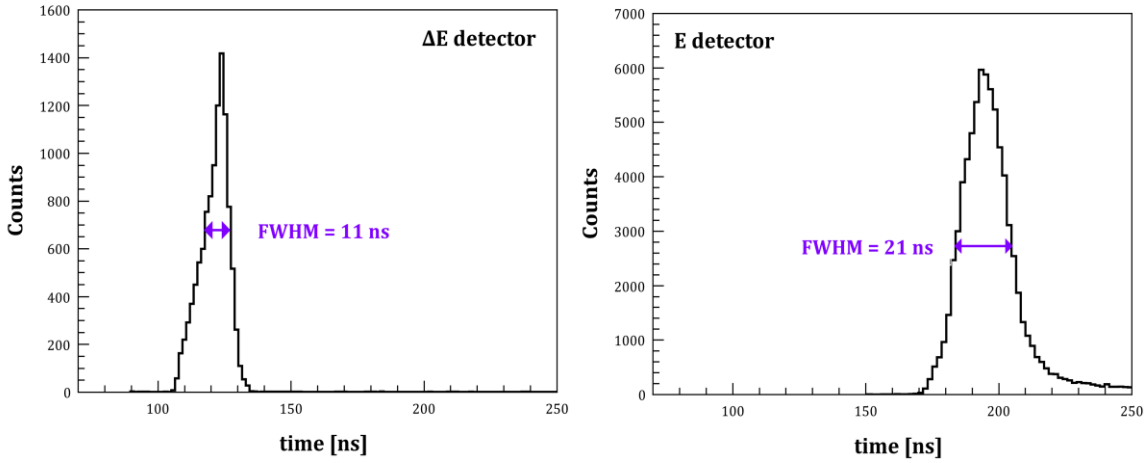

Figure 4.2: *Time spectra of ΔE (left panel), and E (right panel) detectors gated on the ^{17}O scattering channel.*

4.2.2. AGATA

Each γ-ray reconstructed by the tracking algorithm is associated to a timestamp (T_{AGATA}), which measures the absolute time from the start of the Global Trigger and Synchronization (GTS) clock in steps of 10 ns. A more precise information is given by the PSA, using a Constant Fraction Discriminator (CFD) to determine the start time of the signal (t_{CFD}). Thus, the detection time of the gamma relative to the start time of the GTS is given be the sum:

$$time_{TT} = T_{AGATA} + t_{CDF} \tag{4.1}$$

First step of the analysis was to compare the time spectra between crystals. This was done for the whole experimental data set for all studied nuclei: ^{124}Sn, ^{140}Ce, ^{208}Pb. The spectra in Fig. 4.3, top panel, were obtained by choosing one AGATA detector as a reference and measuring the time difference between that detector and all the others. A spread of timing of the order of ~10 ns between the crystals is observed; this was corrected by adding an offset to the timing information of each crystal, obtaining the spectra shown in the bottom panel of Fig. 4.3. The detection time of the γ-ray must be correlated to the detection time of the ^{17}O ions in order to obtain physical information of interest. The timing information of ion detection is given by the GTS timestamp of the ancillary branch of the acquisition, again with a step of 10 ns. In order to obtain a better precision, it was possible to add to the timestamp so-called "phase shift", which is acquired by one channel of the TDCs and measures when the VME master gate was opened relative to the GTS clock. The AGATA time relative to the trigger time was therefore built as:

$$T_{gamma} = T_{AGATA} + t_{CFD} - T_{AGAVA} - t_{phase_{shift}} \tag{4.2}$$

where T_{AGATA} and T_{AGAVA} are the timestamps for the gamma and for the ancillary branch of the DAQ.

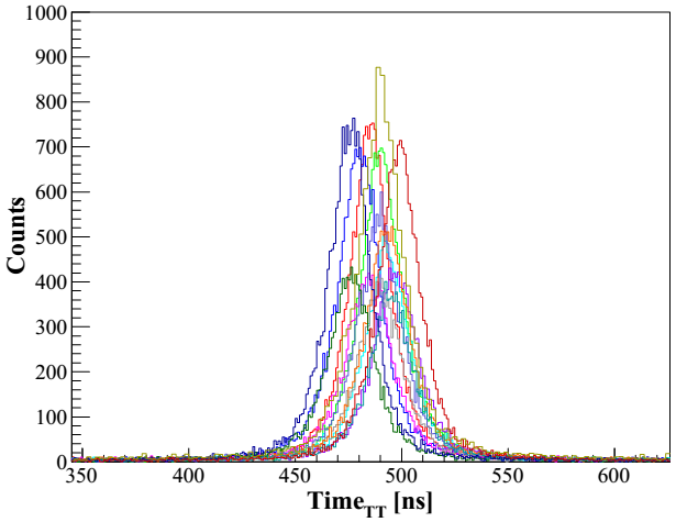

(a) Not Allined

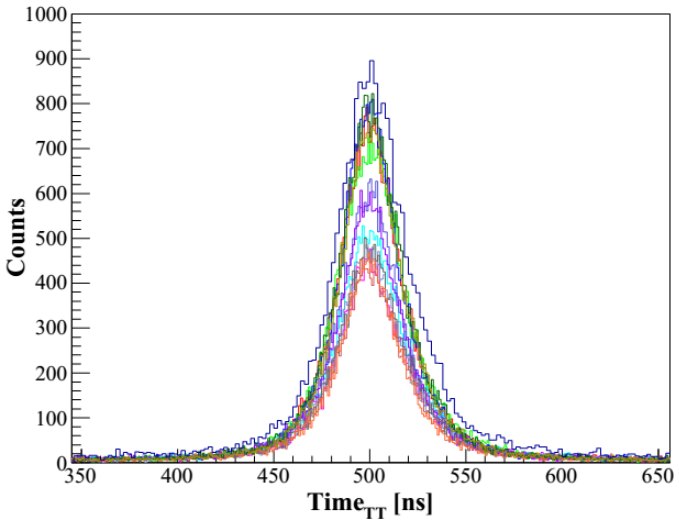

(b) Allined

Figure 4.3: *Time spectra of all AGATA detectors against a reference one, before (a) and after (b) the correction of the spread of different crystals timing. Taken from Ref. [Pel14b].*

Fig. 4.4 shows the obtained time spectrum of AGATA without any gating conditions. The strongest peak marked in blue corresponds to a coincidence between AGATA and TRACE detectors. The large peak marked in red results from random coincidences of AGATA with a scaled-down "HECTOR singles" trigger. The last structure marked in purple corresponds to a coincidences between AGATA and a scaled-down "TRACE singles" trigger.

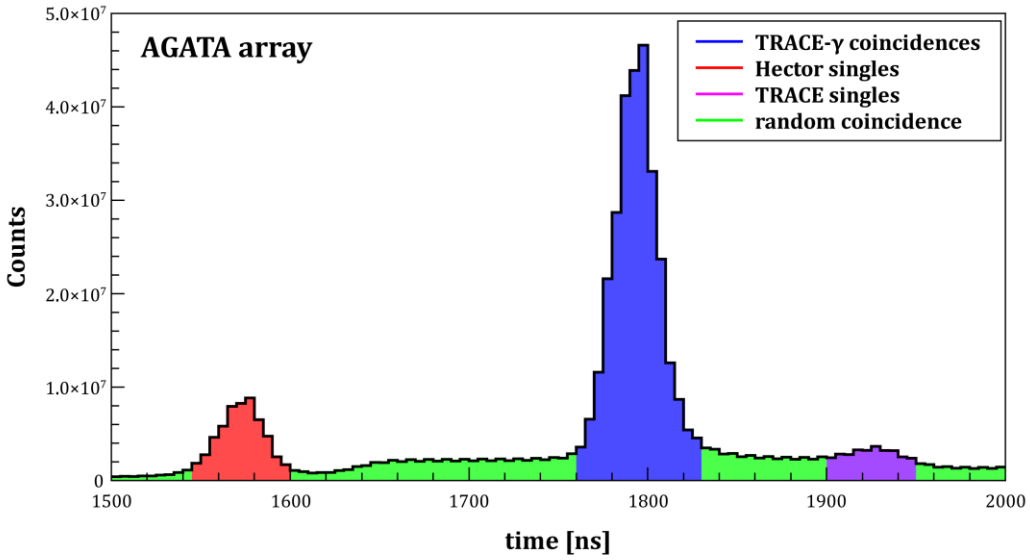

Figure 4.4: *Time spectrum of AGATA detector. Black line corresponds to the spectrum without any gating conditions. Coincidences with different triggers are marked.*

The Fig. 4.5 shows the time spectrum for the AGATA detectors under the gating condition that a ^{17}O ion is detected in the TRACE telescopes. The peak has a FWHM of ~26 ns, and the area marked in blue corresponds to the gate on time that was applied to the AGATA spectra in the further analysis.

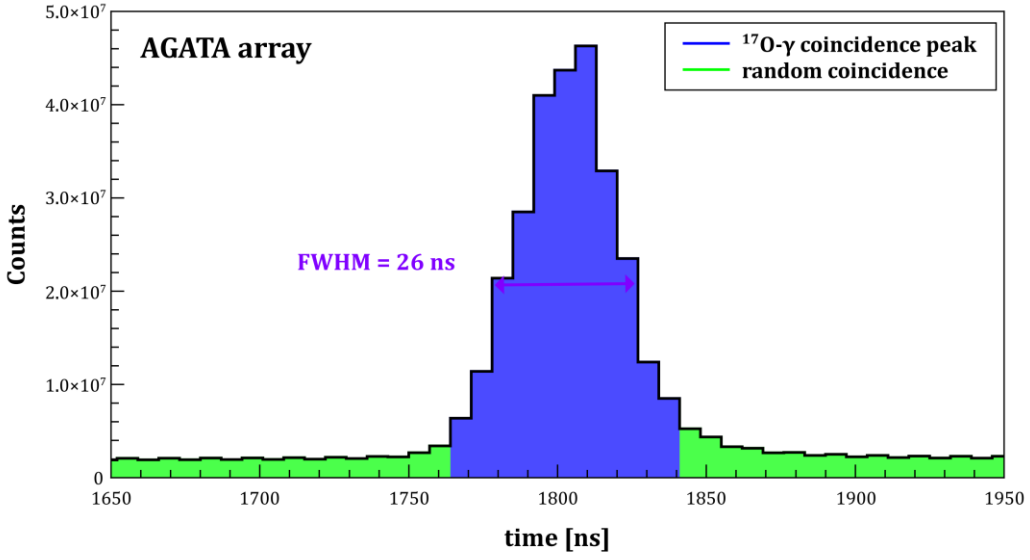

Figure 4.5: *^{17}O gated time spectrum of AGATA versus TRACE array.*

4.2.3. HECTOR+

During the experiment, a CAEN V878 VME TDC acquired a time signal for each $LaBr_3$:Ce crystal. The timing information was obtained from the CFD output of the LaBrPro module, sent through an active delay unit and then to the TDCs. As for the case of silicon telescopes, the TDCs worked in "common start" mode and the Master Gate was opened, for gamma-ion coincidence events, by the pads of the TRACE "E" detectors.

Fig. 4.6 shows the time spectrum of one $LaBr_3$:Ce without any gating conditions. The strong peak marked in blue corresponds to a coincidence between HECTOR+ and TRACE detectors. The peak marked in red results from self-coincidence corresponding to the events in which the detector opened the master gate in a "scintillator singles" event. The last structure marked in purple corresponds to coincidences between HECTOR+ and a scaled-down "TRACE singles" trigger.

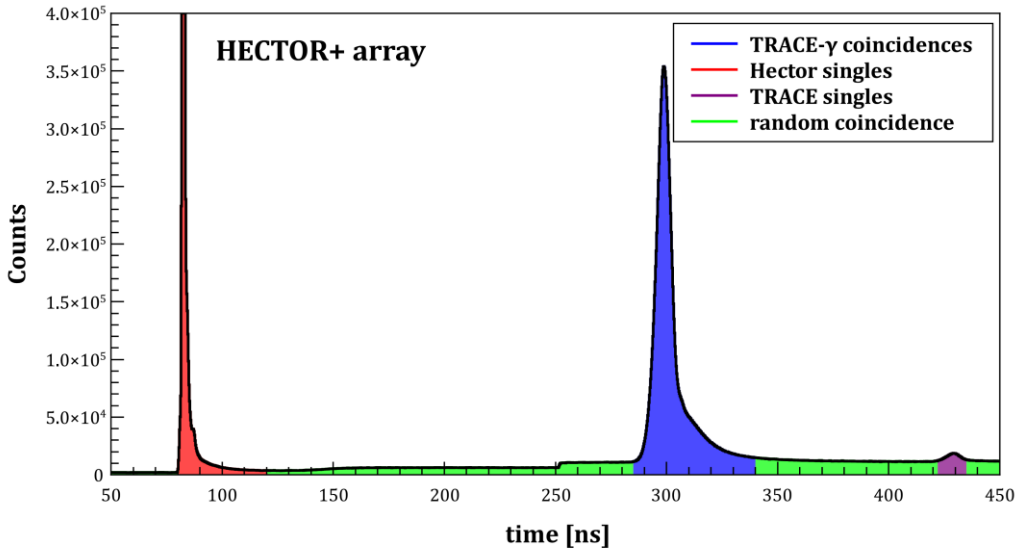

Figure 4.6: *Overall (no condition) time spectrum of single $LaBr_3$:Ce detector. Coincidences with different triggers are marked.*

Large spread in energy of all reaction products results in the width of the coincidence spectrum. The time spectrum for one of $LaBr_3$:Ce detectors with the gating condition that an ^{17}O ion is detected in the telescopes is shown in Fig. 4.7. The FWHM of the peak is ~6 ns and results from the timing resolution and the time walk of the Si detectors. In further analysis, all time spectra are gated on coincidence peak depicted in blue, which is 6 ns large. The tail of the peak on the right (marked in red) is caused by neutrons.

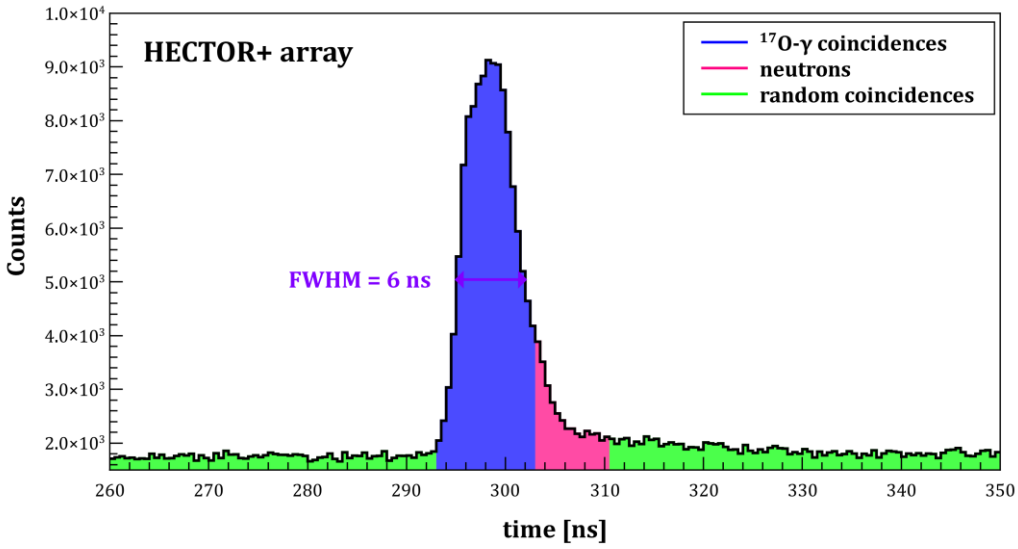

Figure 4.7: *^{17}O gated time spectrum of a single $LaBr_3$:Ce detector of HECTOR+ array.*

4.3. ENERGY CALIBRATION

4.3.1. TRACE

The energy calibration of charged particle detectors with radioactive sources is only possible up to a few MeV, because there are no long-lived emitters of alpha particles with higher energies. However, the calibration is possible at the base of energy loss in the ΔE and E detectors. Knowing the energy corresponding to the projectile elastic scattering, for each ΔE and E pads the calibration coefficients were extracted. Fig. 4.8 shows the energy spectra of ΔE (a) and E (b) for one pad of the silicon detectors after applying the calibration procedure. Finally, it was possible to sum the deposited energies and obtain the total kinetic energy (TKE) spectrum shown in panel (c) of Fig. 4.8.

Fig. 4.9 shows the total number of scattering events detected in each pad of silicon detectors. As explained in sec. 3.1, not all pads were used during the experiment and they are marked as white empty ones. Also, three pads were not working correctly and denoted with (B). It can be observed, that the pads in the right telescope have larger statistics than the pads in the left telescope, meaning that they also had a larger counting rate. This suggests an imperfect symmetry of the Si detectors along the beam axis. Another explanation may come from the fact that ^{140}Ce measurement was performed at the end of experiment, thus the Si detectors performance might be deteriorated and the efficiencies of Si detectors might had been slightly different due to radiation damages. This will be also considered in sec. 5.3.1.

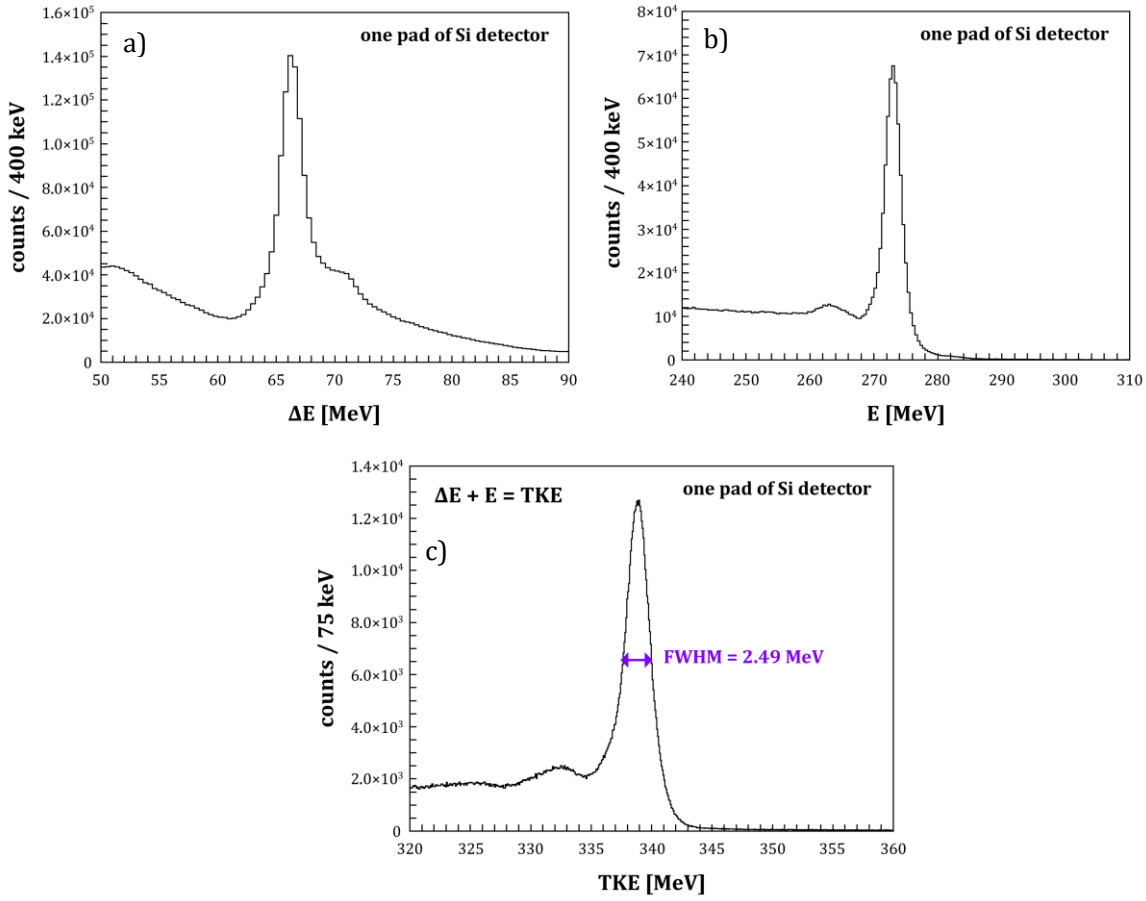

Figure 4.8: *Calibrated spectra of energy deposited in the first layer of one pad of silicon detector - ΔE (a), second layer - E (b), and the total - TKE (c).*

	Left					right				
	0	**1**	**2**	**3**	**4**	**5**	**6**	**7**	**8**	**9**
0				$1.02 \cdot 10^5$	$1.09 \cdot 10^5$	$2.83 \cdot 10^5$	B			
1				$1.47 \cdot 10^5$	$4.49 \cdot 10^5$	$1.12 \cdot 10^6$	$4.49 \cdot 10^5$			
2				$1.88 \cdot 10^5$	$1.73 \cdot 10^6$	$4.68 \cdot 10^6$	$1.68 \cdot 10^6$			
3			$2.95 \cdot 10^5$	$1.25 \cdot 10^6$	$5.76 \cdot 10^6$	$1.91 \cdot 10^7$	$4.97 \cdot 10^6$	$1.36 \cdot 10^6$		
4			$4.87 \cdot 10^5$	$2.50 \cdot 10^6$	$8.87 \cdot 10^6$	$4.96 \cdot 10^7$	$1.15 \cdot 10^7$	$2.50 \cdot 10^6$		
5		B	$7.04 \cdot 10^5$	B	$2.00 \cdot 10^7$	$4.39 \cdot 10^7$	$1.82 \cdot 10^7$	$3.40 \cdot 10^6$		
6			$5.79 \cdot 10^5$	$2.93 \cdot 10^6$	$1.63 \cdot 10^7$	$5.78 \cdot 10^7$	$1.71 \cdot 10^7$	$3.12 \cdot 10^6$		
7			$4.29 \cdot 10^5$	$1.83 \cdot 10^6$	$8.57 \cdot 10^6$	$4.24 \cdot 10^7$	$9.37 \cdot 10^6$			
8			$2.02 \cdot 10^5$	$8.11 \cdot 10^5$	$2.90 \cdot 10^6$	$2.04 \cdot 10^7$	$7.67 \cdot 10^6$	$3.26 \cdot 10^6$		
9				$2.97 \cdot 10^5$	$8.97 \cdot 10^5$	$2.90 \cdot 10^6$	$1.70 \cdot 10^6$			
10				$1.15 \cdot 10^5$	$2.66 \cdot 10^5$	$7.46 \cdot 10^5$	$3.18 \cdot 10^5$			
11				$5.08 \cdot 10^4$	$1.12 \cdot 10^5$	$1.93 \cdot 10^5$	$1.44 \cdot 10^5$			

Figure 4.9: *Counting rates for the pads of the silicon detectors.*

4.3.2. AGATA

The energy calibration of the AGATA array was performed once together with PSA, during the first part of the replay process. Deduced calibration parameters were valid for the whole data concerning studied nuclei: ^{124}Sn, ^{140}Ce, ^{208}Pb. Fig. 4.10 shows the energy spectrum used for the calibration obtained at the base of the calibration runs with ^{137}Cs, ^{60}Co and ^{88}Y γ-rays sources. For each segment of 15 detectors and for the core electrode, the calibration coefficients were calculated.

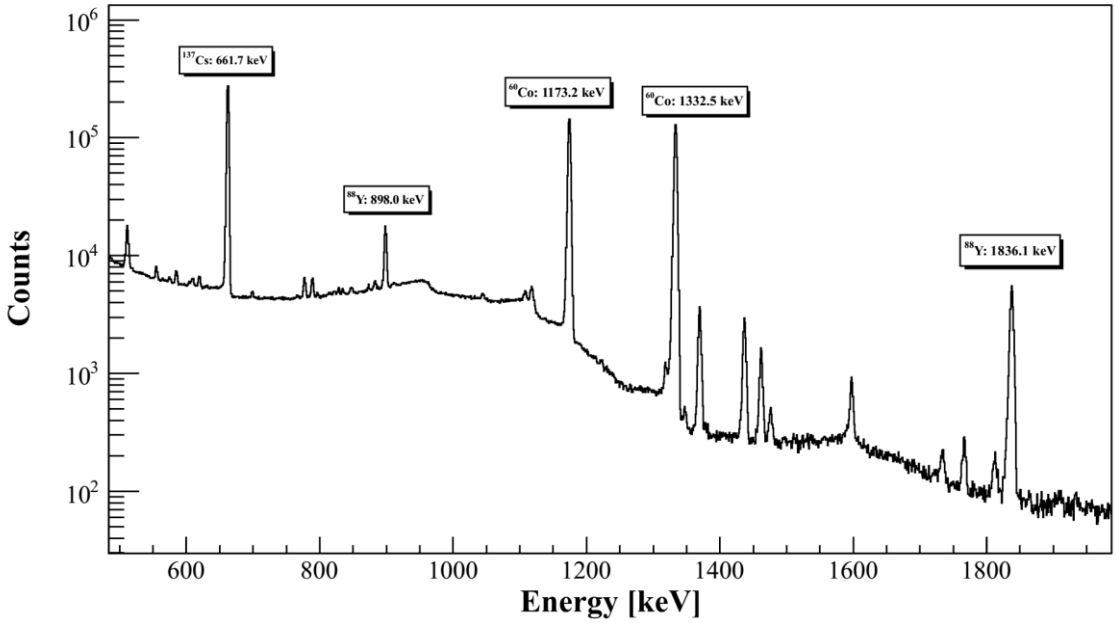

Figure 4.10: γ-rays e*nergy spectrum of ^{137}Cs, ^{60}Co and ^{88}Y sources measured with AGATA array. The spectrum has been obtained after recalibrating segment energies with the energy measured by the core, for each crystal. Taken from Ref. [Pel14b].*

In case of this experiment, the high dynamic range up to 20 MeV of the front-end electronic was used instead of standard dynamic range, which allows measurement only up to 4 MeV. It is known that at high energies segments show a non-linearity. This effect can be, however, taken into account as the nonlinearity concerns only segments, not the core signals. It is possible during the tracking process by requiring for every event that the sum of the segment energies to be equal to the energy measured in the core. This should neither affect the performance of tracking algorithm, nor reduce the energy resolution of reconstructed γ–rays.

The gain stability over time was checked by choosing a set of reference lines from in-beam spectra and comparing the measured energy with the known value for each crystal and each run. To compensate small instability, a linear calibration was applied and the coefficient of the linear term was plotted, as shown in Fig. 4.11. The observed gain fluctuation over the one-week measurement was less than 0.3% indicating very good stability of the AGATA array.

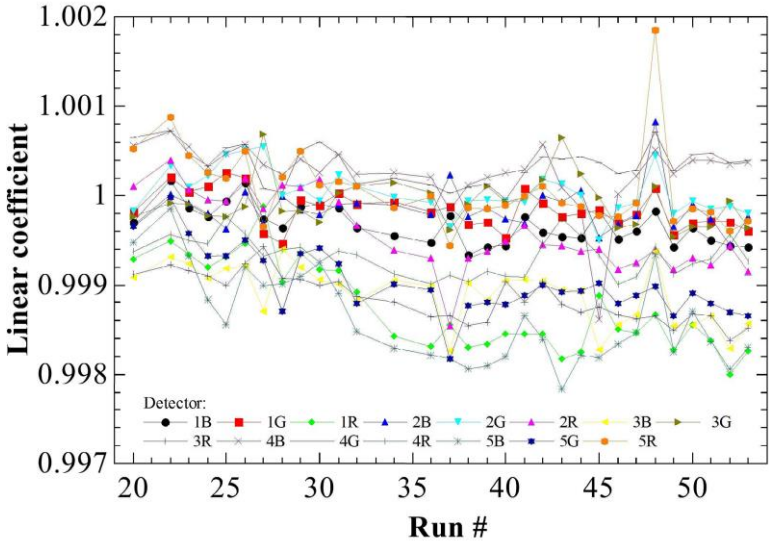

Figure 4.11: *The coefficient of the linear term of the recalibration fit plotted for each crystal and for each experimental run. Taken from Ref. [Pel14b].*

4.3.3. HECTOR+

Energy calibration for each of nine $LaBr_3$:Ce detectors was done using standard ^{137}Cs, ^{60}Co sources. However, because of observed drift of energy during the course of experiment, it was necessary to recalibrate the spectra. For that purpose, spectra were gated on the ^{17}O scattering channel and two know transitions of ^{140}Ce were used for recalibration:

- E_γ = 1596.21 keV (2^+@1596 → g.s.)
- E_γ = 867.85 keV (3^-@2464 → 2^+@1596).

Fig. 4.12. shows the energy spectra obtained for each $LaBr_3$:Ce detector after recalibration procedure. Good alignment between detectors is demonstrated. The peak 511 keV annihilation peak is not observed for most of the detectors because of the high-energy thresholds set.

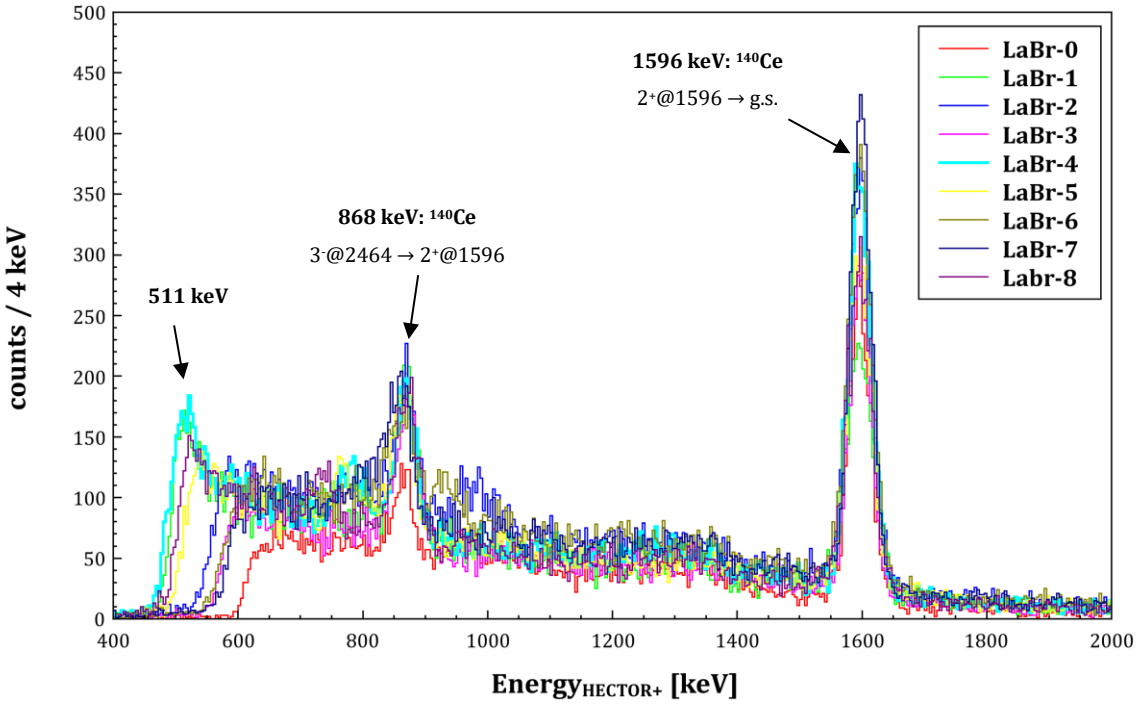

Figure 4.12: *Energy spectra obtained for each $LaBr_3$:Ce detector after recalibration procedure.*

4.4. ION IDENTIFICATION

First purpose of the TRACE data analysis is to select the reaction channels by ion identification. It is possible at the base of the ΔE-TKE matrices for each pad of the silicon detectors. Such matrices can be obtained by plotting the two-dimensional histograms of the energy deposited in the first layer of the Si detector (ΔE) *versus* total kinetic energy (TKE) deposited in both layers. From such matrices, as seen in Fig. 4.13, ^{17}O can be easily separated from other nuclei, in particular ^{16}O. It is then possible to select the ^{17}O channel by making cut on ΔE-TKE matrices for each pad.

It should be noted that Fig. 4.13 shows the data for one pad that were collected at the beginning of the experiment (about 11% of the whole data). As seen from the left panel of Fig. 4.14, which presents the data from the whole experiment, the quality of the matrix became very poor with time. There was a drift of the signal amplitude during the experiment in silicon detectors that needs to be corrected. This will be further discussed in next section.

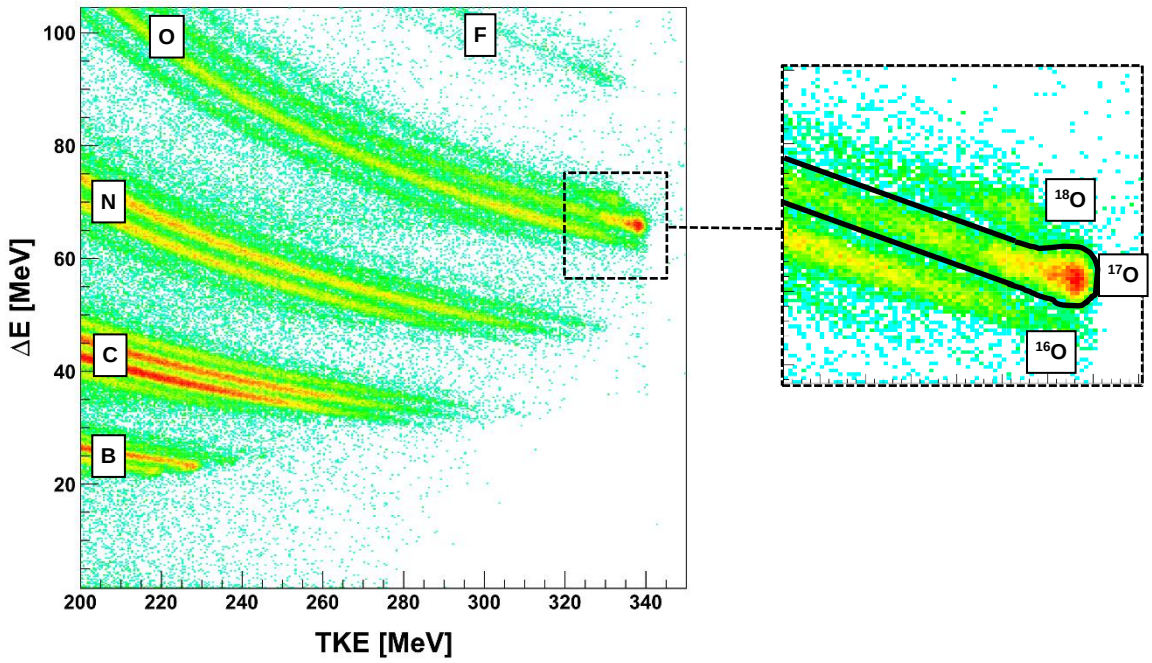

Figure 4.13: *Example of the two-dimensional histogram of the energy deposited in the first layer of Si detector (ΔE) versus total kinetic energy (TKE) deposited in both layers measured during the first run. Clear mass separation between the oxygen isotopes is demonstrated on the right panel.*

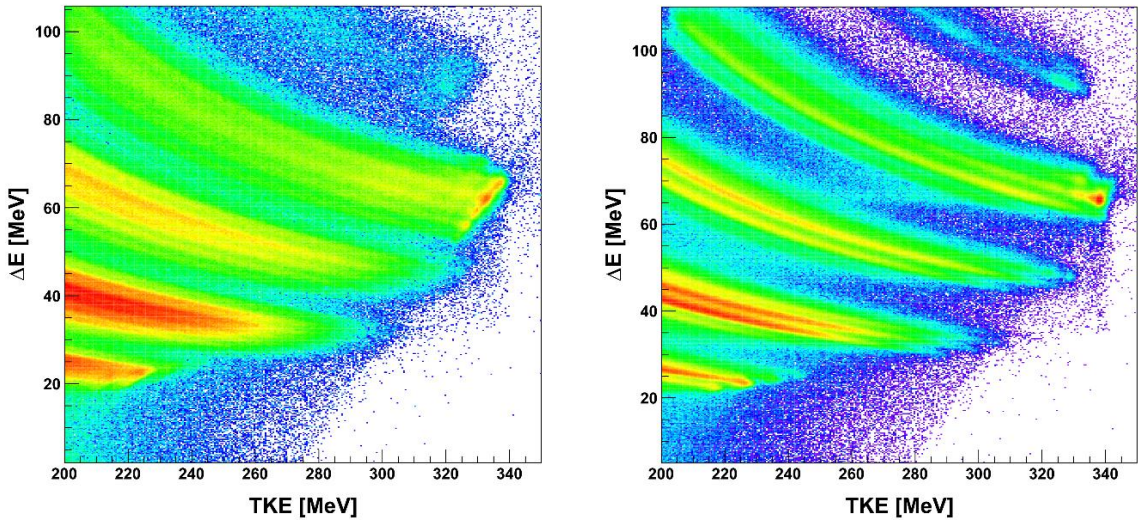

Figure 4.14: *Example of the two-dimensional histogram of the energy deposited in the first layer of Si detector (ΔE) versus total kinetic energy (TKE) deposited in both layers for one pad for the full data set. Left panel shows the matrix with visible gain drift, while right panel shows the matrix for the same pad after applying correction procedure.*

4.4.1. Drift correction of silicon detectors

The effect of energy drift was already observed in the previous experiment for ^{208}Pb [Nic12]. During the course of the data collection, the leakage current passing through the detectors has steadily increased, due to the radiation damage caused by the scattered beam. This effect also causes a gradual loss of energy resolution and a variation over time of the energy gain for the pads that were more damaged by radiation, namely those suffering a higher counting rate. In the ^{208}Pb case, only small drift of the total kinetic energy (TKE - whole energy deposited in both layers) was taken into account and corrected. However, in case of ^{140}Ce experiment, it is clearly visible that significant drift of the total deposited energy is due to the first layer of silicon detector (ΔE). This is shown in details in the left panel of Fig. 4.15, where energies deposited in both layers of silicon detectors are plotted against the time of experiment.

The drift for the TKE parameter was corrected by performing a fit of the elastic peak every ~5 million events and then obtaining a series of recalibration coefficients ($coeff_{TKE}$) that were used to an event-by-event correction. The same procedure was done for the E parameter resulting in the analogous set of coefficients ($coeff_E$). For the ΔE, it was not possible to use the same procedure with the elastic peak. That is why the coefficients for the correction of ΔE drift were obtained as a difference between the coefficients for TKE and E parameters:

$$coeff_{\Delta E} = coeff_{TKE} - coeff_E \tag{4.3}$$

The result of the correction can be seen in the right panel of Fig. 4.15. The corrected ΔE-TKE matrix is shown in right panel of Fig. 4.14, and as compared to the matrix before correction (left panel of the same figure) demonstrates the accuracy of the method.

The spectra of the total kinetic energy deposited in one pad of the silicon detector before and after applying the procedure described in this section are shown in Fig. 4.16. Once the energy drift is corrected, the elastic peak at the energy 337.94 MeV is clearly visible. The FWHM of this peak is ~2.4 MeV. This is related to energy resolution of the Si telescopes that limits the precision of excitation energy measurement.

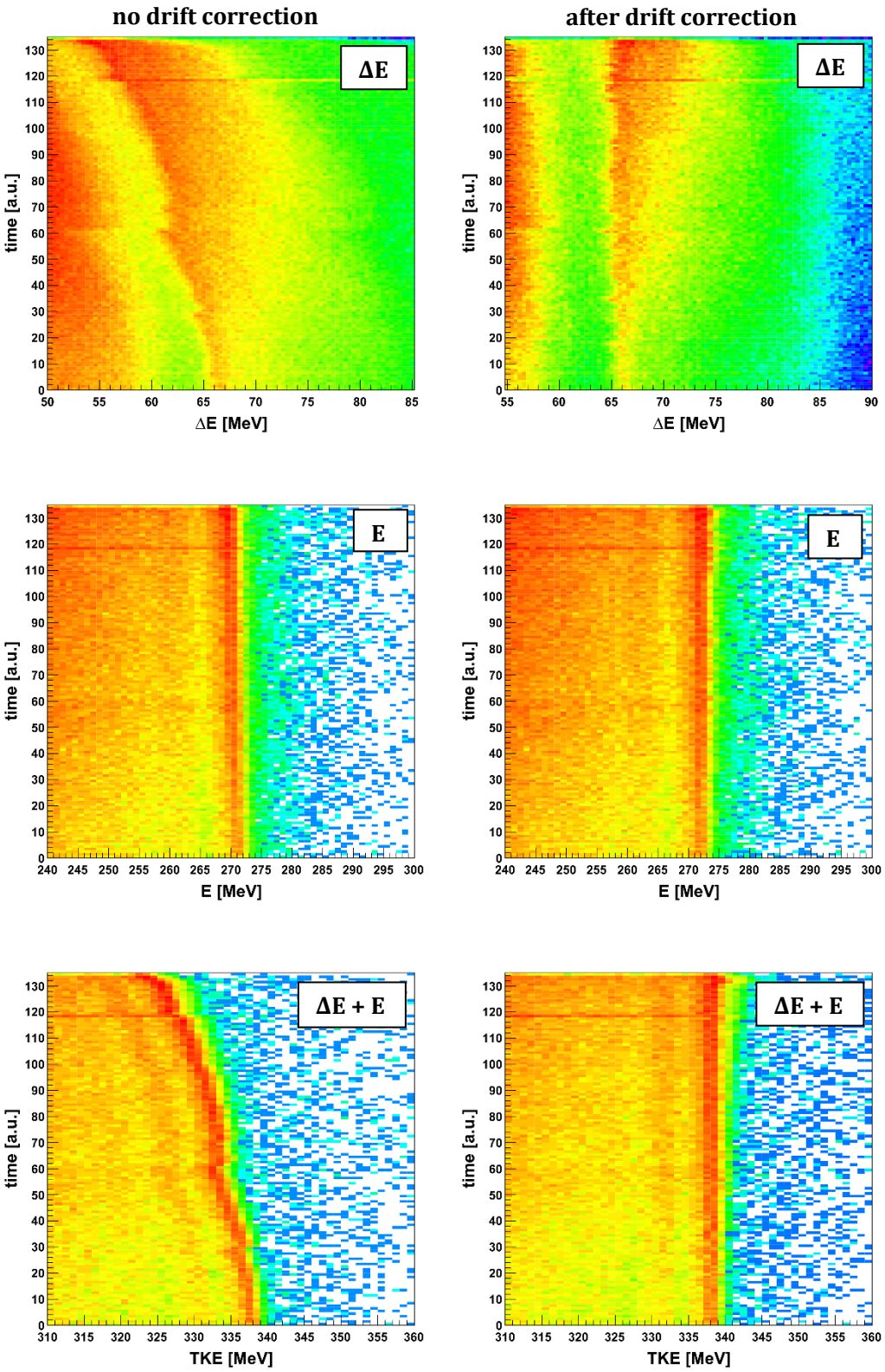

Figure 4.15: *The energy drift observed during experiment in first layer - ΔE (top panel), second layer - E (middle panel) and total kinetic energy deposited in both layers - TKE (bottom panel).*

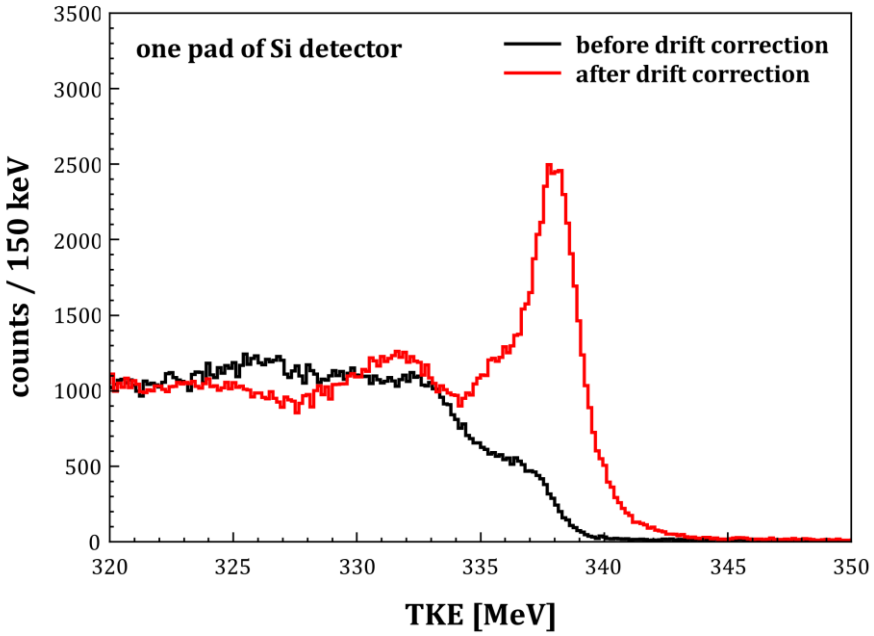

Figure 4.16: *Spectrum of the total kinetic energy for the one pad of the silicon detector before (black line) and after drift correction (red line).*

4.4.2. Selection of ^{17}O scattering channel

The ^{17}O channel was selected by making a graphical cut on the ΔE-TKE matrices for each pad of the silicon detectors according to the example shown in Fig. 4.13.

The spectra of γ-energy measured in AGATA and HECTOR+ requiring the gate on time coincidence peak (black line) and additionally after selecting ^{17}O channel (blue line) are presented in Fig. 4.17. As pointed out at the top panel of Fig. 4.17, for the spectra measured with AGATA, γ-transitions from ^{140}Ce are enhanced with respect to the background transitions at the annihilation peak and neutron capture transitions. It is also interesting to observe the lines from ^{139}Ce and even ^{138}Ce, which result from evaporation of one and two neutrons, respectively, from target nucleus. Much lower energy resolution of HECTOR+ in low energy region does not allow to identify γ-transitions with such precision as for HPGe array. However, the effect of selecting the ^{17}O channel is also clearly visible in this case (Fig. 4.17, bottom panel).

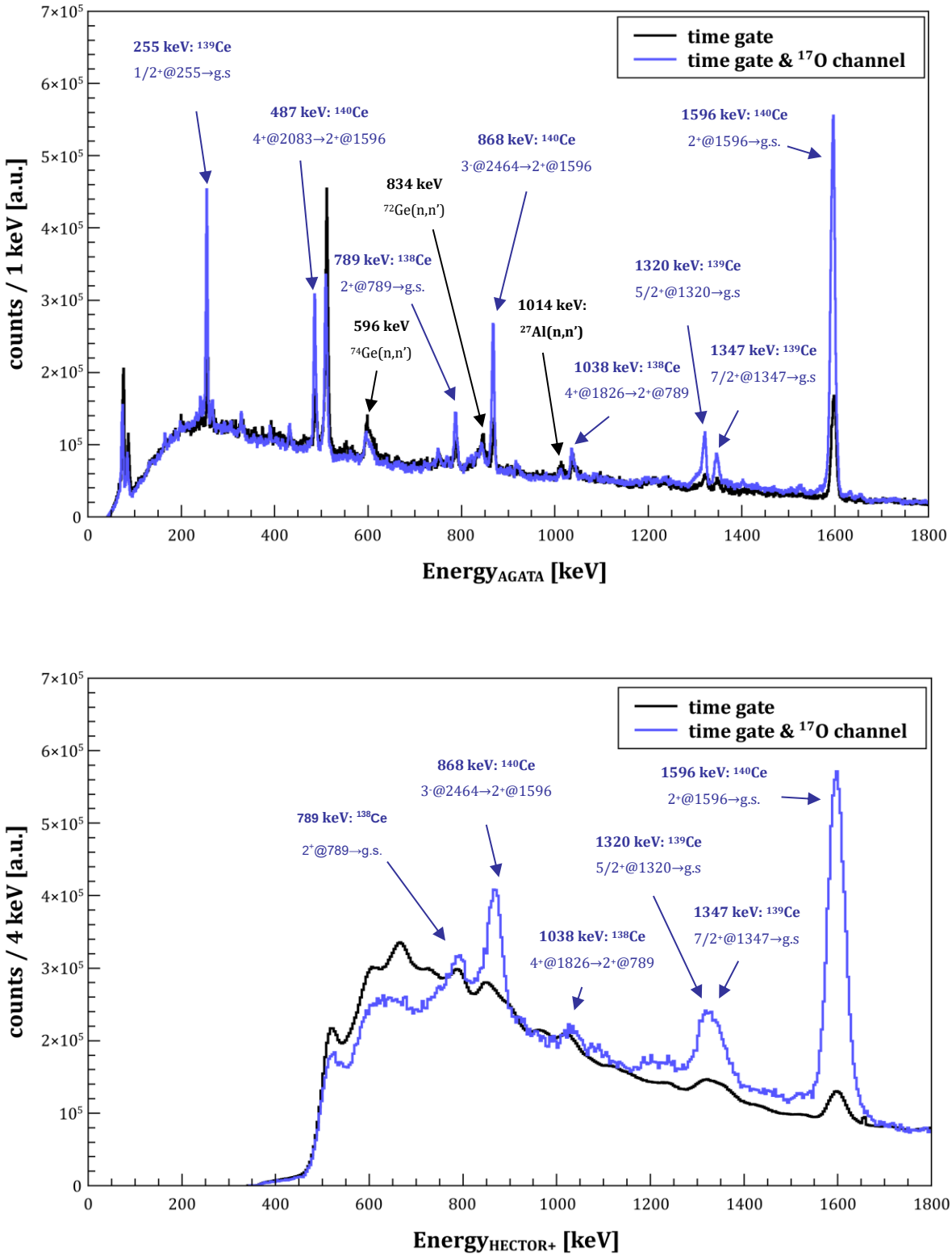

Figure 4.17: *Spectra of γ-energy measured in AGATA (top panel) and HECTOR+ (bottom panel) before (black line) and after (blue line) selecting the ^{17}O channel. Some of identified γ-transitions are marked. Spectra are normalized to the background.*

4.5. DOPPLER CORRECTION

In case when nucleus emits γ-rays in-flight, the detected line energy is shifted due to the Doppler effect, which needs to be corrected. Exploiting the position sensitivity of AGATA, HECTOR+ and TRACE arrays it was possible to perform the precise Doppler shift correction.

The direction of γ-ray velocity vector was determined at the base of the position of the first interaction point in the AGATA crystals. As mentioned in sec. 3.2.5, this was possible due to the PSA and tracking algorithm, which reconstruct the path of the γ-ray within the detectors giving the coordinates of the interaction points in the AGATA frame of reference. The precision of angle estimation for AGATA is at the level of 1°. In the case of HECOTR+, the γ-ray velocity vector was determined by the position of the centres of the $LaBr_3$ crystals.

The direction of projectile velocity vector was determined using the position of the pad of TRACE array in which the ion was detected. As the geometry of the silicon detectors is not spherical, the optimization procedure for the pads position was applied as follows. The pad was moved in a 1 cm x 1 cm large grid with a 1 mm step and for each position the energy and FWHM of known gamma ray was obtained. The best result corresponded to the optimal position used in the analysis. The procedure was applied for the data measured with the ^{208}Pb target that had the same geometries as the ^{140}Ce. For the rest of the analysis, the optimal positions found in this way as the reference position of the TRACE telescopes were used.

The Doppler shit correction was done using the relativistic formula:

$$E_{corr} = E_{lab}\frac{1-\beta cos\theta}{\sqrt{1-\beta^2}} \tag{4.4}$$

where E_{lab} is the energy measured in the laboratory frame of reference, E_{corr} is the energy of the emitter frame of reference, and θ is the angle between the emitter velocity vector and the γ-ray velocity vector and $\beta=v/c$ is the velocity of the emitter.

The Doppler correction could be done separately for the γ-rays emitted by the beam-like nucleus or the target-like nucleus. Both procedures will be described in the following section.

4.5.1. Correction for target-like nucleus

As mentioned before, the velocity of the ^{140}Ce nucleus is at the level of 0.5% speed of light. The value is rather small but it causes a serious shift of the emitted γ-rays energy, especially in high-energy region, as seen in Fig.4.19 for the two transitions. As can be observed for the strong transition at 3118 keV, the Doppler effect resulted even in splitting of the peak, which is associated with registration of scattered ^{17}O by the Si detectors at different positions (left and right detectors).

In order to perform the correction, the angle for the velocity vector of the target nucleus was estimated at the base of a measurement for ^{17}O detected in Si detectors and then calculated using the reaction kinematics. The description of kinematics and necessary equations are presented in Appendix A. The precision of angle estimation for the TRACE is at the level of 3°.

The velocities of ^{17}O and ^{140}Ce nuclei required for calculations were simulated using LISE package [Baz02] and set constant as $\beta(^{17}O) = 0.203$ and $\beta(^{140}Ce) = 0.00528$. The idea of estimating the velocity vector of recoiling target nucleus at the base of a measurement for beam nucleus is shown in Fig. 4.18.

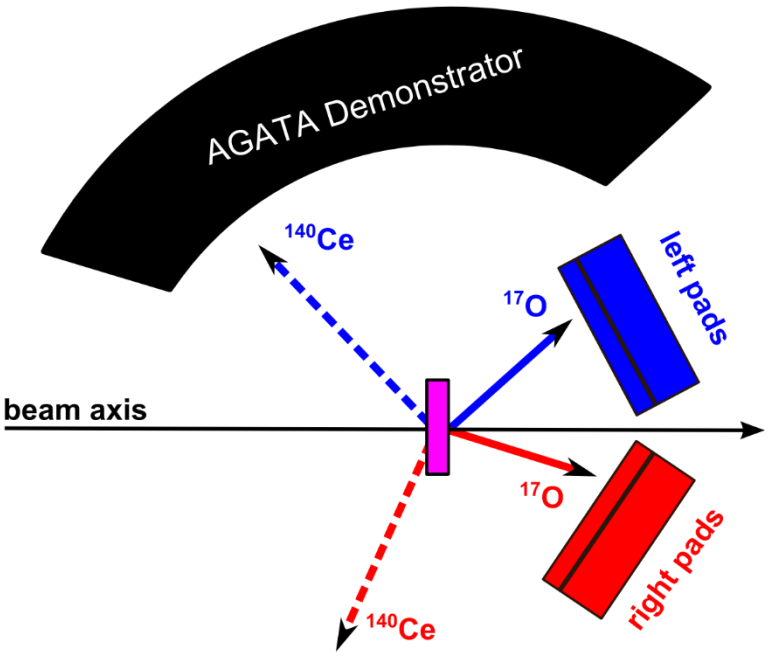

Figure 4.18: *Scheme illustrating the reaction kinematics used for estimation of recoiling nucleus velocity vector at the base of a measurement for ^{17}O scattered beam.*

The Doppler shift correction of γ-rays emitted from ^{140}Ce was performed in event-by-event mode. As presented in Fig. 4.19, after applying the correction procedure (red line) the energy of the centroid is adjusted and broadening effect significantly reduced.

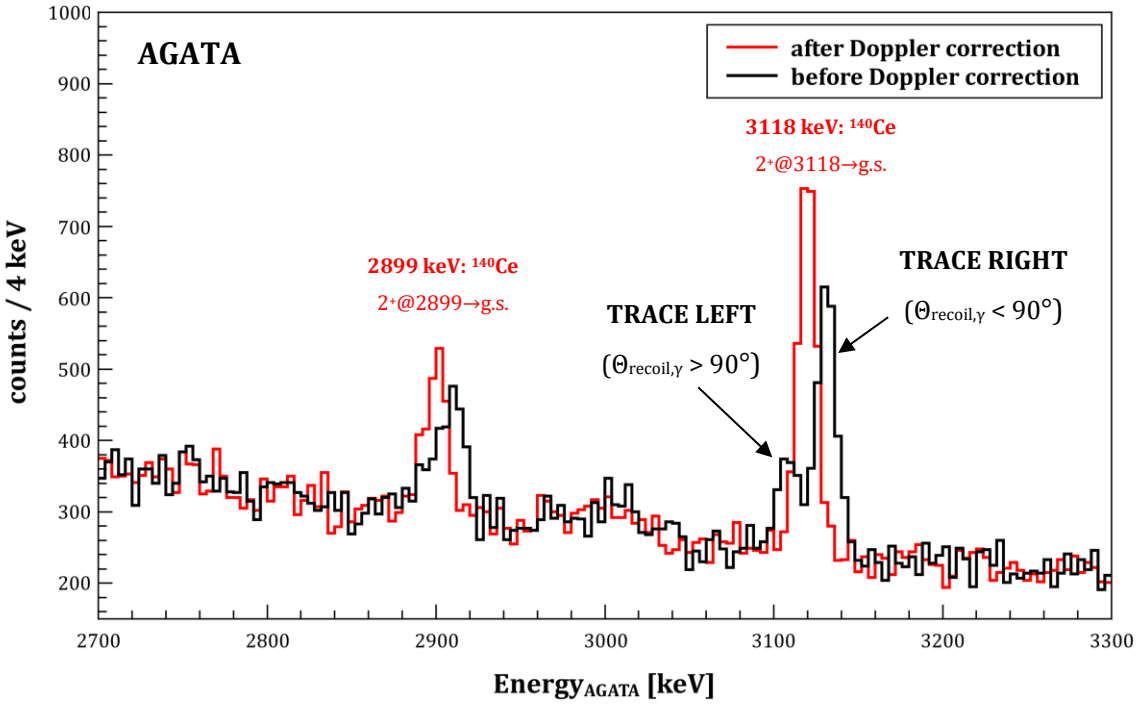

Figure 4.19: *The Doppler effect correction for the two transitions in ^{140}Ce. The black line shows the spectrum before the Doppler correction and the red line represents the spectrum after correction.*

4.5.2. Correction for beam-like nucleus

As the γ-decay from the beam-like nuclei is not the subject of this study, its Doppler correction was not required. However, it is interesting to study, as the next generation γ-spectrometers are challenged to detect the γ-rays emitted in-flight by fast radioactive beams. As mentioned before, the velocity of the beam nuclei was at the level of 20% velocity of light. The optimal in this case was to study the ^{16}O as it has a strong transition at 6129 keV and in this region, the yield of γ-rays emitted from the target is relatively low.

As seen in Fig. 4.20, where ^{16}O scattering channel is selected, the Doppler effect makes impossible to observe the expected γ-transition. After performing the Doppler correction with the procedure described before and using the fixed value of β = 0.203, the significant improvement in the quality of the spectrum is observed. Similar procedure was applied to the AGATA and HECTOR+ data.

This is a very promising result for the future application of such setups.

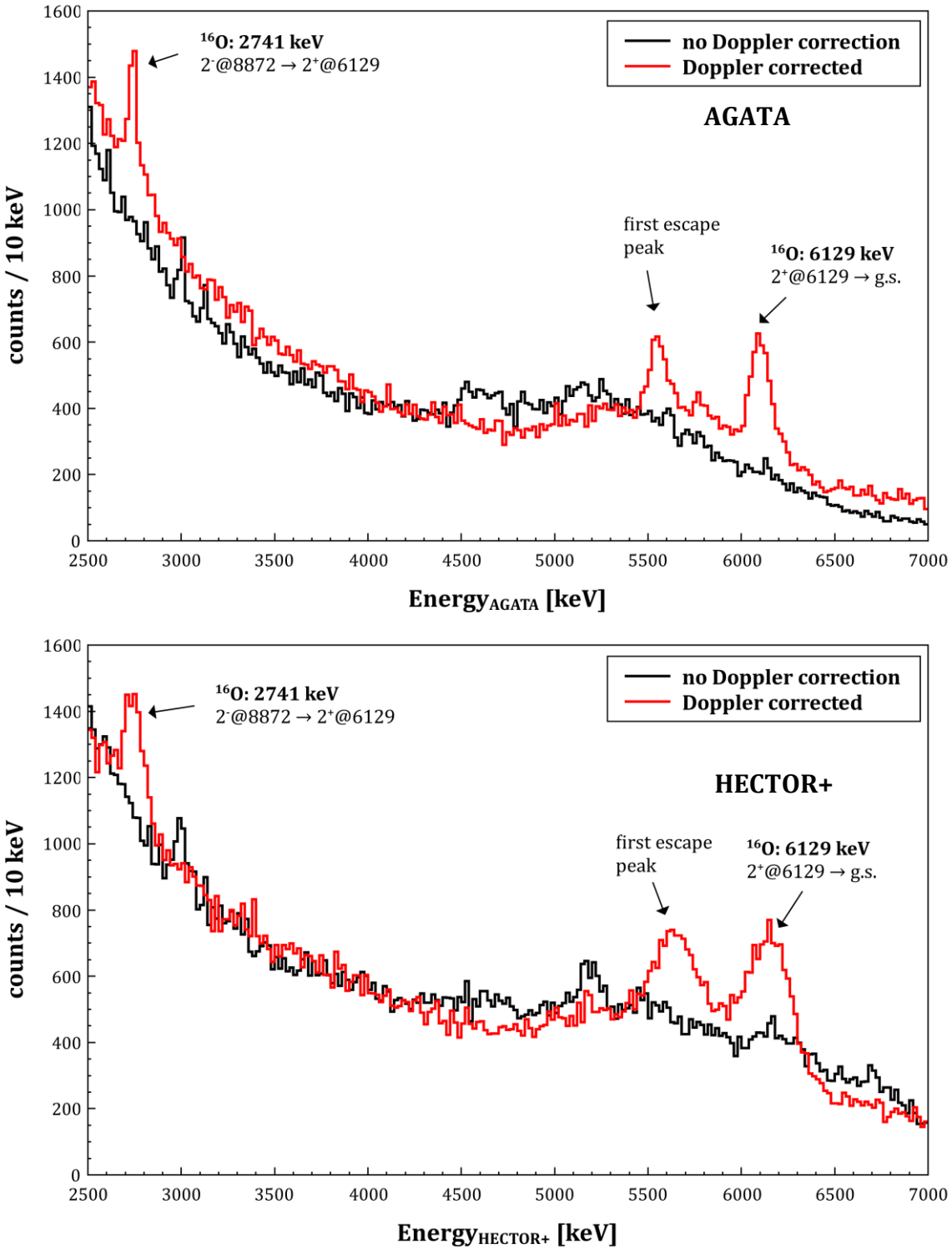

Figure 4.20: *Energy spectra of the γ –rays measured with AGATA-Demonstrator (top panel) and HECTOR+ (bottom panel) in coincidence with the ^{16}O reaction channel, measured by one pad of the TRACE telescope before (black line), and after (red line) the Doppler correction.*

4.6. SELECTION OF GROUND-STATE DECAYS

In order to select only γ-transitions to the ground state, it is possible to use the coincidence matrix between energy of the emitted γ-rays and excitation energy of the target nucleus. In the case of this experiment, it was done by plotting the two-dimensional histogram of the γ-rays energy measured in AGATA and the total kinetic energy loss (TKEL) parameter, that had been estimated as a difference between TKE measured in silicon detectors and the energy of the elastic event (337.94 MeV). Then, TKEL can be considered as excitation energy of the target nucleus. The part of the coincidence matrix between γ-rays energy measured in AGATA and the excitation energy of the ^{140}Ce nucleus is presented in Fig. 4.21. The red solid line corresponds to the γ-rays energy equal to excitation energy. It crosses the state at the energy of 1596 keV: $2^+ \longrightarrow 0^+$. Right part of the matrix is associated to the transitions to the higher-lying states (e.g. green solid line corresponds to the transitions to the 2^+ state, crossing the 868 keV: $3^- \longrightarrow 2^+$). The left part of the matrix is associated to the random coincidences with elastic scattering event.

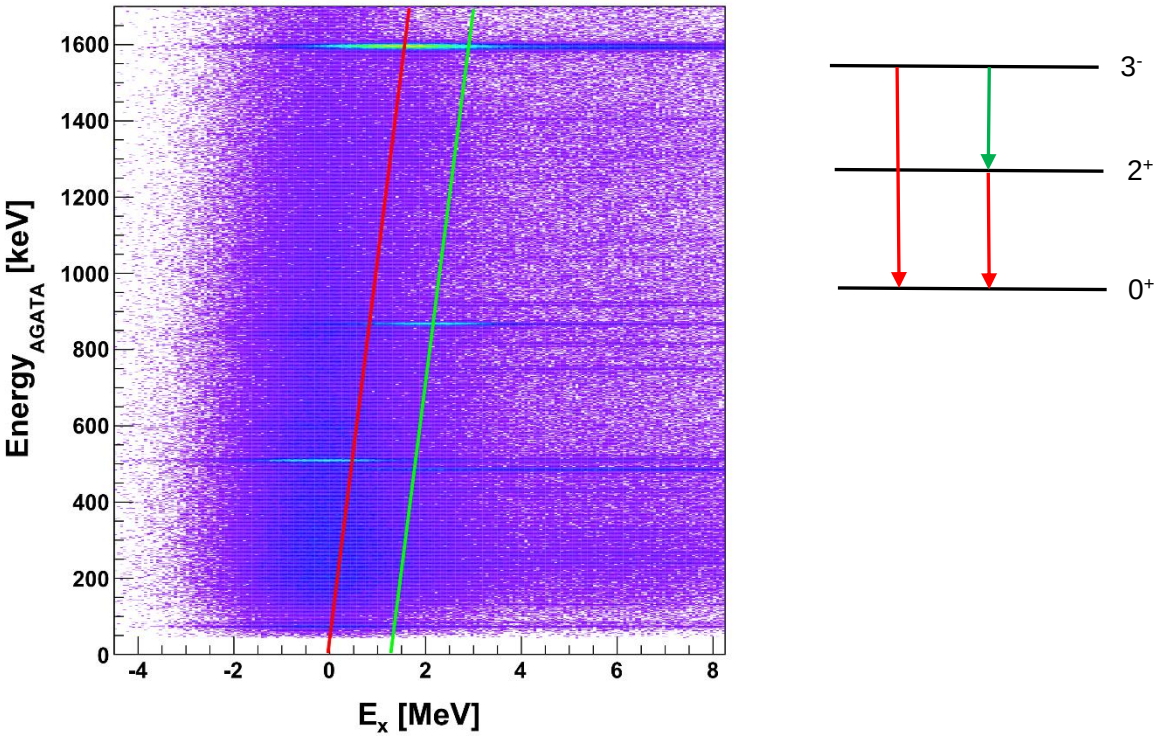

Figure 4.21: *Two-dimensional histogram of the γ-energy measured in AGATA and the excitation energy of the target nucleus. The red line corresponds to the transitions to the ground state, while green line represents transitions from higher-lying states to 2^+ as illustrated in the sketch on the right.*

Fig. 4.22 shows the full energy range histograms evaluated for the measurement from AGATA (left panel) and HECTOR+ (right panel) with depicted regions corresponding to the condition of γ-rays energy equal to excitation energy (dashed lines) within the detector resolution of ±1.2 MeV (solid lines).

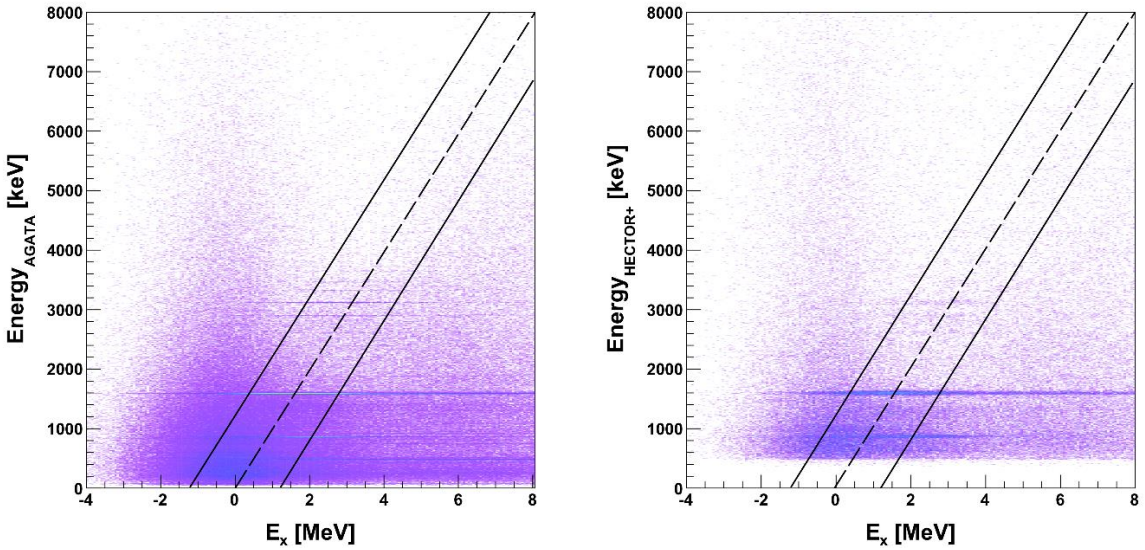

Figure 4.22: *Two-dimensional histogram of the γ-energy measured in AGATA (left panel) and HECTOR+ (right panel) and the excitation energy of the target nucleus measured with TRACE. The diagonal cut for selection of the ground state decays is marked with black solid lines.*

The spectra of γ energy measured in AGATA (Fig. 4.23) and HECTOR+ (Fig. 4.24) in different energy regions, after requesting the time coincidence and ^{17}O channel (black line) and additionally after selecting the ground state decays (blue line) are presented. As it can be observed, the γ transitions to the ground state in ^{140}Ce are enhanced and most of the transitions to higher-lying states are suppressed. The transition at 868 keV: $3^- \rightarrow 2^+$ is still present in the spectrum, which is due to not good enough energy resolution of TRACE detectors. Also γ transitions from ^{139}Ce and ^{138}Ce are supressed as they result from higher excitations, above neutron separation energies.

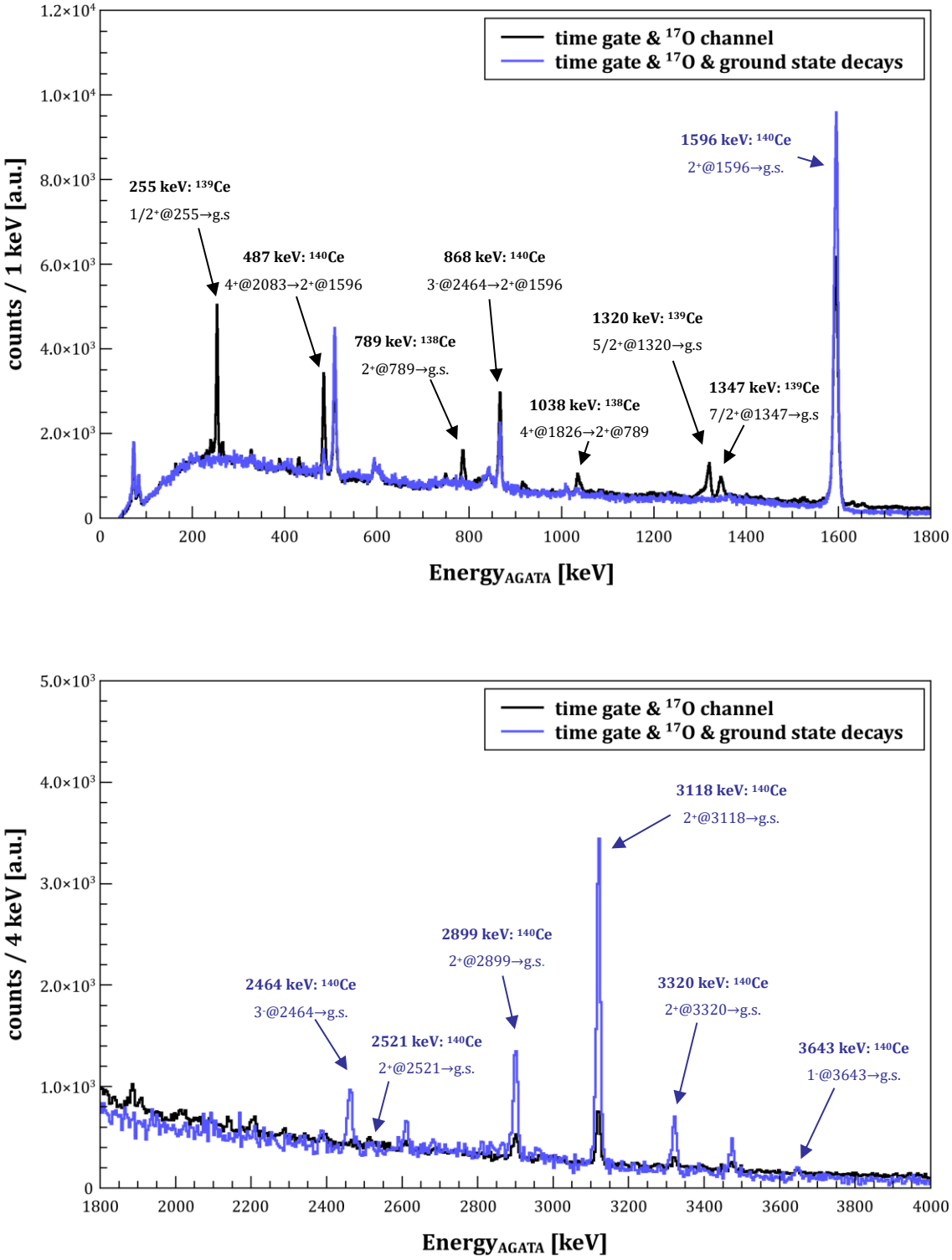

Figure 4.23: *Spectra of γ-energy measured in AGATA for lower (top panel) and higher (bottom panel) energy region, before (black line) and after (blue line) selecting the transitions to the ground state. Some of identified γ-transitions are marked.*

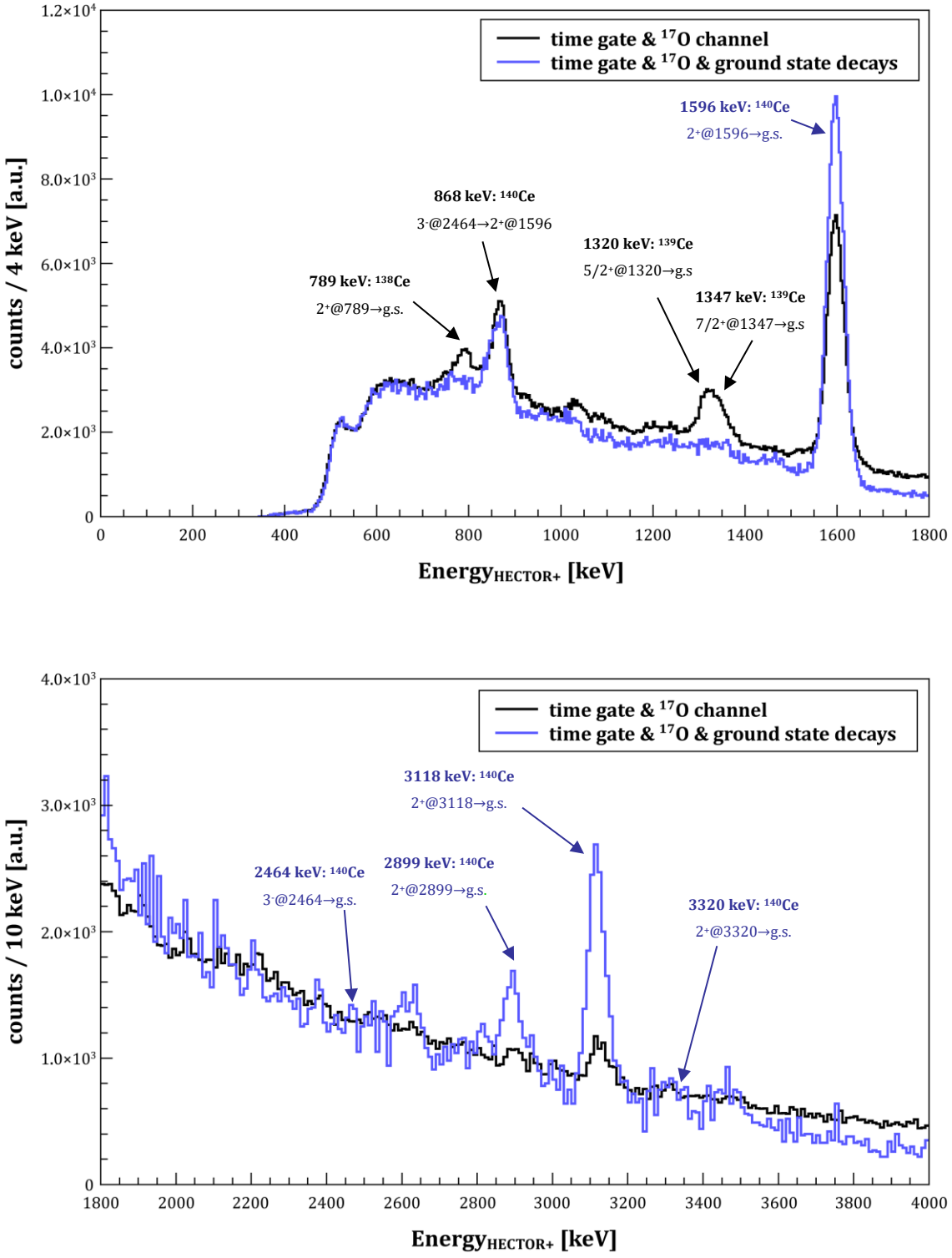

Figure 4.24: *Spectra of γ-energy measured in HECTOR+ for lower (top panel) and higher (bottom panel) energy region, before (black line) and after (blue line) selecting the transitions to the ground state. Some of identified γ-transitions are marked.*

4.7. BACKGROUND SUBTRACTION

Due to the limited energy resolution of the TRACE telescopes, the precision of selecting only ground state decays with the procedure described in sec. 4.6 was not satisfactory. Rather continuous background overlap in the PDR energy region as presented in Fig. 4.25 for AGATA (top panel) and HECTOR+ (bottom panel).

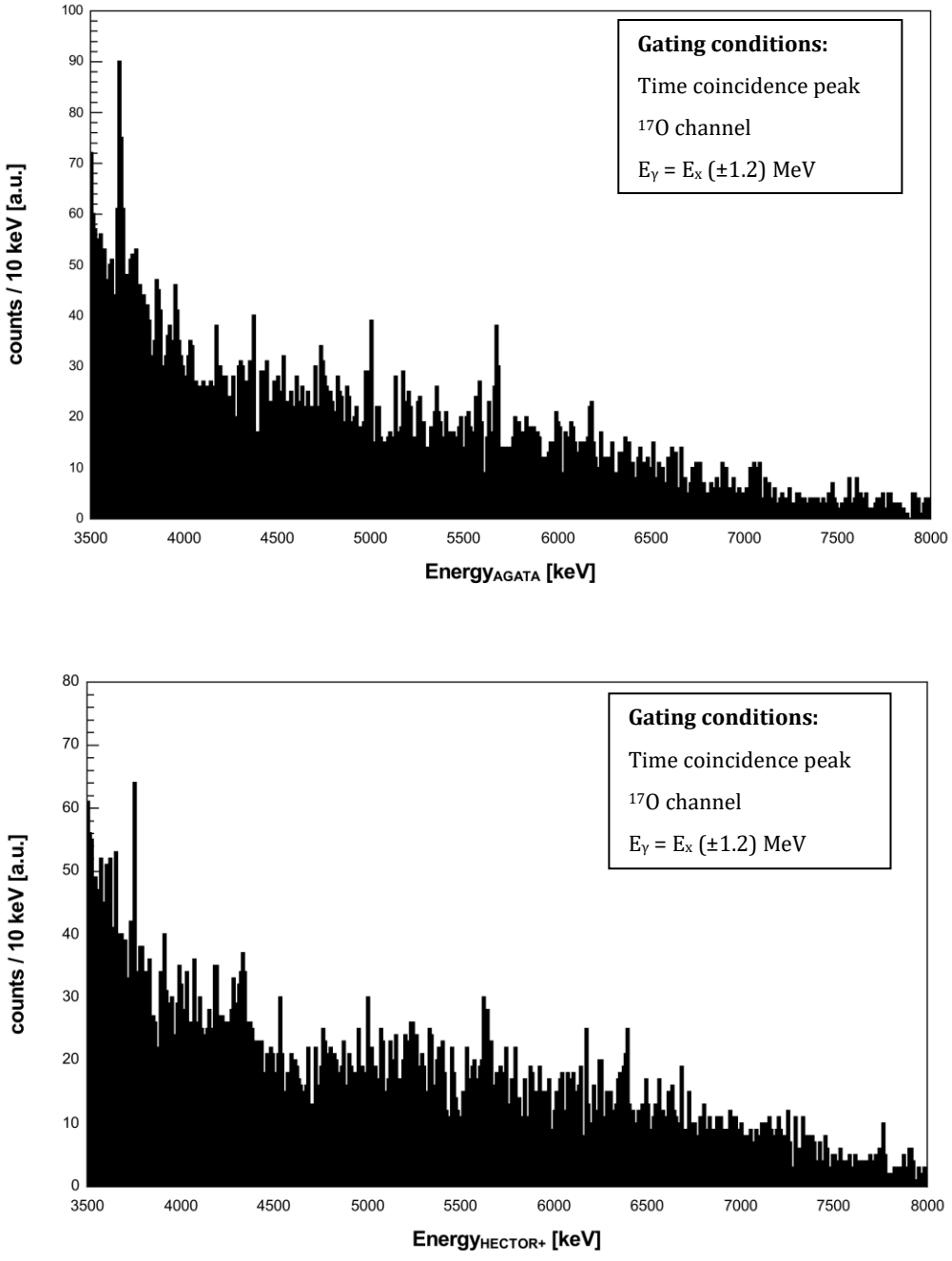

Figure 4.25: *γ-rays energy spectrum measured with AGATA (top panel) and HECTOR+ (bottom panel) gated on the diagonal cuts for the ground state transitions.*

In order to identify if this background may be associated to the decays to higher-lying states, another diagonal gate (of the same width) was applied to the E_γ–E_x coincidence matrix concentrating at higher energy region as shown in Fig. 4.26 and marked by solid red lines.

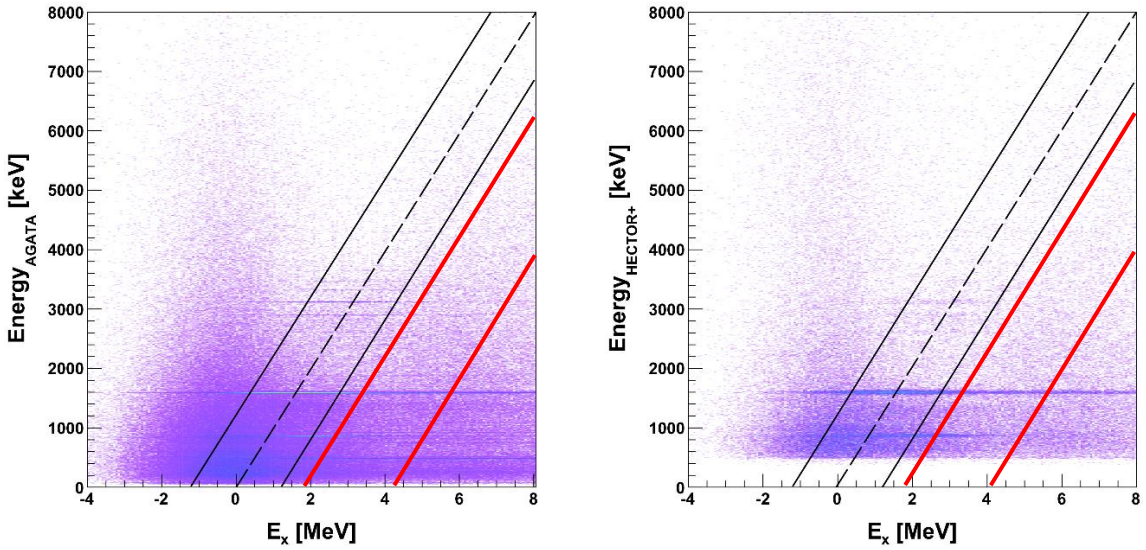

Figure 4.26: *Scattered plot showing the γ–ray energy of the ^{140}Ce, measured by the AGATA array in the (a) panel and HECTOR+ array in the (b) panel for the decay of ^{140}Ce, versus the TKEL, measured by the TRACE telescopes. The diagonal gate for the selection of the background is marked in red while black lines mark the region for the ground-state decays.*

Fig. 4.27 shows the energy spectra, in the pygmy energy range, measured with the AGATA array (top panel) and the HECTOR+ array (bottom panel) gated on the background diagonal cut presented in Fig. 4.26. Finally, those background spectra have been subtracted from the energy spectra of the ground-states decays, in order to obtain clean energy spectra of the gamma decay from the PDR states. The final spectra will be presented in Chapter 5.

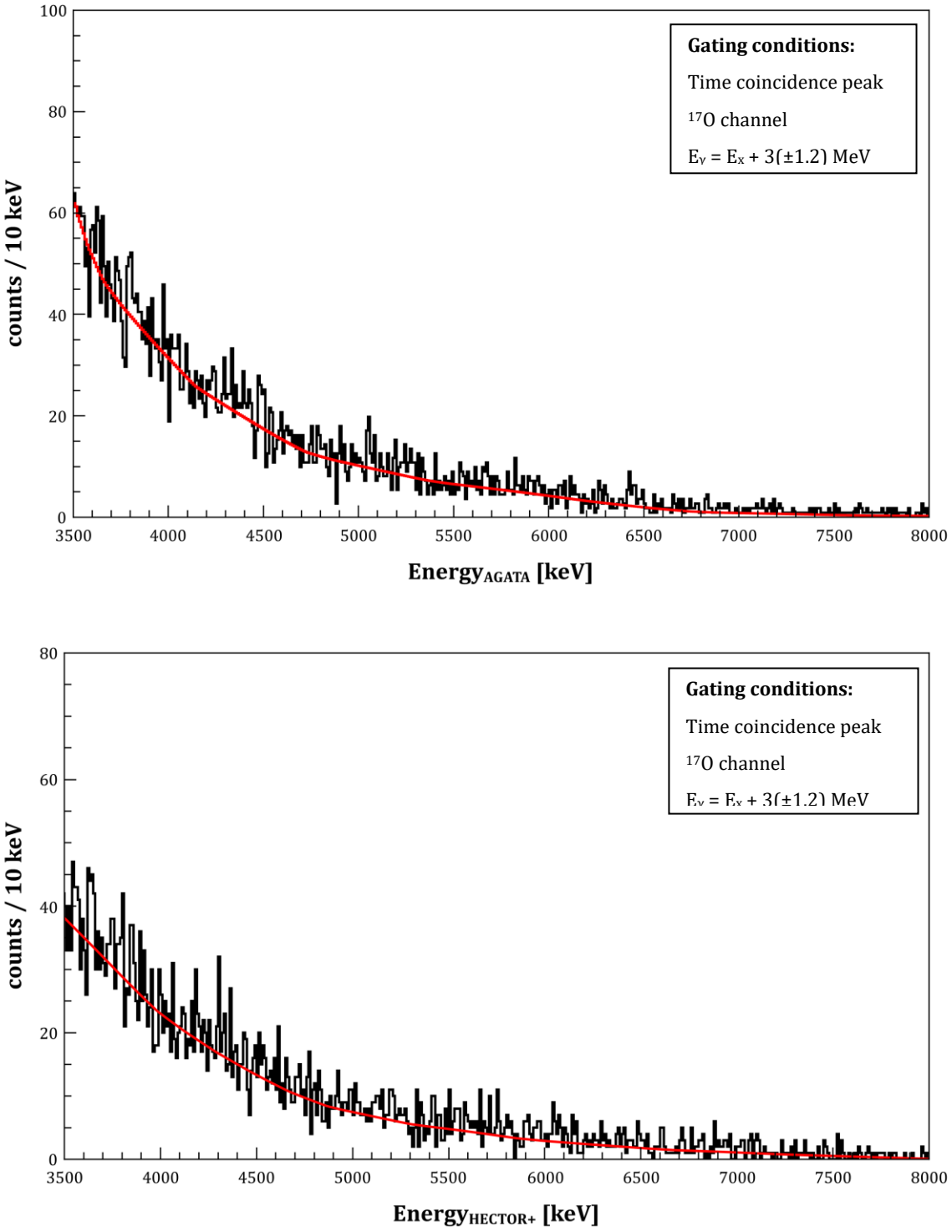

Figure 4.27: *AGATA (top panel) and HECTOR+ (bottom panel) energy spectrum corresponding to the background, obtained gating on the diagonal cuts shown in Fig. 4.26. Fits of continuous background are indicated with red lines.*

Chapter 5. RESULTS

All the most important results obtained in the study are presented in this chapter. The first section (sec. 5.1) shortly presents the result of the Giant Resonances excitation measured with Si telescopes at the base of total kinetic energy loss. The second section (sec. 5.2) discusses the γ-decay of the low-lying E1 states with the focus on possible two-phonon ($2^+ \otimes 3^-$) state and on pygmy dipole resonance as compared to the previous experiments of γ and alpha scattering. Analysis of γ-transitions multipolarity at the base of angular distributions of emitted γ-rays is presented in next section (sec. 5.3). This allowed to estimate the dipole and quadrupole components in the pygmy energy region. Last section (sec. 5.4) contains the results of the cross sections analysis obtained experimentally and compared to calculations using the Distorted Wave Born Approximation (DWBA). After necessary normalization using elastic scattering, the validation of the method is done for known 2^+ and 3^- transitions to the ground state with standard deformed Woods-Saxon potential used in DWBA. Finally, the experimental cross section analysis of 1^- pygmy states is performed and DWBA analysis is done with the use of a form factor obtained by folding the microscopically calculated transition densities.

5.1. GIANT RESONANCES EXCITATION

It is expected that inelastic scattering of ^{17}O at 20 MeV/u should populate the giant resonances in ^{140}Ce target nucleus. They should be observed in excitation energy spectra, produced from known energy of inelastic scattered ^{17}O ions, as a peak-like structure at energies given in Table 5.1. The excitation energy transferred to the target is measured by the Total Kinetic Energy Loss (TKEL) of the projectile which is estimated as a difference between Total Kinetic Energy (TKE) deposited in the silicon detectors in each event and the energy corresponding to the elastic scattering event (337.94 MeV) (see sec. 4.6).

Table 5.1: *Energy, width and reduced transition probability of a different giant resonances (multipolarity λ and isospin T quantum numbers) observed in ^{140}Ce using (e,e') reaction [Pit79].*

$E\lambda^{(T)}$	E_x [MeV]	Γ [MeV]	$B(E\lambda)^{(T)}$ [$e^2fm^{2\lambda}$]
$E2^{(0)}$ (ISGQR)	12.0	2.8	2500
$E1^{(1)}$ (IVGDR)	15.0	4.4	43
$E2^{(1)}$ (IVGQR)	25.0	6.5	2100

Fig. 5.1 shows the excitation spectrum in the giant resonances region for the ^{140}Ce. The presented spectrum is measured at 16.3° scattering angle. The excitation of the giant resonances is reflected by the bump that is clearly visible in the spectrum. It has been fitted with a Gaussian to show that the centroid energy measured in the experiment was 12.9 MeV and the width was 6.2 MeV (panel a). This is a bit higher than expected for the isoscalar quadrupole resonance (ISGQR) (see Table 5.1). This is probably due to the fact that the ISGQR is not the only giant resonance to be populated in the reaction and the peak in Fig. 5.1 would be the result of the partial superposition of more than one resonance. Indeed, panel (b) of the Fig. 5.1 shows the spectrum with marked the ISGQR and the IVGDR obtained using the results from electron scattering experiment [Pit79] with intensities fitted to the experimental data.

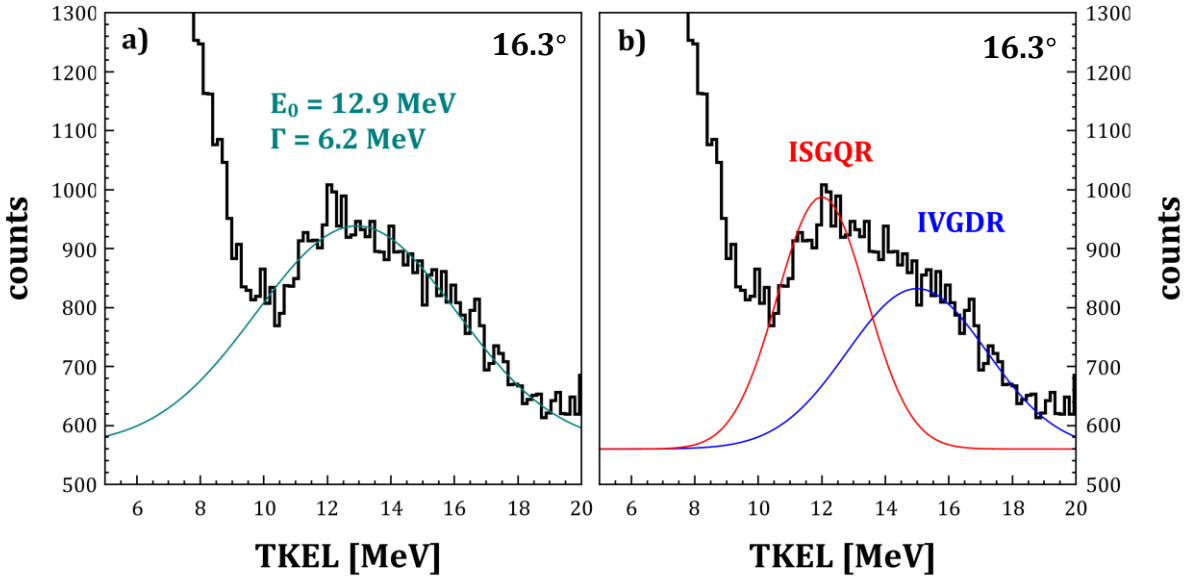

Figure 5.1: *Energy spectra of scattered ^{17}O ions measured for ^{140}Ce target. Green line (panel a) corresponds to simple Gaussian fit. The red marked peak (panel b) is due to the population of the ISGQR and the blue (panel b) is the IVGDR measured in (e,e') experiment [Pit79].*

To get more complete picture of the observed excitation of giant resonances, the DWBA analysis was performed using the deformed optical model in order to calculate the differential cross sections for excitation of different resonances. In calculations, the parameters of the optical potential (further discussed in sec. 5.4) and reduced transition probabilities (see Table 5.1) were used. Differential cross sections as a function of scattering angle presented in Fig. 5.2 show very well how excitation of different resonances is related to the angle of detection. In the case of this experiment, the Si detectors were sensitive to the angular interval from 12.4° to 20.2°, which is indicated in the figure as white area.

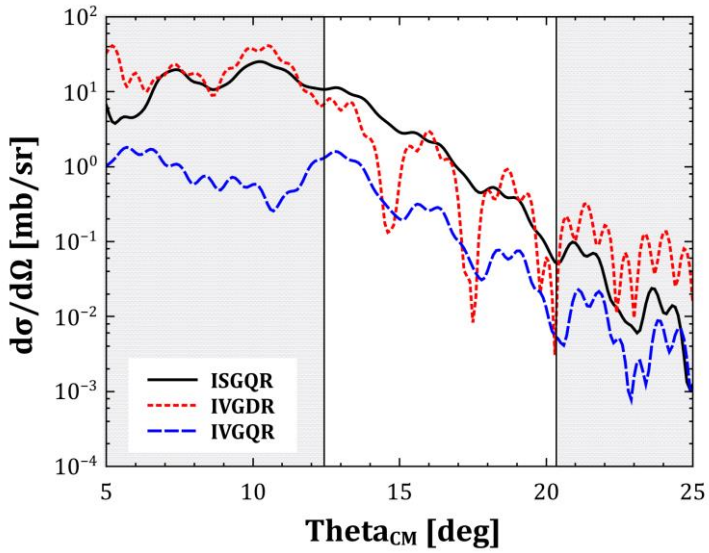

Figure 5.2: *Calculated differential cross sections for excitation of ISGQR, IVGDR and IVGQR using the parameters shown in Table 5.1. The angular interval covered by Si detectors in this experiment is indicated with white area.*

In order to compare the predictions with experimental data, the differential cross sections for the same angle (16.3°) for the excitation of different GR are shown in Table 5.2 as well as their relative content. Rough estimation of the experimental differential cross section related to the peaks fitted in Fig. 5.1 as a peaks area resulted in relative content of 56% for ISGQR and 44% for GDR. It can be seen that the data agree very well with the predictions.

Table 5.2: *Calculated differential cross sections for excitation of a different giant resonances (multipolarity λ and isospin T quantum numbers) observed in ^{140}Ce using data from (e,e') reaction [Pit79], as well as their relative content. The cross sections are integrated in the angular interval covered by Si detectors.*

$E\lambda^{(T)}$	dσ/dΩ [mb/sr] @16.3°	Relative content [%]
$E2^{(0)}$	2.0	54
$E1^{(1)}$	1.7	46

It would be desirable to observe the decay of the GRs through emission of γ rays. Such data would be well appreciated especially on ISGQR, which is still not much studied. As it was discussed in sec. 1.2.3, the probability of the GR decay through photon emission related to the particle emission is only of the order of 10^{-3}. Unfortunately, even nine large volume $LaBr_3$

detectors were not efficient enough to measure such decay. The rest of the chapter will focus on the study of the low-lying dipole states, below the GR, which are the main subject of the thesis.

5.2. DECAY OF THE LOW-LYING DIPOLE STATES

In order to observe the decay of the low-lying dipole states, the gate on time coincidence peak was applied, ^{17}O channel was selected and only ground state decays where chosen by applying the gate on ^{17}O-γ matrix. Finally, the remaining background subtraction was applied as described in sec. 4.7. Obtained spectra are shown in Fig. 5.3 for the AGATA (top panel) and HECTOR+ array (bottom panel). They are compared with the previous results from (γ,γ') and (α,α'γ) experiments. The γ-transitions that were observed in both experiments are depicted with purple lines while green lines indicates the transitions that were observed only in (γ,γ') measurement.

As discussed in sec. 1.1, the first 1^- state is expected to have two-phonon ($2^+ \otimes 3^-$) character. This issue will be addressed in the next section (5.2.1). The γ-decays from the rest of 1^- states, which are considered to originate from pygmy dipole resonance, will be discussed in sec. 5.2.2.

5.2.1. Two-Phonon 1^- State

As discussed in sec. 1.1, the strong peak at the energy of 3643 keV as seen at the top panel of Fig. 5.3 is identified as a candidate for the two-phonon $2^+ \otimes 3^-$ state. Fig. 5.4 shows the 1^- state together with the 2^+ and 3^- phonon states, all marked with blue arrows. The values of B(*E2*; $2^+ \longrightarrow 0^+$) = 13.8 W.u. and B(*E3*; $3^- \longrightarrow 0^+$) = 27 W.u. [Kim77] are characteristic for the collective phonon vibrations. Furthermore, the sum energy of the 2^+ and 3^- phonon states is within 10% equal to the energy of the 1^- state and seems to be an indication of rather non-harmonic coupling (see discussion in sec. 1.1).
The strong evidence of the pure harmonic vibration coupling would be the observation of the decay of this 1^- state into 2^+ and 3^- constituents that were not yet observed:

- 2047 keV: 1^-@3643 $\longrightarrow 2^+$@1596
- 1179 keV: 1^-@3643 $\longrightarrow 3^-$@2464.

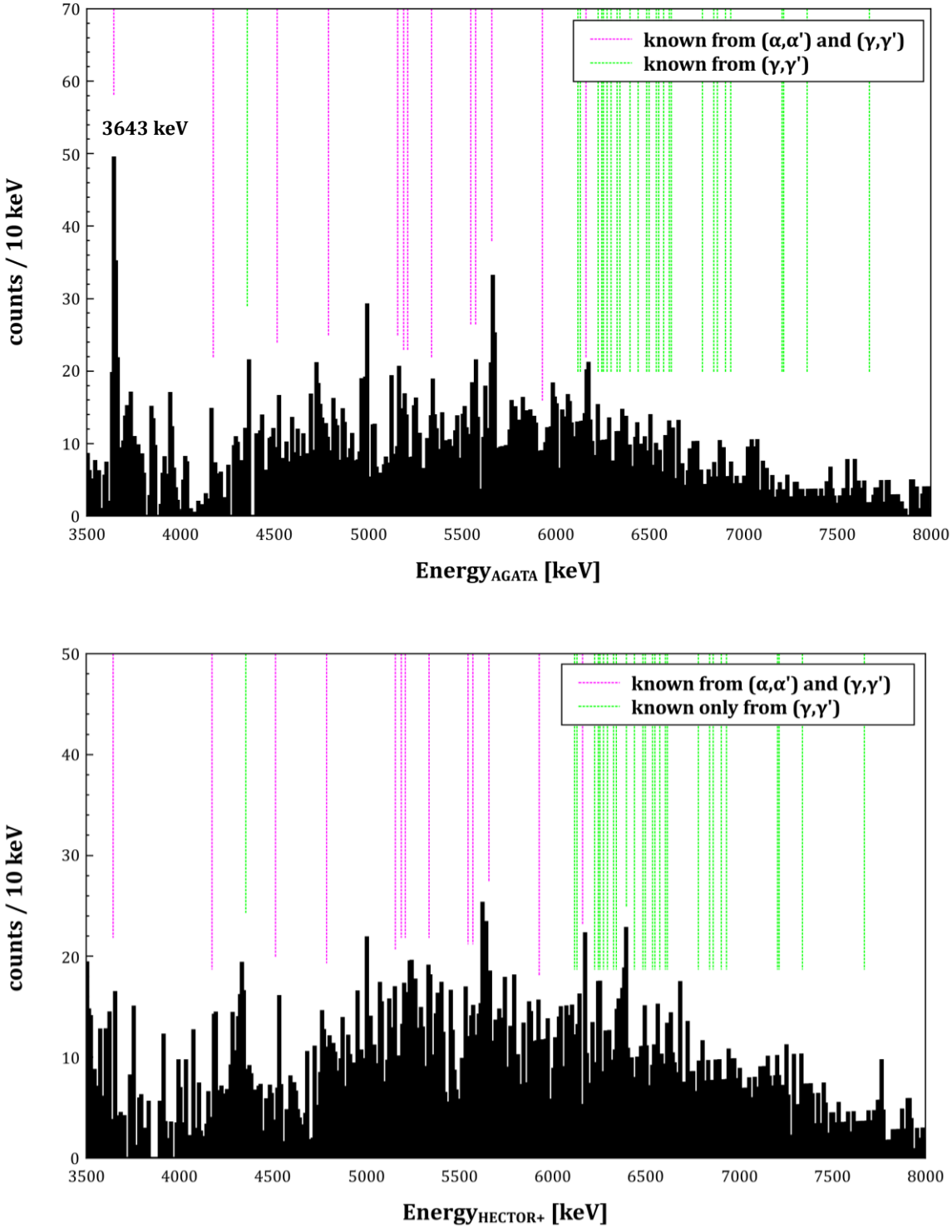

Figure 5.3: *γ-rays energy spectra in the pygmy energy region measured with AGATA (top panel) and HECTOR+ (bottom panel). Gate on time coincidence peak, selection of the ^{17}O channel and ground state decays where applied. Comparison with α scattering (purple lines) [End09] and γ scattering [Vol06] (purple and green lines) is presented.*

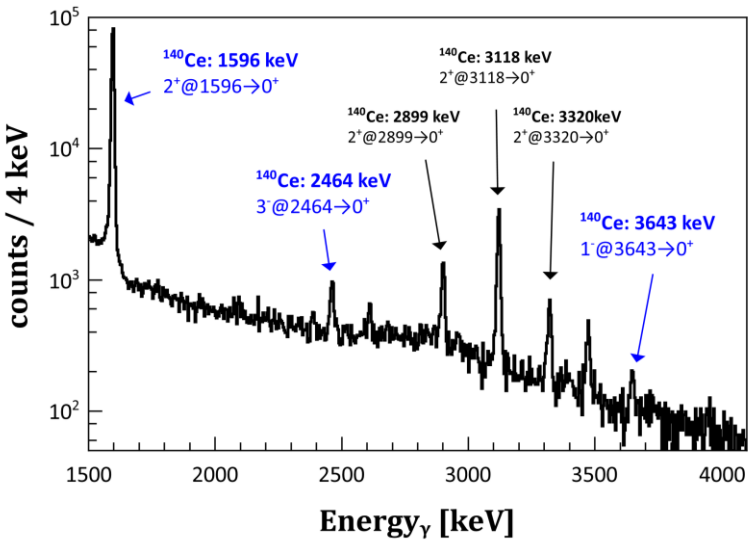

Figure 5.4: *γ-rays energy spectrum measured with AGATA in coincidence with ^{17}O inelastic scattering and ground state decays selected. Transition at 3643 keV is the candidate for the decay of two-phonon state. Transitions at 1596 and 2464 keV are the decays of one-phonon 2^+ and 3^- states, respectively.*

In order to observe the desired decay branch, it was possible to construct the γ-γ coincidence matrix of γ-rays detected in AGATA. Such matrix is shown in Fig. 5.5. In order to produce the spectrum corresponding to coincidence with particular γ transition, the gate on this transition was set as it is shown with red lines. In this case, it was chosen to observe the γ rays in coincidence with the 2^+ state at 1596 keV because it is much more intense than the 3^- state at 2464 keV.

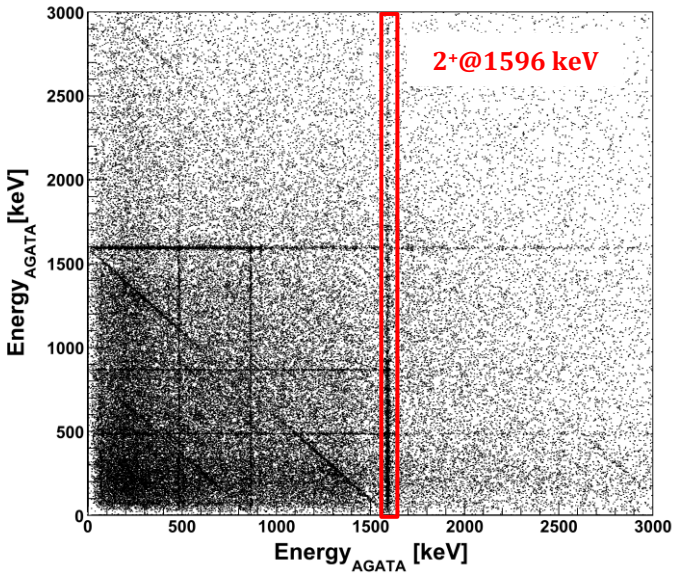

Figure 5.5: *Gamma-gamma coincidence matrix.*

Such coincidence spectrum after background reduction is shown for a different energy ranges in Fig. 5.6. Several transitions to the 2^+ state can be seen. The possible decay at 2047 keV from 1^- state to 2^+ phonon state is marked in blue. One can see that for this energy, there is a peak-like structure but it is not statistically significant. Theory predicts that the branching ratio for this γ-transition should be 0.45% [Gri94]. In this case the measurement of such branching is below the sensitivity limit so we can't exclude the existence of the pure harmonic coupling of the two-phonons. Apart from the possible harmonic coupling of the two phonons, one can clearly see the γ transition at 867 keV: $3^-\rightarrow 2^+$, which supports the assumption of a two-phonon coupling state. The nature of the two-phonon state will be also studied with the DWBA analysis later in the thesis (sec. 5.4.4). The analysis revealed also another transition at 1522 keV (marked in red), which corresponds to the energy difference between 2^+ state at 3118 keV and 2^+ state at 1596 keV. This transition is not related to the two-phonon issue, however, it was not observed before for this nucleus.

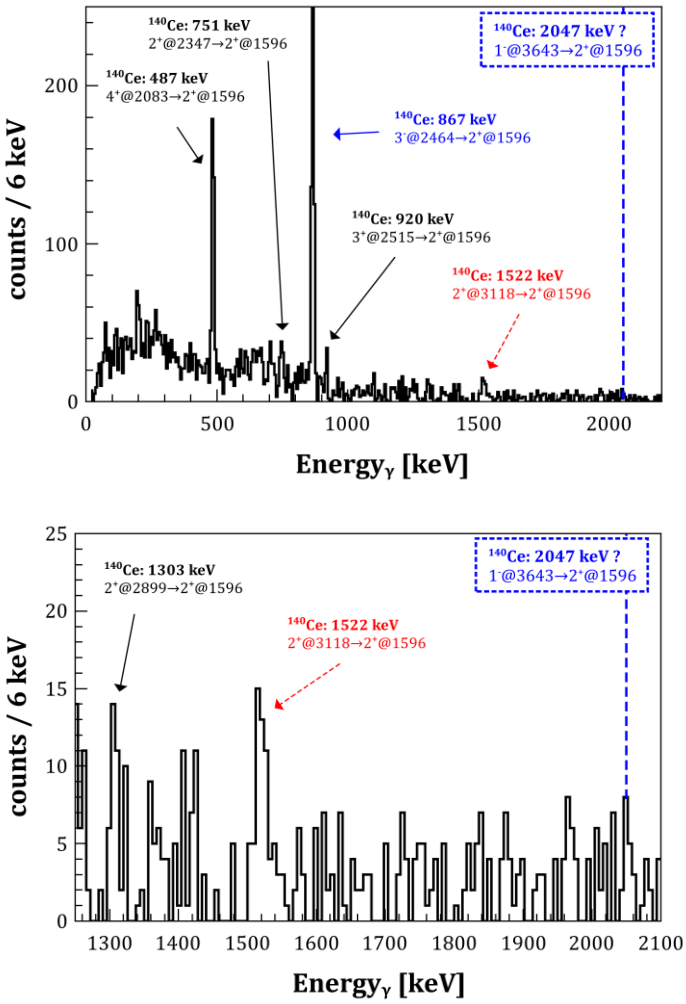

Figure 5.6: *Top panel: γ-ray energy spectrum measured in with AGATA coincidence with the transition at 1596 keV. Bottom panel: The same spectrum in energy range 1200-2100 keV. The expected energy of γ ray at 2047 keV is marked. Taken from Ref. [Krz2016b].*

5.2.2. Pygmy Dipole Resonance

The spectrum of γ rays energy in the PDR region measured with AGATA is presented in top panel of Fig. 5.3. It can be observed that ^{17}O probe excites mostly the low-energy part of the pygmy states. As compared to alpha scattering, almost the same states are observed except the one at the energy of 5929 keV, which seems not to be populated. On the other hand, one state which was not populated with alphas but seen in NRF experiment is also present in (^{17}O,^{17}O'γ) spectrum at 4355 keV. Due to a limited statistics, it was not possible to distinguish between the two states at 5157 and 5190 keV, and another two at 5548 and 55734 keV. Thus, each couple was treated as one peak in further analysis. Small fraction of the high-energy part of pygmy states seems to be also populated, but with limited statistics it is not possible to identify the single peaks. An intense peak at around 5 MeV might be a "background" γ-transition of 4979 keV with unclear spin and parity of 2^+ or 3^-. This will be further investigated in next chapter by the analysis of multipolarity.

Bottom panel of Fig. 5.3 presents the analogous spectrum measured with HECTOR+ array, using the same gating conditions. The overall picture is similar to what is observed with AGATA. The peak at 4355 keV is also present which confirms the excitation of this state with ^{17}O. Furthermore, the peak at 5929 keV seems to be below sensitivity limit also in this case. Due to different properties of $LaBr_3$ as compare to HPGe detectors of AGATA, one should expect their better efficiency in the region of higher energies. Indeed, in spectrum obtained with HECTOR+, it seems possible to observe stronger excitation of high-energy part of the PDR transitions.

5.3. ANALYSIS OF MULTIPOLARITY

Spins of excited states formed in nuclear reactions are generally oriented with respect to the direction of the projectiles. The degree of orientation depends on the formation process, which is related to the reaction mechanism [Mor77]. For the purpose of this particular experiment, which is a subject of this thesis, the expected theoretical angular distributions for the dipole (E1) and quadrupole (E2) γ-transitions were calculated. Calculations were performed using ADPCO code, which is based on formulas from Ref. [Ste75].

Taking profit from the position sensitivity of AGATA and silicon detectors, angular distributions of γ-rays emitted from ^{140}Ce nucleus were determined. The angle between beam direction and recoiling nucleus velocity vector was obtained at the base of a measurement of the scattered beam nuclei, according to the same procedure as for the Doppler correction (see sec. 4.5). The obtained distributions of the of γ rays with respect to the angles between emitted γ-rays and the recoiling nucleus velocity vector were then divided by the angle dependant efficiency of AGATA detectors which was simulated using Geant4 code (see Fig. 5.7).

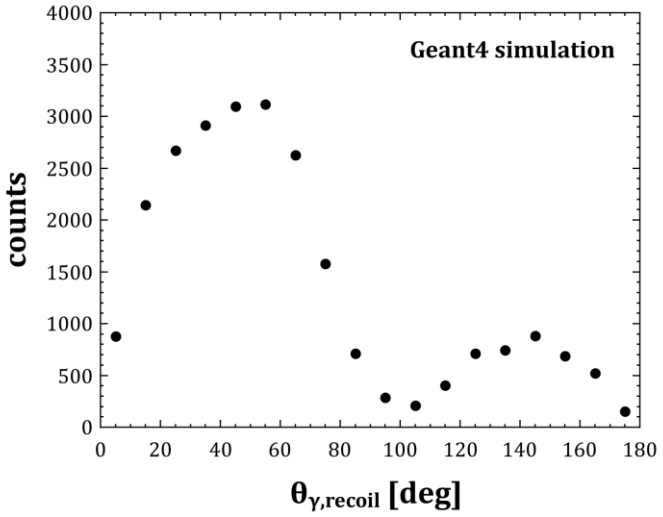

Figure 5.7: *AGATA efficiency with respect to the angle of detection simulated with GEANT4.*

5.3.1. Angular Distributions

As a first step of the analysis, ground-state transition at 1596 keV from first excited 2^+ state, as being the most intensive, was chosen to evaluate whether the applied technique is sensitive to multipolarity. The measured yield with respect to the angle between emitted γ-rays and recoiling target nucleus was normalized for the AGATA efficiency (see Fig. 5.7). The obtained angular distribution is shown in Fig. 5.8 and compared to the expected trend. Good agreement confirms the expected quadrupole character of this transition. One can note, the data points at angles larger than 90^0 are rather scattered and that the low statistics of these points does not fully explain this behaviour. Indeed, one cannot exclude other effects such as for example more complicated reaction mechanisms showing up at these large angles, or some extra inefficiencies of Si pads at these angles not entirely accounted for in the computed error bars. As mentioned in sec. 4.3.1, this also suggests a not perfect symmetry of the Si detectors along the beam axis. On the other hand, this may also be due to the fact that ^{140}Ce measurement was performed at the end of experiment, thus the properties of Si detectors might had been slightly changed due to radiation damages. Therefore the angular distribution data between 90° and 180° were disregarded in the following analyses.

The same procedure was applied to the γ transition at E_γ = 868 keV ($3^- \rightarrow 2^+$) which is an E1 transition. The Fig. 5.8 (top panel) shows the angular distribution for this transition and good agreement with the expected theoretical trend is observed.

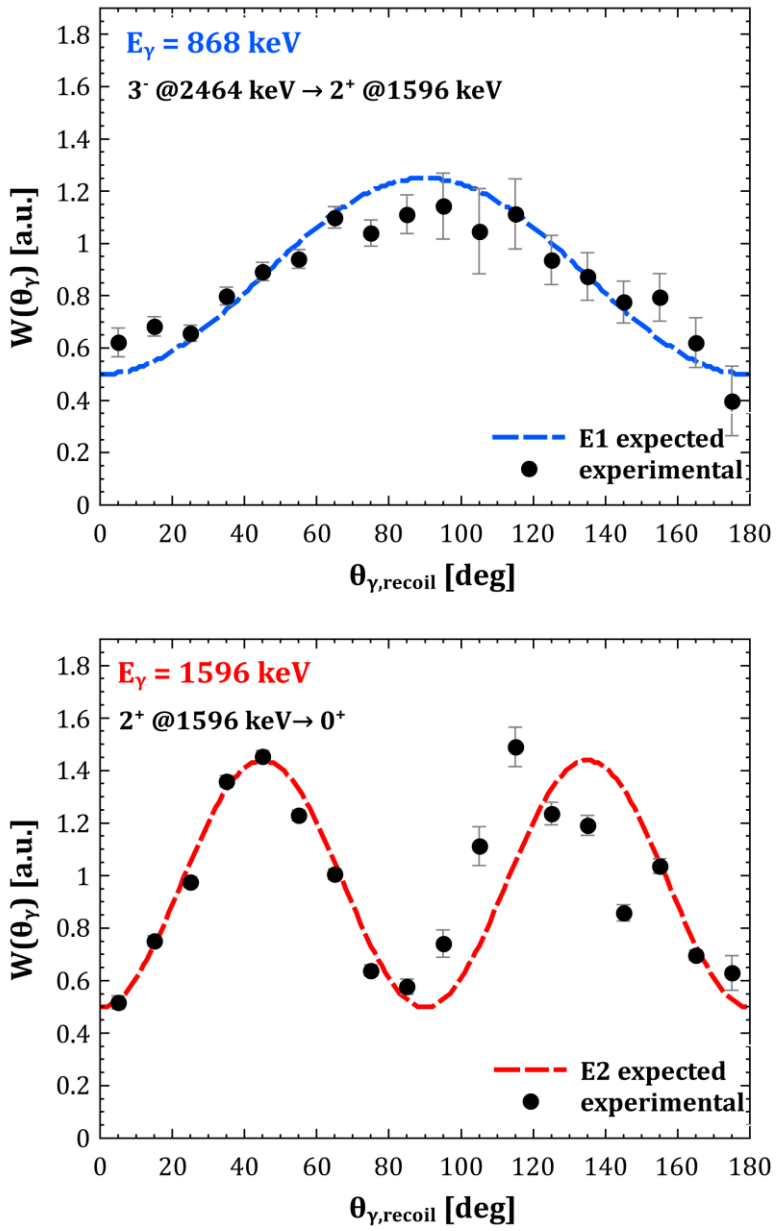

Figure 5.8: *Angular distributions of γ-rays emitted from ^{140}Ce nucleus. Top panel: dipole (E1) γ-transition (868 keV: $3^- \rightarrow 2^+$) as well as expected trend (blue line); Bottom panel: quadrupole (E2) γ-transition (1596 keV: $2^+ \rightarrow 0^+$) together with expected trend (red line).*

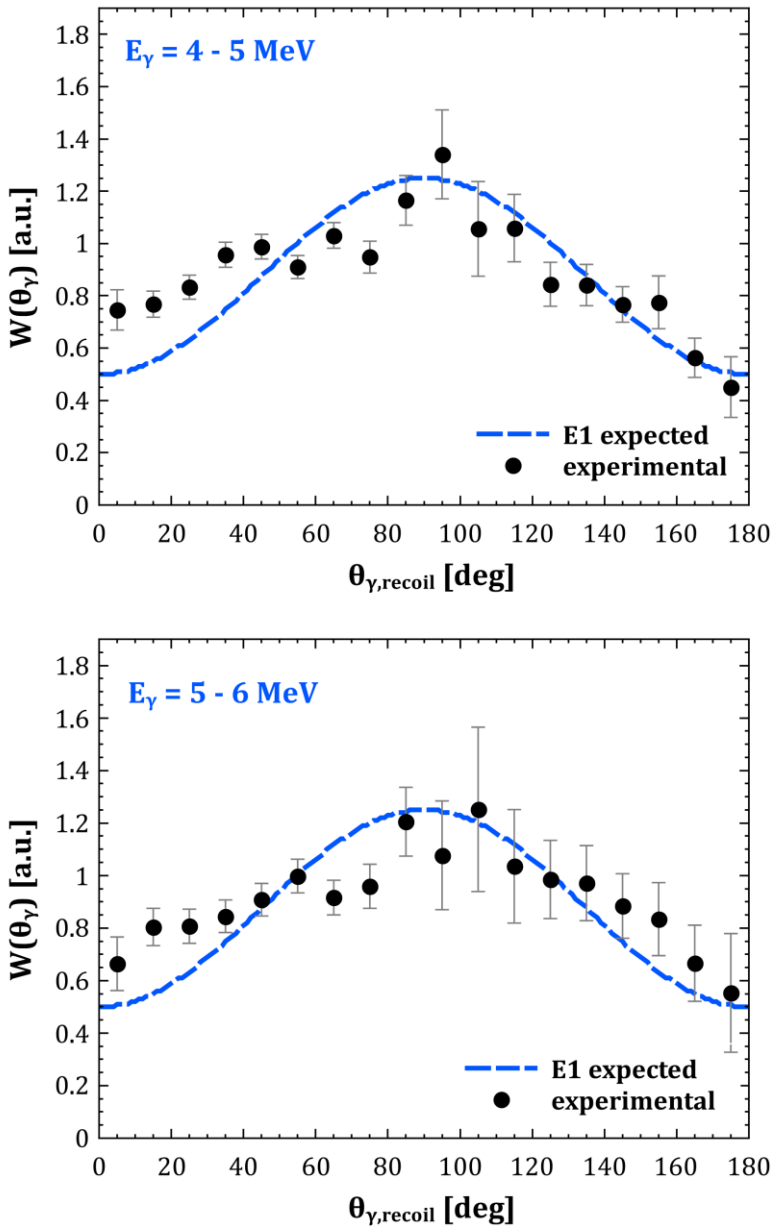

Figure 5.9: *Angular distributions of γ-rays emitted from ^{140}Ce nucleus for a different pygmy energy regions: 4-5 MeV (top panel), 5-6 MeV (bottom panel).*

After demonstrating the sensitivity of applied technique to multipolarity, the angular distribution for the pygmy energy region was also investigated. Due to low statistics, it was not possible to perform the analysis for each individual γ-transition. For this reason, the region between 4 -6 MeV, where it is expected to observe the highest concentration of pygmy dipole strength (see Table 1.1) as compared to α scattering [Sav06, End09], was divided into 1 MeV intervals. For such integrated regions, the angular distributions were obtained. As it is shown in the Fig. 5.9 for the energies between 4 - 5 MeV (top panel) and 5 - 6 MeV (bottom panel), there is a good agreement with the theoretical calculations confirming the dominantly dipole character of the γ-transitions in this energy region. In both distributions some fraction of *E2* transitions is observed giving a rise on the left and right parts of the distributions.

5.3.2. Dipole vs Quadrupole γ-transitions

The calculated angular distributions for the E1 and E2 γ-transitions are shown in Fig. 5.10. The angular interval from 15° to 65° in which mostly quadrupole transitions are expected is depicted in red. The angular interval from 65° to 115° which is highlighted in blue corresponds to the predominance of dipole γ-transitions. In order to investigate quantitatively the composition of *E1* and *E2* γ-transitions in the pygmy energy region, different angular ranges were selected as it is shown in Fig. 5.10. Such gating allowed to obtain two kinds of γ-rays energy spectra (see Fig. 5.11) related to this two angular ranges. The spectra were normalized so that for each spectrum the intensity of the first excited 2^+ state (E_γ = 1596 keV) was the same.

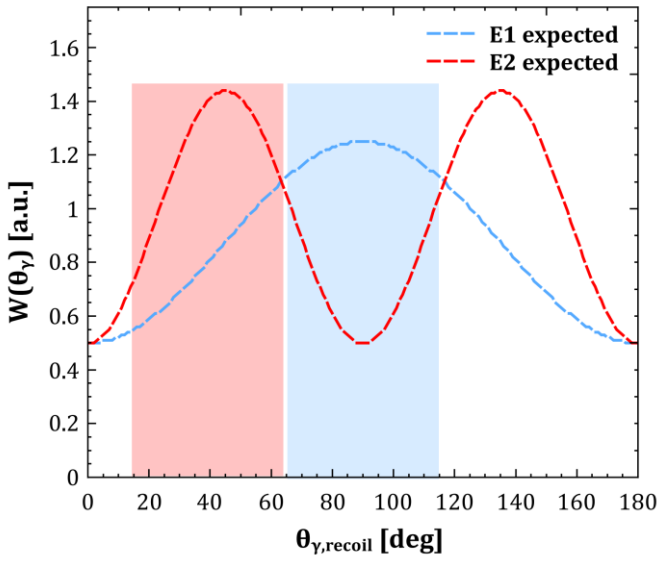

Figure 5.10: *Expected angular distributions of γ-rays for E1 (blue line) and E2 (red line) γ transitions. Angular intervals in which E1 or E2 γ transitions dominate are marked.*

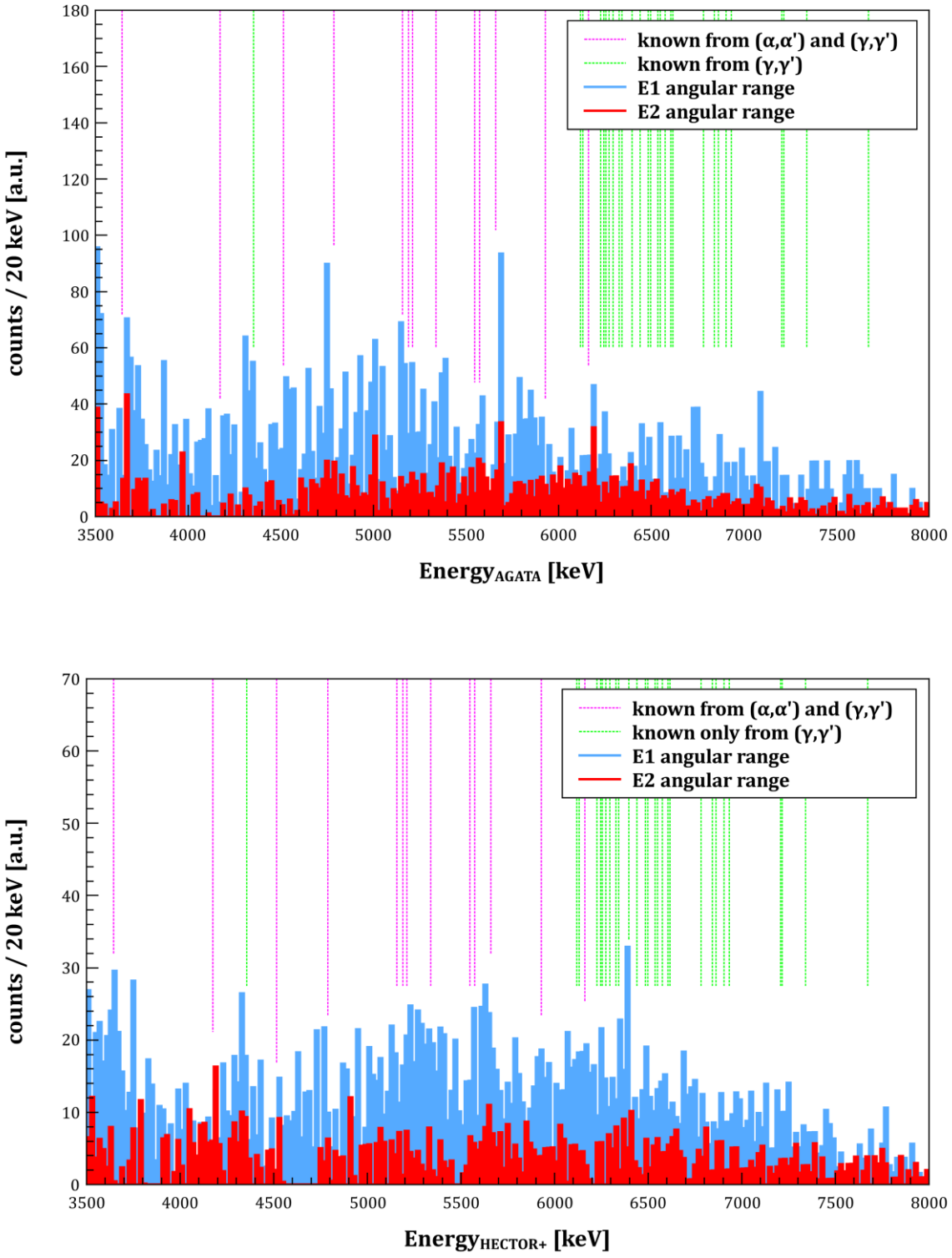

Figure 5.11: *γ-rays energy spectra measured with AGATA (top panel) and HECTOR+ (bottom panel) in the pygmy energy region. Blue spectrum is gated on 65°-11° angular range in order to enhance the E1 transitions. Red spectrum is gated on 0-65° angular range in order to enhance the E2 transitions.*

As it was postulated, *E1* type γ-transitions clearly dominate over *E2* type of excitations in the studied energy region. Additionally, it seems that the previously seen intense structure around 5 MeV is very much supressed in "*E1* like" spectrum which suggests its *E2* character. However with very limited statistics in is not possible to distinguish whether the state has *E2* or *E3* character.

In order to evaluate the *E1* excitations content in the pygmy energy region in quantitative way, the ratio of the intensity in the spectra associated to the angular ranges that are presented in Fig. 5.10 was evaluated for different energy intervals. First interval from 3.5-4 MeV in which first 1^- state is expected and then for the intervals of 1 MeV from 4 to 8 MeV, which should contain the PDR excitations. The results are shown in Fig. 5.12 together with the expected ratios for the pure *E1* and *E2* transitions and two known γ-transitions at 868 keV ($3^- \longrightarrow 2^+$) and 1596 keV ($2^+ \longrightarrow 0^+$). It is clearly seen for the whole PDR region that E1 transition dominates. The ratio is lower for the 3.5 – 4 MeV energy interval because of presence of the state at 3653 keV, which is postulated to be 2^+ or 3^- state [Wur69]. However, because of low statistics, it is not possible to evaluate the angular distribution for single state.

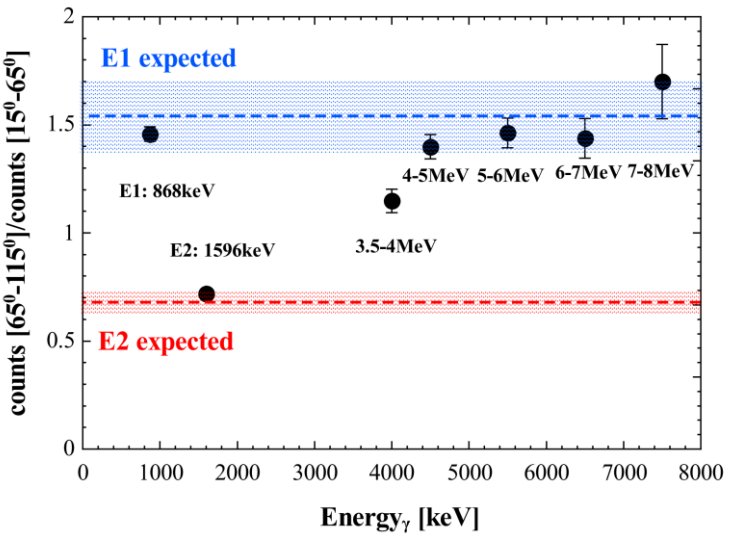

Figure 5.12: *The ratio of the γ-rays energy spectra intensity measured in different energy intervals with AGATA for the different angular intervals corresponding to the E1 and E2 transitions. The values obtained for transitions at 868 and 1596 keV are also shown. The blue and the red regions are the ratios predicted for the pure E1 and E2 γ-transitions.*

5.4. DIFFERENTIAL CROSS-SECTIONS

In order to describe the excited states, a Distorted Wave Born Approximation (DWBA) analysis was performed to obtain the theoretical estimation of differential cross sections at different scattering angles. The DWBA calculations were performed using the computer code FRESCO [Tho88]. Details on the code including the input description are given in Appendix B.

Calculations were then compared to obtained experimental results. The differential cross sections were estimated as follows:

$$\frac{d^2\sigma}{dEd\Omega} = \frac{N_\gamma(E)}{\epsilon(E)N_{beam}N_{target}d\Omega} \tag{5.1}$$

where N_γ is the number of γ-rays measured at the energy E, ε(E) is the absolute efficiency of the γ-rays detection system at the energy E, dΩ is the solid angle of the TRACE pads, N_{target} is the number of target nuclei per surface unit and N_{beam} is the number of beam nuclei that passed through the target during experiment.

The uncertainties of the experimental cross sections included uncertainties due to statistics, the angular correlations (10%) and the AGATA array efficiency (10%).

Cross sections analysis began with the comparison between experimental results and DWBA for elastic scattering, which gave necessary normalization. Then, the validation of the applied method was done for known 2^+ and 3^- ground state decays. Finally, main part of the analysis was devoted to 1^- states.

5.4.1. Elastic Scattering

First step of the analysis was to evaluate the experimental cross sections for the elastic scattering with respect to the scattering angle. This was possible because the scaled down "singles" spectra of the scattered heavy-ions, without coincidence with γ-rays emission, were also measured, which gave an information on the elastic scattering (for the technical details see sec. 3.4 and for the time spectra see sec. 4.2.1). The differential cross sections were evaluated at the base of the number of counts in the peaks corresponding to the elastic events (see example in Fig. 4.8). The experimental data were then compared with the DWBA calculations using FRESCO code. The optical parameters of the Woods-Saxon potentials that were applied for all DWBA calculations using FRESCO code are presented in Table 5.3. They were obtained according to the procedure presented in sec. 2.2.1. The experimentally obtained data were then normalized to the calculations obtained with the FRESCO. This normalization was necessary in order to take into account the numbers of beam and target nuclei denoted as N_{beam} and N_{target} in eq. 5.1, which was not possible to obtain from the measurement.

Table 5.3: *Parameters of the Woods-Saxon potential used in the DWBA analysis for ^{140}Ce.*

Nucleus	**V** [MeV]	**R_v** [MeV]	**r_c** [fm]	**a_v** [fm]	**W** [MeV]	**R_w** [fm]	**a_w** [fm]
^{140}Ce	48.1	1.153	1.2	0.669	34.1	1.153	0.669

V, W – depth of the real and imaginary potential
R_v, Rw – radii of the real and imaginary potential
a_v, a_w – diffuseness of the real and imaginary potential
r_c – Coulomb radius parameter

Fig. 5.13 shows the data obtained for the elastic scattering divided by the Rutherford cross-section after normalization. This normalization was then applied in the analysis of the cross sections for inelastic excitation of different states that will be shown in next sections. The results show a characteristic behaviour of the elastic scattering. It is close to the Rutherford type up to certain angle, which is called grazing. Then the cross section drops which is due to nuclear component of the interaction. Good agreement between data and the model calculation is observed.

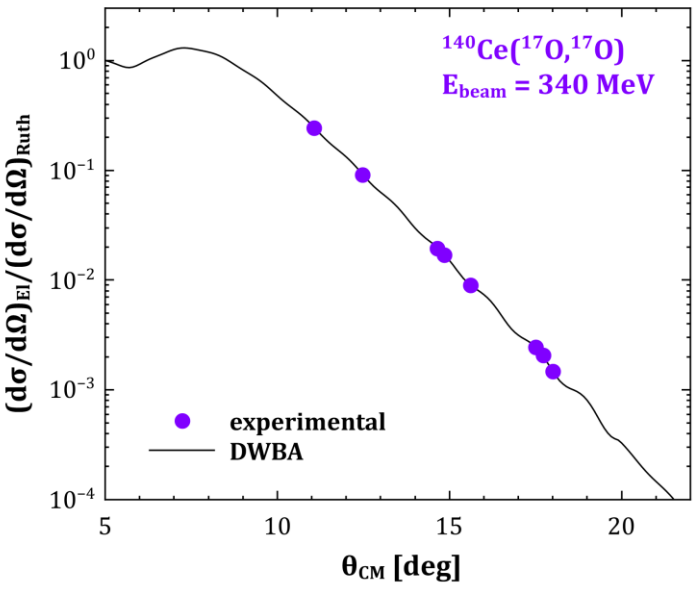

Figure 5.13: *Experimental differential cross section (filled circles) and DWBA calculation (solid curve) for the elastic scattering of ^{17}O on ^{140}Ce at E_{beam} = 340 MeV at different scattering angles. Elastic scattering differential cross section is divided by the Rutherford cross section.*

5.4.2. Quadrupole (2^+) States

In order to determine the differential cross sections for the inelastic excitations (see Eq. 5.1), the number of emitted γ-rays was evaluated from energy spectrum measured with AGATA. To check the reliability and the accuracy of DWBA calculations, a comparison between the experimental and the calculated cross sections for different $J^\pi = 2^+$ excited states were evaluated. The values of $B(E2; 0^+ \rightarrow 2^+)$ = 13.8 W.u. for 1596 keV and $B(E2; 0^+ \rightarrow 2^+)$ = 1.255 W.u. for 3118 keV [Kim77] state were used.

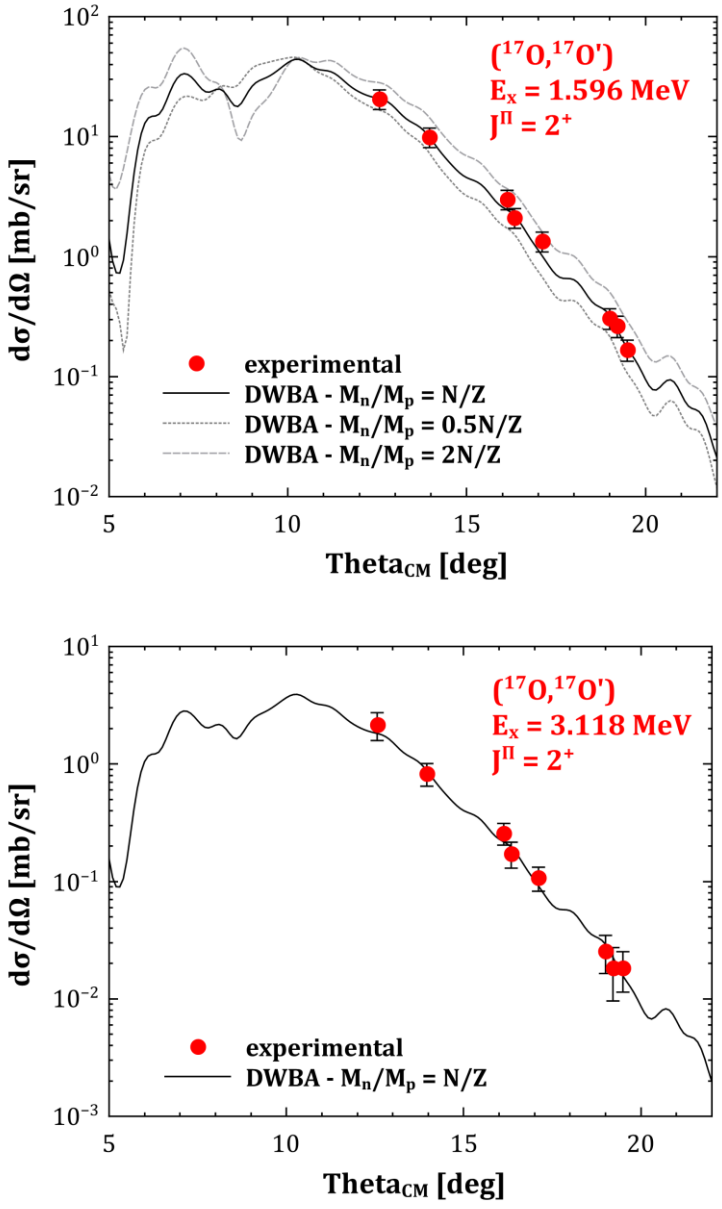

Figure 5.14: *Experimental differential cross sections (filled circles) and DWBA calculation (solid curves) for the inelastic scattering of ^{17}O on ^{140}Ce at E_{beam} = 340 MeV at different scattering angles. Cross sections for the 2^+ excited states at 1.596 MeV (top panel) and 3.118 MeV (bottom panel) are shown. The uncertainties of experimental cross sections are reported with the error bars.*

As a first verification of the FRESCO calculations, the cross sections for the first 2^+ state have been evaluated with different values of neutron and proton matrix elements M_n/M_p which is an indication of isospin character of excitation when using the deformed optical model as it was discussed in Ref. [Hor91]. It was also discussed in sec. 2.2.3 when calculating the form factor with double-folding method, that for the $M_n/M_p = N/Z$ the isovector part of the form factor vanishes [Sat83]. As one can observe from Fig. 5.14 (top panel), the best agreement with the experimental data is achieved for the value of $M_n/M_p = N/Z$ which refers to a pure isoscalar nature of this state. It is clear that calculations are sensitive to the value of M_n/M_p, thus for the other 2^+ states the FRESCO calculations have been performed with the value $M_n/M_p = N/Z$ according to the nature of these states. Good agreement between experimental values and DWBA calculations is then also demonstrated for another 2^+ state at 3118 keV (Fig. 5.14, bottom panel). This allows to conclude that the deformed optical model very well describes the studied 2^+ states and the parameters of the model are well-defined.

5.4.3. Octupole (3^-) State

As it was demonstrated in the previous section, the applied model was able to describe well the excitation of the 2^+ states decaying to the ground state. It is also interesting to investigate the excitation cross-sections of states with different angular momentum and more complicated decay pattern.

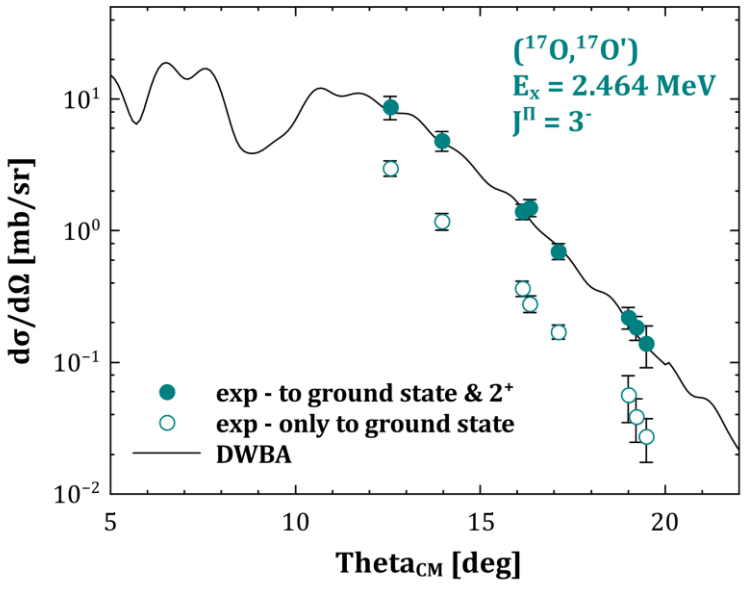

Figure 5.15: *Experimental differential cross sections (filled and empty circles) and DWBA calculation (solid curve) for the inelastic scattering of ^{17}O on ^{140}Ce at E_{beam} = 340 MeV at different scattering angles. Experimental cross sections for the 3^- excited states at 2.464 MeV taking into account only ground state decay are shown with empty circles. The values obtained for the sum of transitions to 0^+ and first excited 2^+ are presented with filled circles.*

There is a $J^{\pi} = 3^-$ state at the energy of 2464 keV. This state decays either to the ground state or to the first excited 2^+ state at 1596 keV. Therefore the total intensity should be the sum of the transitions at 2464 keV: $3^- \rightarrow 0^+$ and 868 keV: $3^- \rightarrow 2^+$. Such experimental data have been taken into account for the comparison with the theoretical predictions. For the DWBA calculations, the value of B(*E3*; $0^+ \rightarrow 3^-$) = 27 W.u. [Kim77] was used. The results of the analysis are shown in Fig. 5.15. The empty circles display the experimental cross sections when taking into account only transition to the ground state, while the filled circles show the total strength adding the transition to the first excited 2^+ state. Also in this case, a good agreement with the DWBA analysis is observed.

5.4.4. Dipole (1^-) Pygmy States

The obtained good agreement between experimental cross sections and DWBA calculations for known quadrupole and octupole γ-transitions, allowed for applying the same technique was applied to the $J^{\pi} = 1^-$ states in the PDR energy region. At first, the experimental differential cross sections for each identified $J^{\pi} = 1^-$ state have been evaluated with respect to the scattering angle. Due to very low statistics in the pygmy energy region, the analysis for the individual peaks was very difficult. In most cases, the identification of the position of the peaks was only possible by comparison to the results from previous (γ,γ') and (α,α'γ) experiments. Limited statistics did not allow to distinguish between the two states at 5157 and 5190 keV, and another two at 5548 and 5574 keV. In these cases, each couple was treated as a one peak and estimated cross sections reflects the sum of the pair. The experiemental sensitivty limit was evaluated, as a condition for the mimimum peak area [End09]:

$$A \geq \frac{1}{2p^2} + \sqrt{\frac{1}{4p^4} + \frac{2B}{p^2}} \tag{5.3}$$

where A is the mimimum peak area, B is the background and p is the relative uncertainty of the peak area, $p = \frac{\Delta A}{A}$ *that is required to be* $p \leq 0.7$.

The procedure of the background spectrum determination was presented in chapter 4.7.

The experimental differential cross sections measured using (^{17}O, ^{17}O'γ) reaction at 12.5 deg (in CM frame of reference), together with the sensitivity limit are shown in the top panel of Fig. 5.16. The values are reported in Table 5.3. The obtained differential cross sections of the ^{17}O inelastic scattering are compared with differential cross sections from (α,α'γ) [Sav06, End09] (middle panel) and the reduced transition probabilities B(*E1*) from (γ,γ') [Vol06] (bottom panel).

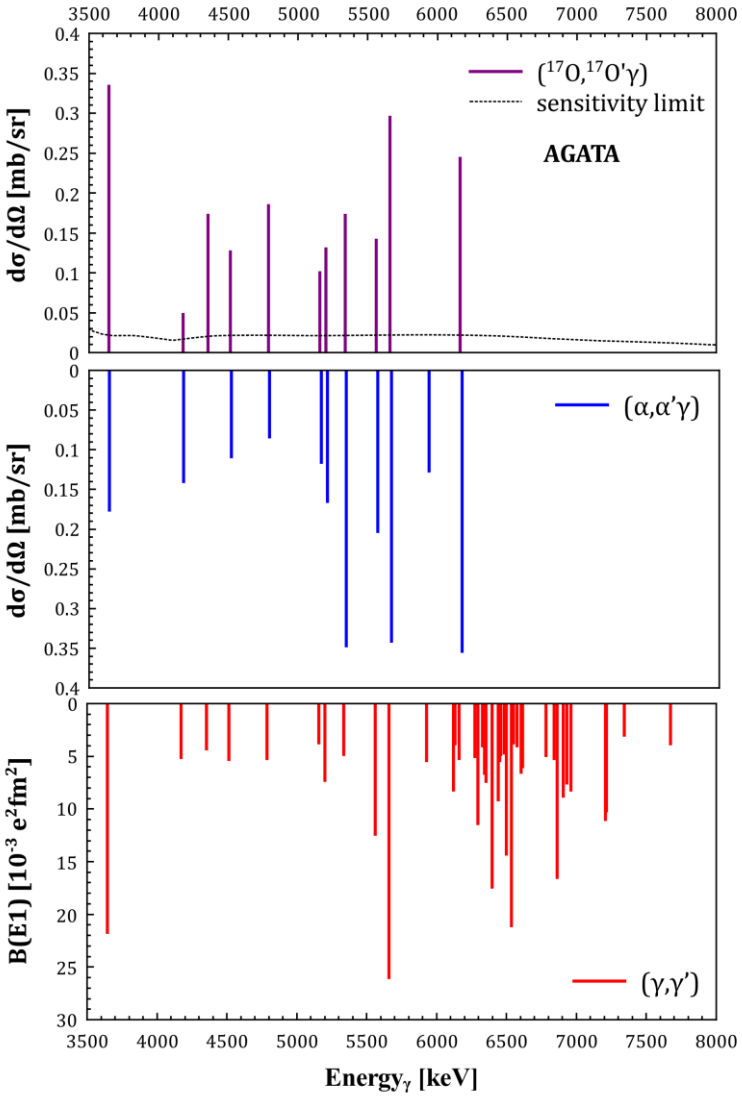

Figure 5.16: *Experimental cross sections of 1⁻ states in ^{140}Ce excited via inelastic scattering of ^{17}O (top panel) measured at 12.5 deg (in CM frame of reference) compared to the cross sections measured in (α,α'γ) [End09] (middle panel) and values of B(E1) obtained in NRF experiment [Vol06] (bottom panel).*

One can see that the results for ^{17}O scattering are similar to the ones obtained using α scattering. This supports the interpretation of isospin mixing of the pygmy dipole states that relies on the fact that isoscalar probe excites predominantly the lower-lying PDR states, as compared to photons. Some differences are also present indicating that heavy-ions and α particles probe in a bit different way the transition densities associated to the PDR states. This justify how important is to use heavy-ions to study the PDR states which have a very complicated transition densities.

In order to investigate the character of the dipole states, the experimentally obtained differential cross sections were compared with the DWBA calculations using similar approach as before with

deformed optical model. The first step was to study the character of the first dipole state at 3643 keV, which is expected to be a two-phonon state. This analysis was also performed for the state at 5660 keV which is supposed to have a pygmy dipole nature and having the largest value of B(E1) thus the strong isovector component (see bottom panel of Fig. 5.16).

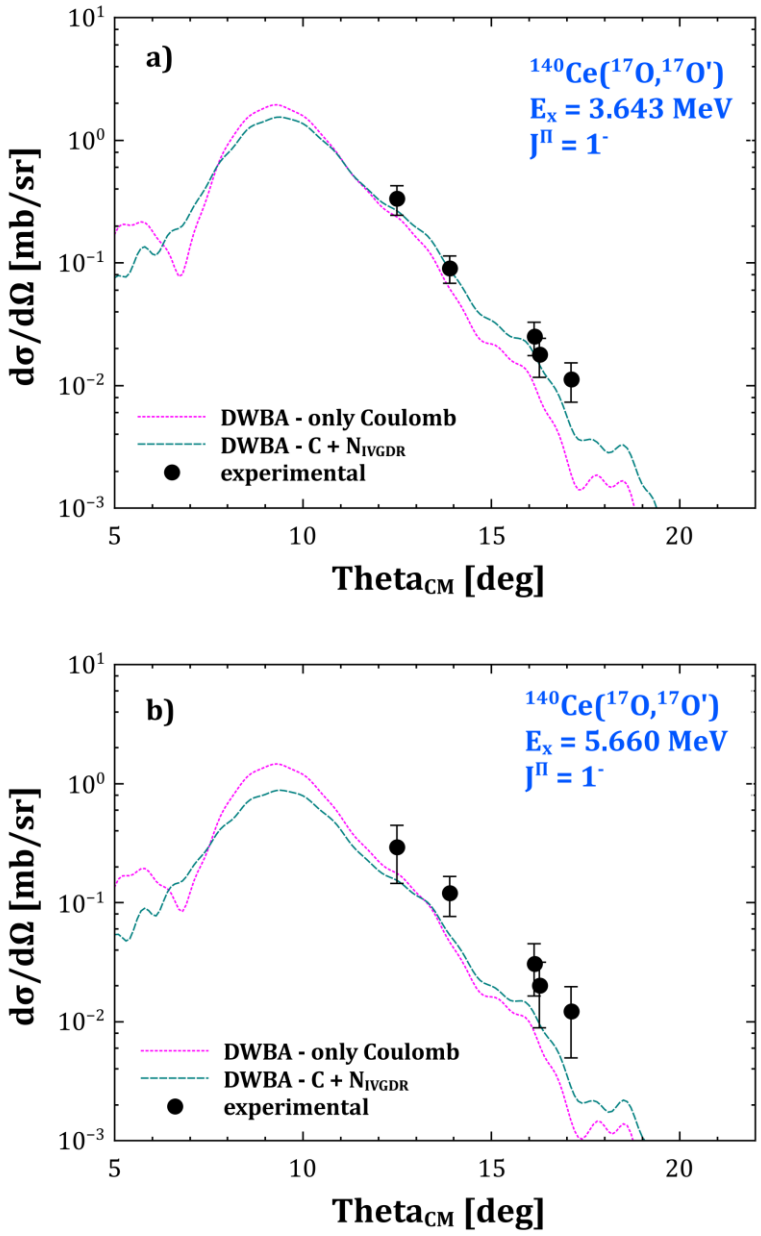

Figure 5.17: *Experimental differential cross sections for the excitation of 1¯states at 3643 keV (a) and 5660 keV (b) in ^{140}Ce measured with (^{17}O, ^{17}O'γ) reaction at different scattering angles. The dotted purple line represents the calculated Coulomb cross section with the DWBA while the dashed green line is the total cross section using the standard collective form factor.*

The comparison of the results for these two states is shown in Fig. 5.17 and suggests their different character. Indeed, the differential cross section for the excitation of the two-phonon state (panel a) is rather satisfactory described by the Coulomb interaction with a small nuclear contribution evaluated using the standard collective form factor as for the GDR. In contrast, in the case of the state at 5660 keV the nuclear contribution plays a significant role and the standard collective form factor can't reproduce the data. The conclusion from that observation was that in case of the PDR states, the different form factor is needed, which would properly take into account a nuclear part of the interaction. The discussion about the importance of different form factors for various modes of excitations like PDR, IVGDR or ISGDR was presented in sec. 2.2.3.

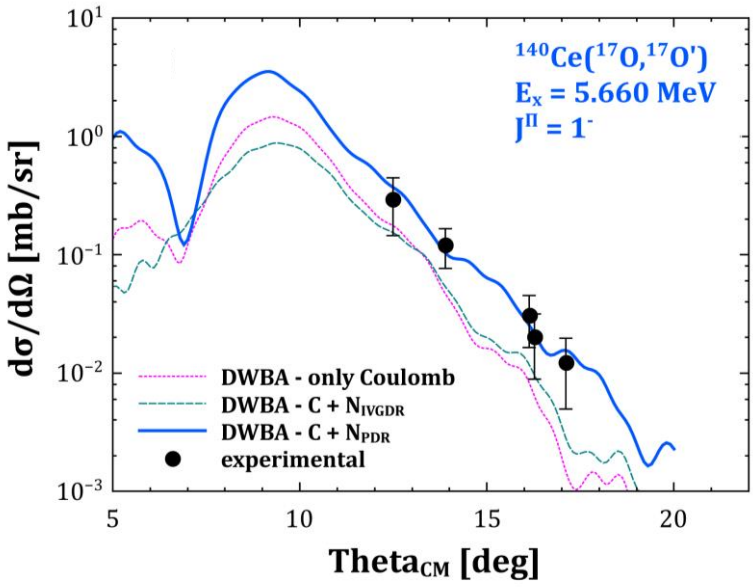

Figure 5.18: *Experimental differential cross sections for the excitation of 1$^-$ state at 5660 keV in ^{140}Ce measured with (^{17}O, ^{17}O'γ) reaction at different scattering angles. The dotted purple line represent the calculated Coulomb cross section with the DWBA while the dashed green line is the total cross section using the standard collective form factor, and solid blue line represents the total cross section using microscopically calculated form factor for the PDR states.*

As it was described in sec. 2.2.3, a microscopic form factor based on transition densities for the PDR state was derived. This form factor was calculated assuming one state at the energy of 8.39 MeV, and corresponding to 4.14% of ISEWSR. For the purpose of the procedure description, this form factor can be denoted as "initial". In order to apply this form factor to specific PDR state, it had to be scaled so that it refers to excitation of different energy and fraction of ISEWSR. As the cross section is proportional to the square root of the form factor, the scaling was performed in following way. As a first approximation, the DWBA calculation was done using the initial form factor that corresponds to known values of energy and fraction of ISEWSR. Then, different scaling factors (*SF*) were applied to the initial form factor and the DWBA calculations were

repeated until the calculated differential cross sections best fitted the experimental data. Finally, the corresponding fraction of ISEWSR was evaluated from proportion as being related to the energy of the excitation and to the cross section, which is proportional to the square root of the form factor. This can be expressed with the equation:

$$ISEWSR_i[\%] = \frac{E_i}{8.39\ MeV} \cdot SF_i^2 \cdot 4.14\% \tag{5.3}$$

where SF_i denotes the scaling of the form factor for a given excitation (i)

After applying the pygmy dipole form factor, and assuming estimated value of ISEWSR fraction, the DWBA reproduces the experimental data which is shown in Fig. 5.18 with the solid blue line for the peak at 5660 keV. The same procedure was applied to each studied pygmy dipole γ transition. This way, fraction of ISEWSR was estimated for each PDR state and the results are shown in Table 5.4. The sum for all discrete states was therefore 0.44(13)%. The strengths (S_{IS}) of PDR states were obtained using procedure described later and they are presented in Table 5.4 as well.

Table 5.4: *Experimental differential cross sections (*dσ/dΩ*) measured at 12.5 deg (in CM frame of reference) scattering angle for the population of 1^- states in ^{140}Ce excited via inelastic scattering of ^{17}O as well as the values of isoscalar energy-weighted sum rule (ISEWSR) and its strength (S_{IS}).*

Energy [keV]	**dσ/dΩ [mb/sr]**	**ISEWSR [%]**	**S_{IS} [10^2 e^2fm^6]**
4173.6	0.048(63)	0.014(19)	0.83(1.12)
4354.9	0.173(145)	0.039(32)	2.21(1.81)
4514.9	0.126(98)	0.029(22)	1.58(1.20)
4787.8	0.184(149)	0.050(40)	2.57(2.06)
5157.3	0.100(112)	0.030(34)	1.43(1.63)
5211.6 & 5190.2	0.130(111)	0.033(28)	1.56(1.33)
5337.3	0.172(137)	0.053(42)	2.45(1.94)
5548.4 & 5573.8	0.141(133)	0.038(36)	1.68(1.60)
5659.9	0.295(171)	0.075(44)	3.27(1.92)
5928.6		*not observed*	
6161.7	0.243(220)	0.076(68)	3.04(2.72)

The very important information concerning the PDR states properties is their isospin character. To study the isospin mixing of the PDR states, the additional analysis was done. At the beginning the whole PDR region was divided into low- and high-energy parts, based on the observations from (α,α'γ) and (γ,γ') experiments and confirmed by the results of ^{17}O scattering. They correspond to the 4 – 6.2 MeV and 6.2 – 7.8 MeV intervals. The integrated regions should represent the "total" cross sections, including so called the unresolved strength, which can be considered as an upper limit in this experiment. For both regions, the experimental differential cross sections have been compared with the DWBA calculations. The results are presented in Fig. 5.19. As expected, one can see that the deformed optical model (indicated with dashed green lines) does not reproduce the experimental cross section also in this case. The fraction of missing cross section is 88 and 58% for the low- and high-energy parts of the PDR states. This allows to conclude, the same as previously for the discrete states, that the excitation mechanism of PDR strongly involves the nuclear contribution. This is especially seen for the low-energy part. Different amount of missing fractions for both part of data confirms a predominantly isoscalar character of the low-energy region, while a strong mixing with isovector states in high-energy region. Analogically as it shown for the discrete state at 5660 keV (Fig. 5.18), the calculations using the microscopic form factor for PDR states allowed reproducing the experimental data.

Then, for the more accurate approximation, the whole region was divided into 200 keV intervals and the fraction of ISEWSR was estimated for each range using the same method described before. The fraction of ISEWSR for the low-energy part was 1.42(22)% and 0.61(14)% for the high-energy region, with a total of 2.03(26)% including unresolved strength. The value obtained for total strength in the integrated region can be treated as an upper limit observed in this experiment.

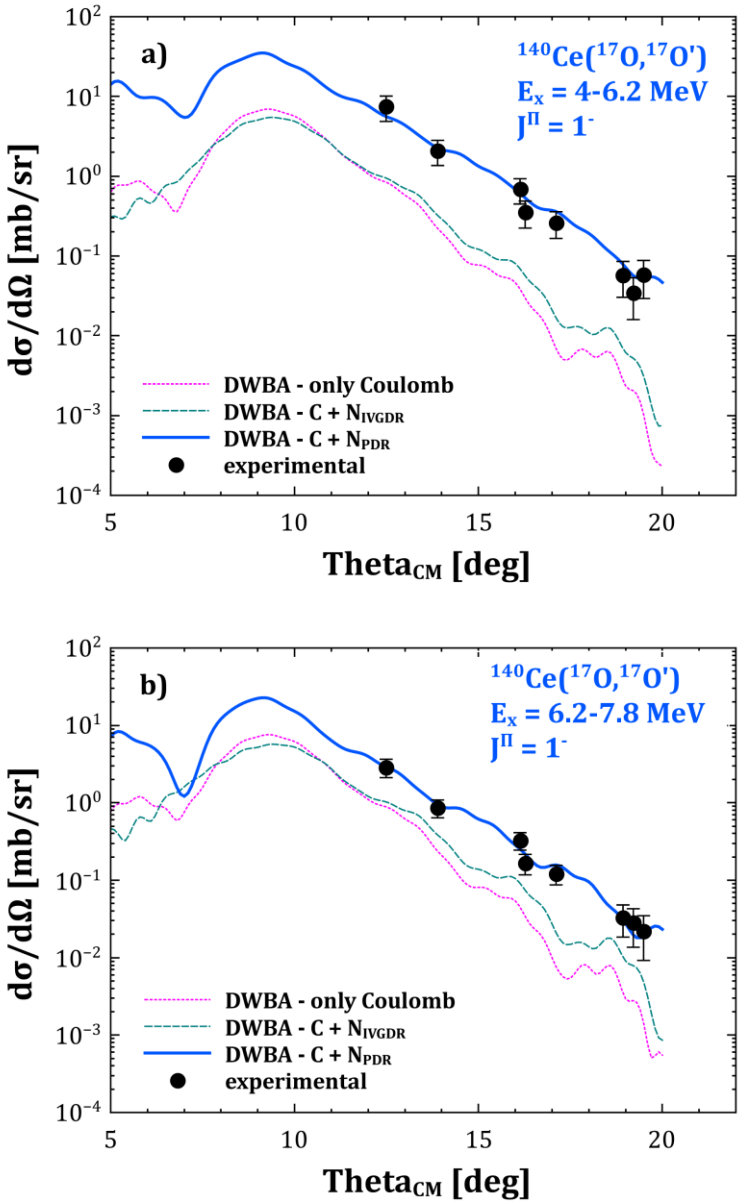

Figure 5.19: *Experimental differential cross sections for the PDR transitions below (a) and above 6.2 MeV (b) of ^{140}Ce measured in (^{17}O, ^{17}O'γ) reaction at different scattering angles. The dotted purple line represent the calculated Coulomb cross section with the DWBA while the dashed green line is the total cross section using the standard collective form factor, and solid blue line represents the total cross section using microscopically calculated form factor for the PDR states.*

The RQRPA calculations for the PDR state at 8.39 MeV provided not only the prediction of the fraction of ISEWSR but also the isoscalar strength (S_{IS}) in units of e^2fm^6/MeV (see Table 1.2). Therefore, the isoscalar strength was estimated for experimentally observed PDR states, based on the relation between EWSR and the strength function (see Eq. 1.15). If one considers, as in this case, that the whole isoscalar PDR strength is accumulated in one peak at the energy $E = 8.39\ MeV$ corresponding to the fraction of ISEWSR equal to 4.14%, and the total isoscalar strength $S_{IS} = 1.2 \cdot 10^4\ e^2fm^6$, the corresponding sum rule (M_1) can be expressed as follows:

$$M_1 = \frac{E \cdot S_{IS}}{ISEWSR[\%]} = 24420\ [e^2fm^6 \cdot MeV] \tag{5.4}$$

Then for each considered PDR excitation (i), the corresponding isoscalar strength (S_{IS}^i) was evaluated knowing the energy of the state (E_i) and the corresponding fraction of $ISEWSR_i$, that was estimated before (values given in Table 5.4). This illustrates the following equation:

$$S_{IS}^i = \frac{M_1 \cdot ISEWSR_i[\%]}{E_i} \tag{5.5}$$

The procedure was applied, similar as for the ISEWSR, both for the discrete states and the integrated regions of 200 keV. The results for each identified pygmy state are shown in Table 5.4 and in Fig. 5.20 together with the values for the total strength in bins of 200 keV. The summed strength in discrete peaks was therefore $0.20(6)\cdot10^4$ e^2fm^6. The total strength (including unresolved region) was $0.66(10)\cdot10^4$ and $0.22(5)\cdot10^4$ e^2fm^6 for low- and high-lying region, respectively, giving the total strength of $0.88(11)\cdot10^4$ e^2fm^6.

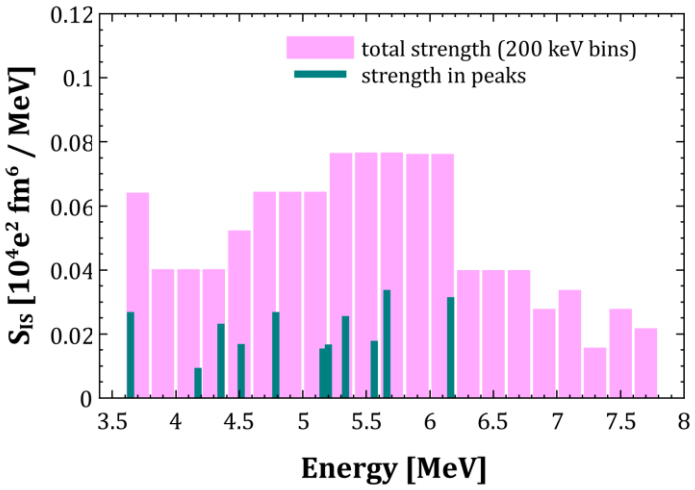

Figure 5.20: *Isoscalar strength distribution obtained for the PDR states, integrated in bins of 200 keV. The green lines correspond to the known discrete transitions. The pink bars give the total strength (including the unresolved part) corresponding to the total counts in each energy bin.*

The obtained values of the ISEWSR for ^{140}Ce can be compared with those estimated for the ^{124}Sn [Pel14a] in the same experiment and also with the cross sections from corresponding (α,α'γ) measurements. All this results are summarized in Table 5.5. The ISEWSR values are proportional to cross-sections so they are compared to each other. The ratio of the ISEWSR values for the ^{124}Sn and ^{140}Ce for the discrete peaks is equal to 5. The ratio of the cross sections for the excitation of pygmy dipole transitions between ^{124}Sn and ^{140}Ce measured in the (α,α'γ) experiments was equal to 4.92 which agrees very well with the ISEWSR ratio.

Table 5.5: *Isoscalar energy weighted sum rule (ISEWSR) exhausted by PDR estimated in (^{17}O,^{17}O'γ) for ^{124}Sn[Pel14a] and ^{140}Ce [Krz16a], together with corresponding cross sections (*dσ/dΩ*) obtained in ^{124}Sn(α,α' γ)[End12] and ^{140}Ce(α,α' γ)[End09] experiments.*

Nucleus	(^{17}O,^{17}O'γ) **ISEWSR [%]**		(α,α' γ) **dσ/dΩ [mb/sr]**
	in peaks	total	in peaks
^{124}Sn	2.20(30)	7.80(70)	10.77
^{140}Ce	0.44(12)	2.03(26)	2.19

The experimental values of ISEWSR and strength obtained for PDR states excited in ^{140}Ce nucleus were compared with the predictions of the RQRPA and RQTBA models in Table 5.6. It is important to note that RQRPA calculations overestimate the experimental values predicting the 4.14% of ISEWSR. The model, however, predicts all the PDR strength to be accumulated at one 8.39 MeV peak. Meanwhile, the average experimental energy of the PDR states for ^{140}Ce is around 5.65 MeV. As being proportional to energy, such difference results in significant change in estimation of a sum rule. As already discussed by Paar et al. [Paa09], the shift of the PDR states into higher energies as compared to experimental data might be related to the fact that RQRPA does not include effects of coupling to low-energy surface phonons which would enhance the effective nucleon mass and result in much more fragmented states. This effect is included in relativistic quasiparticle time blocking approximation (RQTBA) model. However, in the case of ^{140}Ce the relativistic models are not able to reproduce well the lowest 2^+ (phonon) state, overestimating its value of around 1.5 MeV. This is crucial in reproducing the fragmentation of the PDR states due to the coupling to the low-energy phonons. The comparison between RQRPA and RQTBA strength distributions for the ^{140}Ce was introduced in sec. 1.3.2 (Fig. 1.11). As expected, there is a shift of the pygmy dipole states to lower energies in RQTBA as compared to RQRPA, but it is still around 2 MeV above the experimental data. Also fragmentation of the PDR states is not satisfactory in isoscalar channel which was expected taking into account the difficulties with reproducing the lowest 2^+ state. It is however important to note, that RQTBA calculation predicts the ISEWSR to be 2.5% for the pygmy dipole states which is close to experimental value of 2.03(26)% for the total integrated strength consider as upper limit in this experiment.

Table 5.6: *Values of the isoscalar energy weighted sum rule (ISEWSR) exhausted by PDR and its strength (S_{IS}) for ^{140}Ce obtained in this experiment compared to corresponding calculations using RQRPA [Paa09] and RQTBA models [Krz16a].*

Method		ISEWSR [%]	S_{IS} [10^4 e^{2}fm^6]
(^{17}O,^{17}O'γ)	in peaks	0.44(12)	0.20(6)
	total	2.03(26)	0.88(11)
RQRPA (DD-ME2)		4.14	1.20
RQTBA (NL3)		2.50	1.16

As already mentioned, the method that is described in the thesis was applied to study also a several other nuclei. The strengths of the PDR states were obtained also for ^{90}Zr, ^{124}Sn and ^{208}Pb. Fig. 5.21 shows the isoscalar strength distributions for the ^{90}Zr, ^{124}Snand ^{208}Pb nuclei [Bra15] together with the results obtained for ^{140}Ce. Table 5.7 summarizes all the most important results including the energy range of the PDR states, values of ISEWSR and strength as well as the sum of B(E1) values obtained from different measurements. As one can observe, the B(E1)↑ summed for all PDR transitions is increasing with the mass of the nucleus. This is consistent with the predictions that were introduced in sec. 1.3.2 (Fig. 1.14). There is no such trend in the case of isoscalar strength of the PDR, which seems to be more related to the structure of a nucleus. More fragmentation and increased strength is observed for the ^{124}Sn nucleus with the open neutron shell. In general, the fragmentation of the strength is decreasing with increasing mass. The exception from the trend is observed in the ^{90}Zr nucleus, however, this might be due to the fact that in this case, several expected transitions above 7 MeV where not observed [Cre15]. Nevertheless, there is definitely a need for much more systematic studies of the PDR properties. This would also be very interesting to obtain results not only for the spherical but also deformed nuclei. In such a case, one might expect to observe kind of splitting of the PDR strength due to deformation as in the case of GDR [Ber75].

Table 5.7: *The isoscalar strength (S_{IS}), fraction of isoscalar energy sum rule (ISEWSR) and B(E1)↑ values for ^{90}Zr [Cre15], ^{124}Sn [Pel14a], ^{140}Ce [Krz16a] and ^{208}Pb [Cre14] nuclei studied with (^{17}O,^{17}O'γ) method.*

Nucleus	Selection	Energy range [MeV]	S_{IS} [10^4 e^{2}fm^6 / MeV]	ISEWSR [%]	B(E1)↑ [10^{-3} e^{2}fm^2]
^{90}Zr	in peaks	6.3 – 6.9	4.6(7)	4.0(6)	87
^{124}Sn	in peaks	5.5 – 9.0	11.9(1.6)	2.2(3)	228
^{124}Sn	total	5.5 – 9.0	41.1(3.7)	7.8(7)	228
^{140}Ce	in peaks	4.1 – 7.8	0.20(6)	0.44(12)	307
^{140}Ce	total	4.1 – 7.8	0.88(11)	2.03(26)	307
^{208}Pb	in peaks	4.8 – 7.3	8.9(1.5)	9.0(1.5)	1084

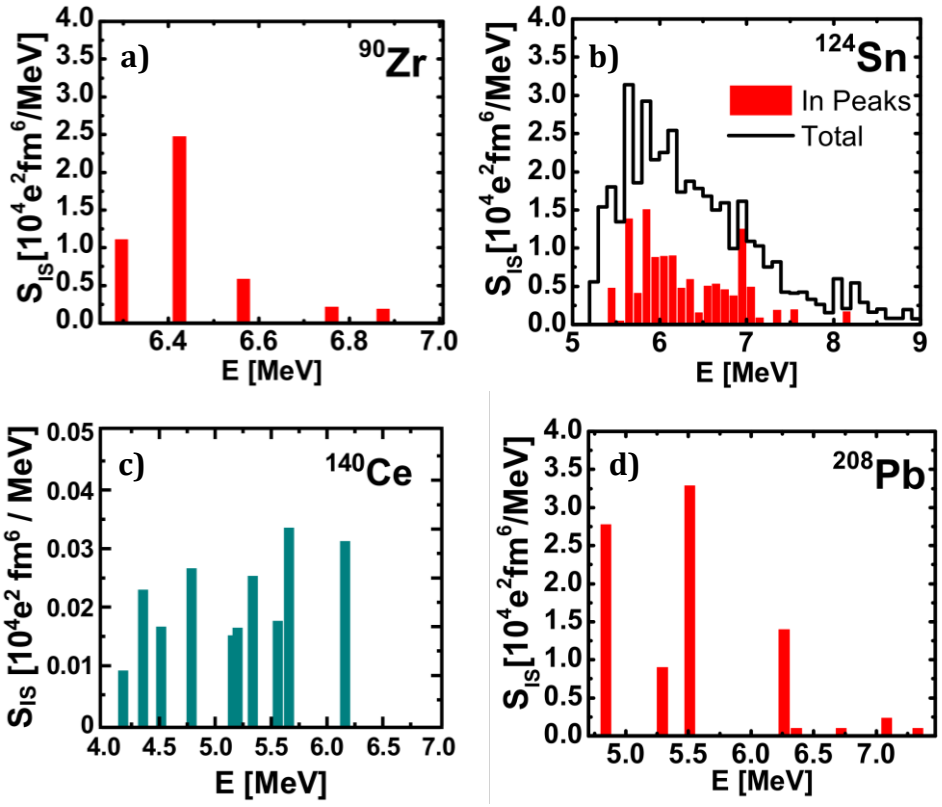

Figure 5.21: *Isoscalar strength distribution measured for the PDR states [Bra15, Krz16a]. The full coloured red bars correspond to the isoscalar strength of the observed known discrete transitions for the case of ^{90}Zr (a) and ^{208}Pb (d) and to the sum of known discrete transitions in each energy bin of 100keV for the case of ^{124}Sn (b). In the right panel the black histogram gives the total strength (including the unresolved part) corresponding to the total counts in each energy bin. The results for ^{140}Ce are included in panel (c).*

Chapter 6. CONCLUSIONS AND OUTLOOK

The low-lying dipole states around neutron emission energy are attracting a lot of attention as there are still many open questions regarding their origin and nature. Particular interest has been put into the isospin structure of the PDR. As it was revealed by using different probes with different interaction mechanisms, PDR constitutes of a mixture of isoscalar and isovector states. The calculations predict that transitions densities of the isoscalar part of the PDR are peaked on the nuclear surface, while the isovector part is associated towards the tail of GDR. These findings emphasised a need for further studies using probes, which would be sensitive to the nuclear surface and interact mainly *via* nuclear interaction.

The dedicated experiment has been performed at Legnaro National Laboratories (LNL, Italy) for studying the γ decay of high-lying states in several nuclei (^{90}Zr, ^{124}Sn, ^{140}Ce, ^{208}Pb). The nuclei have been excited *via* inelastic scattering of ^{17}O nuclei at the energy of 20 MeV/u. The scattered ions were detected by the two silicon ΔE-E telescopes of TRACE array, while γ-rays originating from target de-excitation were registered by 5 triple clusters of HPGe detectors of AGATA-Demonstrator and 9 large volume $LaBr_3$:Ce detectors of HECTOR+ array.

The thesis concentrates on the results for ^{140}Ce spherical nucleus with a magic number of neutrons. Particular interest has been put to the first dipole state at 3643 keV which is postulated to originate from two-phonon ($2^+ \otimes 3^-$) coupling and the rest of the 1^- states to be of a pygmy dipole resonance nature. It was possible to identify decays to the ground state by correlating the energy of detected γ-rays with the excitation energy transferred to the target nucleus. The position sensitivity of AGATA and TRACE arrays allowed to study the multipolarity of emitted γ-rays with respect to the scattered ions.

In this experiment, it was possible to observe the known decays to ground state from the single phonon states (2^+ and 3^-) which should be the constituents of the two-phonon 1^- state. The gamma-gamma coincidence analysis allowed to select the decays to the 2^+ state but no clear indication of the direct decay from 1^- to 2^+ was observed. Such observation would be the proof of the pure harmonic coupling of the phonons, however, this is below sensitivity limit of this experiment so that the possibility of pure harmonic coupling cannot be excluded. Furthermore, it was possible to observe the decay from the 2^+ to 3^- states which supports the assumption of two-phonon coupling. The analysis of the experimental differential cross sections as a function of scattering angle compared to calculations using the DWBA approach allowed to shed some light into the nature of the possible two-phonon state. Indeed the obtained results were compared with those for the higher-lying pygmy dipole state and this comparison allowed to conclude that these two states have different character. The excitation mechanism of the two-phonon state is mainly due to the Coulomb interaction with a rather small nuclear contribution well described by the standard collective form factor. In contrast, the cross section for the pygmy dipole state was found to have a strong nuclear contribution and it was reproduced using the

form factor calculated by double-folding transitions densities obtained with the RQRPA model for the pygmy dipole state.

The results of the analysis have shown that in the PDR energy region between 4 and 8 MeV, the E1 γ-transitions dominate, as it was revealed in NRF experiments. Obtained differential cross sections for the excitation of pygmy dipole states are in a very good agreement with the ones previously estimated using (α,α'γ) reaction which confirms the selectivity in excitation of such states as compared to (γ,γ'). Some differences however exists, confirming the need for further studies using heavy ions to probe the shape of the transition densities in more details, especially their surface part. DWBA analysis for the pygmy dipole states using microscopically calculated form factor based on the transition densities obtained with RQRPA allowed to extract the percentage of isoscalar energy weighted sum rule exhausted by PDR and its strength in ^{140}Ce for the first time. This analysis confirmed that the low-energy PDR states have more isoscalar character than high-energy part. The overestimation of the experimental ISEWSR by RQRPA predictions might be explained due to the fact that RQRPA calculations do not take into account the effects of coupling to low-energy surface phonons. It has been found that the pygmy mode, arising in the RQRPA as a single state or as very few low lying dipole states with isoscalar character, is strongly fragmented over many states in a broad energy region due to the coupling to phonons. As a result, some fraction of the strength is located well below the original position of the RQRPA pygmy mode. In case of ^{140}Ce it is difficult to reproduce the fragmentation of the pygmy dipole states as relativistic models largely overestimate the energy of the lowest 2^+ phonon. However, the experimental value estimated as an upper limit fits well with the predictions of RQTBA model which includes the effect of phonon coupling.

The results for ^{140}Ce have been compared to the one obtained for ^{124}Sn with the same (^{17}O,^{17}O'γ) technique as well as with the (α,α'γ) measurements demonstrating high consistency. This allows to conclude that inelastic scattering of ^{17}O at 20 MeV/u is a very good tool to probe the isoscalar component of the highly-excited states.

Trying to have an outlook for possible future studies of PDR in nuclei, the presented technique (inelastic scattering of heavy ions coupled to high-resolution gamma detection systems) can be used for different stable nuclei over the nuclear chart. The experimental set-up requires an improvement to achieve better energy resolution of Si telescopes for precise estimation of excitation energy. Also the γ-rays detection efficiency would be improved by using the AGATA and HECTOR+ in extended configurations.

There are also other very promising experimental perspectives for stable nuclei. A long campaign will start in late 2016 in RCNP (Osaka, Japan) where complementary beams of protons and alpha particles will be used to study the isospin properties of PDR in many nuclei from different mass regions. Additionally to previous campaigns, the coincident high-resolution gamma spectroscopy will be also performed. Similar techniques of using proton beams are now tested at Cyclotron Centre Bronowice at IFJ PAN Krakow (Poland).

Another yet promising perspective for studying stable nuclei comes from the ELI-NP project in Bucharest (Romania), which aims to provide a very intense ($\sim 10^{13}$ γ/s), brilliant γ beam of ~0.1 % bandwidth and energy up to 19 MeV, obtained by incoherent Compton back scattering of a laser light off an intense electron beam (E_e > 700 MeV). This will allow to use well known NRF and (γ,n) methods but with remarkable precision, especially valuable to study the strength functions around neutron separation energy.

As far as the PDR excitations in exotic, for example neutron-rich nuclei are concerned, they were so far successfully studied by using relativistic (>600 MeV/u) radioactive beams and the relativistic Coulomb excitation method (experiments LAND and RISING in GSI Darmstadt). Such studies, profiting with the high cross-section of the Coulomb excitation at relativistic energies, will be pursued in the future in even more exotic nuclei at the GSI/FAIR facility in Darmstadt. However in this case high-velocities of the excited nuclei and corresponding Doppler broadening is causing rather low energy resolution of the obtained spectra.

Nonetheless, the methods obtained in the present work might be directly adapted to possible future experiments with slow (ca. 20 MeV/u) exotic, radioactive beams, soon to be available in such facilities as GANIL/SPIRAL2 in Caen, SPES in Legnaro, or HIE-ISOLDE at CERN. In such cases, the PDR excitations of the exotic nuclei from the beam could be studied in inverse kinematics, using inelastic scattering on a solid, weakly bound targets, as for example the ^{13}C. Such experiments and use of high-resolution gamma-detectors (as AGATA) will allow to study the fine structure of the pygmy dipole resonance strength in nuclei far from the valley of stability.

Appendix A. BINARY REACTION KINEMATICS

Aim of this appendix is to introduce the kinematic of the binary reaction kinematic of the type:

$$a + A \rightarrow b + B \qquad (A.1)$$

where a is the incoming ion beam with a velocity $\overrightarrow{v_a}$ and mass m_a ; A is the target nucleus with a mass m_A. which is at rest in laboratory frame of reference; b is the projectile-like reaction product and B is the target-like product. Their mass and velocity are m_b, m_B and $\overrightarrow{v_b}, \overrightarrow{v_B}$, respectively.

In the appendix, certain quantities regarding the reaction kinematics will be given in laboratory frame of reference and then the formulas for transformation to a centre-of-mass frame of reference.

Only classical mechanics will be considered, neglecting relativistic effects.

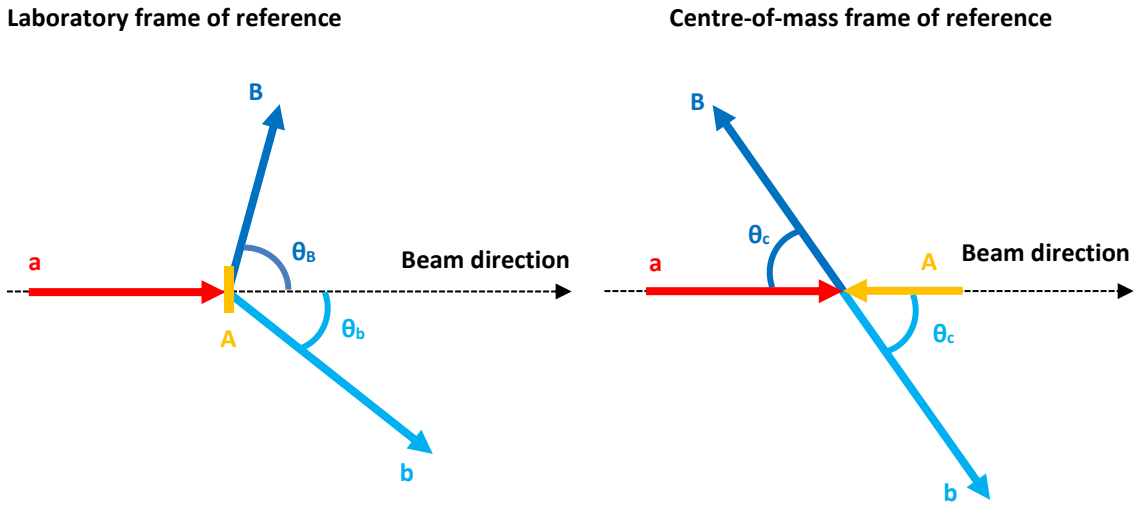

Figure A.1: *Schematic view of a binary reaction in the laboratory and in the centre-of-mass frame of reference.*

A1. Laboratory Frame of Reference

If one considers a laboratory frame of reference, a target A is assumed to be in rest. Considering the laws of energy and momentum conservation:

$$K_a = K_b + K_B - Q \qquad (A.2)$$

and:

$$m_a v_a = m_b v_b cos\theta_b + m_B v_B cos\theta_B \qquad (A.3)$$

$$m_b v_b sin\theta_b = m_B v_B sin\theta_B \qquad (A.4)$$

where the angles θ_b, θ_B are defined in Fig. A.1 (left panel). K_a, K_b, K_B are the kinetic energies of a, b, B. Q-value of the reaction is the difference between initial and final mass of the system:

$$Q = (m_a + m_A - m_b - m_B)c^2 - E_{ex} \qquad (A.5)$$

Where E_{ex} is the excitation energy transferred to the internal degrees of freedom of either nuclei.

From Eqs. A.3 and A.4 it is possible to calculate:

$$tan\theta_B = \frac{sin\theta_b}{\sqrt{\frac{m_a K_a}{m_b K_b}} - cos\theta_b} \qquad (A.6)$$

$$v_B = v_b \frac{m_b sin\theta_b}{m_b sin\theta_b} \qquad (A.7)$$

A2. Centre of Mass Frame of Reference

In experimental nuclear physics, all observations take place in a reference frame that is at rest in the laboratory, referred to as the laboratory frame of reference. From the theoretical point of view, however, the motion of the centre of mass is of no consequence for the properties of a nuclear reaction. It is then often more convenient to use a moving coordinate frame in which the centre of mass of the two colliding nuclei is at rest, called the centre-of-mass coordinate system.

In the centre-of-mass frame of reference, both nuclei are moving towards each other with equal and opposite momenta:

$$m_a v'_a = m_A v'_A \qquad (A.8)$$

where v'_a and v'_A are the speed of projectile and target in the centre-of-mass frame of reference.

If v_{CM} is the speed of the centre of mass in the laboratory frame of reference, then by definition of the centre of mass has:

$$v_{CM} = v_a \frac{m_a}{m_a + m_A} \qquad (A.9)$$

meaning that the velocities of a and A in the centre-of-mass system are:

$$v'_a = v_a - v_{CM} = v_a \frac{m_a}{m_a + m_A} \qquad (A.10)$$

$$v'_A = -v_{CM} = -v_a \frac{m_a}{m_a + m_A} \qquad (A.11)$$

After the collision, b and B move in opposite direction in the centre-of-mass frame, due to momentum conservation, as shown in Fig. A.1 (right panel). Their direction forms and angle θ_C with the direction before the collision (that is the beam direction). This implies that:

$$m_b v'_b = m_B v'_B \qquad (A.12)$$

where *v'_b and v'_B are the speeds of b and B in centre-of-mass system, related to the speed in laboratory system by:*

$$v'_b cos\theta_C = v_b cos\theta_b - v_{CM} \qquad (A.13)$$

$$v'_b sin\theta_C = v_b sin\theta_b \qquad (A.14)$$

It should be noted that, it the Q-value is non-zero, the velocity of the centre-of-mass changes between the initial and final state, with the relation:

$$v_{CM,f} = v_{CM,f} \frac{m_a + m_A}{m_b + m_B} \qquad (A.15)$$

Typically, however, the Q-value is only $\sim 10^{-3}$ – 10^{-5} of the total mass of the system and we can assume $v_{CM,f} \cong v_{CM,i}$.

Using Eqs. A.13 and A.14 one obtains the relation between the angles in the laboratory and the centre-of-mass frame of reference:

$$tan\theta_b = \frac{sin\theta_C}{cos\theta_C + \gamma} \qquad (A.16)$$

where γ is the ratio of the velocities of the centre of mass and of the particle b in the centre-of-mass frame of reference:

$$\gamma = \frac{v_{CM}}{v'_b} = \sqrt{\frac{m_a m_b}{m_A m_B} \frac{K_a}{\left(1 + {}^{m_a}/_{m_A}\right) Q + K_a}} \qquad (A.17)$$

The second equality has been derived from Eq. A.2

Appendix B. FRESCO CODE

The calculations of the cross sections for the inelastic excitations were done with DWBA using FRESCO code [Tho88]. The example of the FRESCO input file, for the excitation of the 2^+ state at 1596 keV in ^{140}Ce via inelastic scattering of ^{17}O at 20 MV/u, is shown in Fig. B.1.

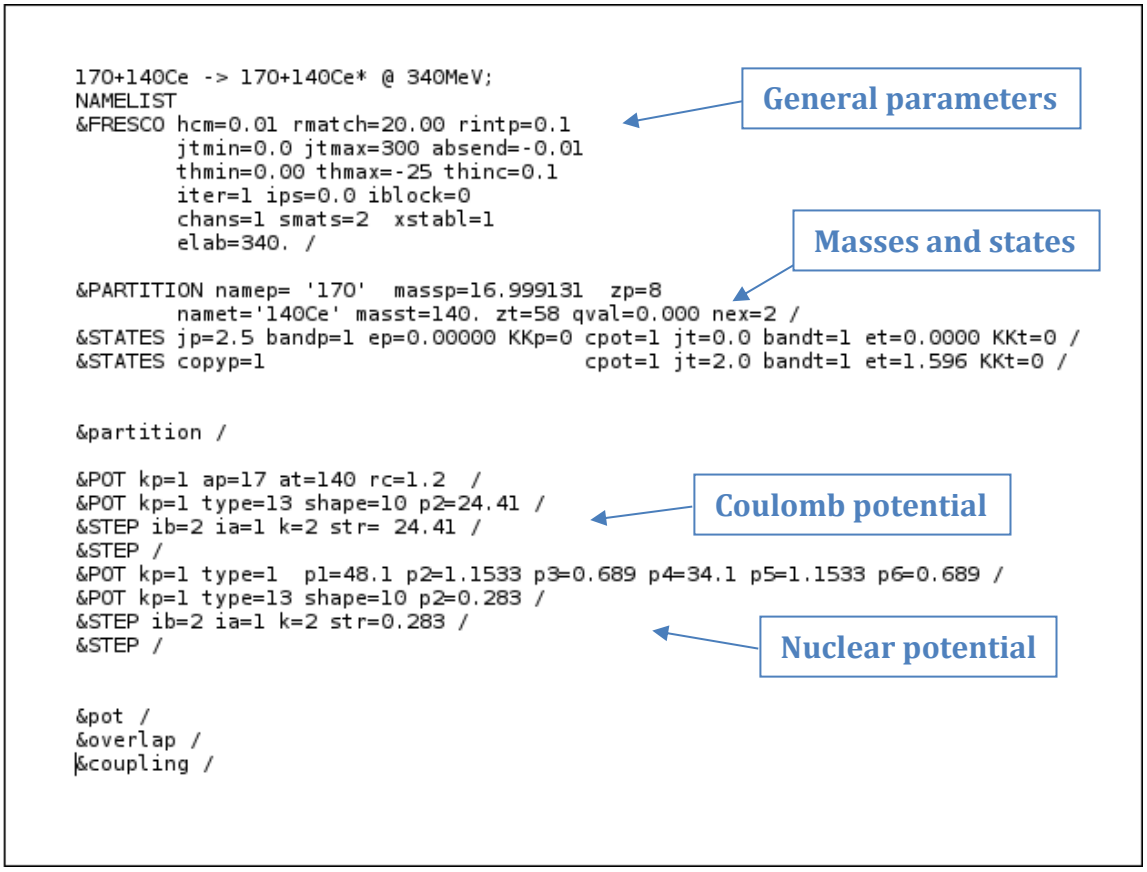

Figure B.1: *Input file with the parameters used by the FRESCO code for the excitation of 2^+ state at 1596 keV in ^{140}Ce via inelastic scattering of ^{17}O at 20 MeV/u.*

The most important parameters that are required by the code can be divided into three sections:

General parameters

- *thmin-thmax* is the range of scattering angles (in the CM frame of reference) for which to perform the calculations
- *thinc* is the angular increment
- *jtmax* is the number of partial waves considered
- *rmatch* is the maximum distance for the integration

- *elab* is the beam energy

Masses and states

- the entrance and exit channels of the reaction
- the spin (*jp*) and parity (*bandp*) of projectile ground state
- the energy (*et*), spin (*jt*) and parity (*bandt*) of the excited state

Coulomb potential

- Coulomb radius parameter (*rc*)
- the Coulomb deformation parameter (*str*)[related to $B(E_L)$]

Nuclear potential

- the depth, radius and diffusiveness for both the real and the imaginary part of the optical potential (*p1* to *p6*)
- the nuclear deformation parameter (*str*) [related to RDEF(L)]
- the type of form factor (*shape*) – can be changed into a list-mode file as in the case of PDR form factor used in the thesis by changing parameter into *shape=9*

ACKNOWLEDGEMENTS

Prowadzenie badań naukowych w grupie kierowanej przez prof. dr hab. Adama Maja pozwoliło mi docenić nie tylko efekty kolektywne obserwowane w jądrach atomowych, ale przede wszystkich we wzajemnej współpracy międzyludzkiej. Dlatego też chciałbym podziękować wielu osobom, z którymi miałem przyjemność współpracować w czasie wykonywania mojej pracy doktorskiej.

Serdeczne podziękowania kieruję do promotorów mojej rozprawy: dr hab. Piotra Bednarczyka (główny) i dr hab. Marii Kmiecik (pomocniczy). Bardzo doceniam, iż zawsze mogłem liczyć na fachową pomoc na każdym etapie badań i pisania pracy. Szczególnie dbałość dr hab. Piotra Bednarczyka o przejrzystość prezentowanych myśli była dla mnie stymulacją do pogłębiania swej wiedzy. Nie mniej doceniam również dużą swobodę jaką mi zapewnili pozwalając na rozwijanie samodzielności, szczególnie we współpracy międzynarodowej.

Nie mniej serdecznie dziękuję Prof. dr hab. Adamowi Majowi, którego wiedza i profesjonalizm stanowi dla mnie inspirację.

I would also like to specially thank Prof. Angela Bracco, the leader of Milano group, for Her professional guidance with strong involvement and patience. I gratefully acknowledge the whole Milano group, especially dr. Fabio Crespi who was my guide in complex data analysis. I thank also dr. Roberto Nicolini and dr. Luna Pellegrii for their contribution in development of data analysis tools.

I am also very grateful to Prof. Nils Paar, dr. Elena Litvinova, and dr. Edoardo Lanza for their valuable contribution in theoretical analyses.

Chciałbym również podziękować dr inż. Michałowi Ciemale za profesjonalne wprowadzenie w tajniki zaawansowanych symulacji danych.

Na koniec dziękuję wszystkim pracownikom i doktorantom Zakładu Struktury Jądra IFJ PAN, którzy tworzą wspaniałą atmosferę, pozwalająca nie tylko na prowadzenie badań naukowych na najwyższym poziomie, ale też daje niezbędną w pracy naukowej radość.

Badania zamieszone w niniejszej pracy zostały przeprowadzone w ramach grantu o numerze 2013/09/N/ST2/04093 ufundowanego przez Narodowe Centrum Nauki.

REFERENCES

[Adr05] Adrich P., Klimkiewicz A., Fallot M., Boretzky K., Aumann T., Cortina-Gil D., Datta Pramanik U., Elze Th. W., Emling H., Geissel H., Hellstroöm M., Jones K. L., Kratz J. V., Kulessa R., Leifels Y., Nociforo C., Palit R., Simon H., Surówka G., Sümmerer K., *Evidence for Pygmy and Giant Dipole Resonances in ^{130}Sn and ^{132}Sn*, Phys. Rev. Lett. 95, 132501 (2005).

[Akk12] Akkoyun S., et al. (AGATA collaboration), *AGATA—Advanced Gamma Tracking Array,* Nucl. Instr. And Meth. A 668, 26 (2012).

[Avi11] Avigo R., *Caratterizzazione dei rivelatori HPGe segmentati on raggi gamma ad alta energia*. Master's thesis, University of Milan (2011).

[Bar61] Bartholomew G. A., *Neutron Capture Gamma Rays*, Annu. Rev. Nucl. Sci. 11, 259 (1961).

[Bas08] Bastrukov S. I., Molodtsova I. V., Podgainy D. V., Mişicu S. and Chang H. –K., *Elasticity of nuclear medium as a principal macrodynamical promoter of electric pygmy dipole resonance*, Phys. Lett. B 664, 258 (2008).

[Bass80] Bass R., *Nuclear Reactions with Heavy Ions* (Springer-Verlag 1980).

[Baz91] Bazzacco D., Cederwall B., Cresswell J., Duchêne G., Eberth J., Gast W., Gerl J., Korten W., Lazarus I., Lieder R.M., Simpson J., Weisshaar D., *AGATA, Technical Proposal for an Advanced Gamma Tracking Array for the European Gamma Spectroscopy Community*. J. Gerl and W. Korten. AGATA collaboration, 87 (1991).

[Baz02] Bazina D., Tarasov O., Lewitowicz M, Sorlin O., *The program LISE: a simulation of fragment separators*, Nucl. Instrum. And Meth. A482, 307 (2002).

[Baz04] Bazzacco D., *The Advanced Gamma Ray Tracking Array AGATA*, Nucl. Phys. A 746, 248-254 (2004).

[Baz05] Bazzacco D., Bednarczyk P., Bellato M., Coleman-Smith P .J., Czermak A., Dulny B., Gadea A., Houarner Ch., Isocrate R., Jones P., Meczyński W., Olivier L., Pucknell V., Theisen Ch., Weber Ch., Wittwer G., Zięblíński M., *AGATA Ancillary Detectors and Ancillary Detector Integration Working Group Specifications of the AGAVA (AGATA Ancillary VME Adapter) Ancillary Detector GTS Interface* (2005).

[Ber69] Berman B. L., Van Hemert R. L., and Bowman C. D., *Threshold Photoneutron Cross Section for Mg26 and a Source of Stellar Neutrons*, Phys. Rev. Lett. 23, 386 (1969).

[Ber70] Berman B.L., Fultz S.C., Caldwell J.T., Kelly M.A., Dietrich S.S., *Photoneutron Cross Sections for Ba138 and N14*, Phys. Rev. C 2, 2318 (1970).

[Ber75] Berman B.L., Fultz S.C., Rev. Mod. Phys. 47, 713 (1975).

[Bert88] Bertrand F. E., Beene J. R., and Horen D. J., *Heavy ion excitation of giant resonances – The next generation*, Nucl. Phys. A 482, 1-2, 287-303 (1988).

[Boi08] Boiano C., Bassini R., Camera F., Million B., Wieland O., Giaz A., *A 16 channel NIM module for a complete processing of fast scintillator signals*, In IEEE Nuclear Science Symposium Conference Record, 2068 (2008).

[Bor98] Bortignon P. F., Bracco A. and Broglia R. A., *Giant Resonances: Nuclear Structure at Finite Temperature* (Amsterdam: Harwood Academic, 1998).

[Bos07] Boston A. J., Boston H.C., Cresswell J.R., Dimmock M.R., Nelson L., Nolan P.J., Rigbya S., Lazarus J., Simpson J., Medina P., Santos C., Parisel C., *Gamma-ray tracking: Characterisation of the AGATA symmetric prototype detectors*, Nucl. Instr. And Meth. B 261, 1- 2, 1098-1102 (2007).

[Bro00] Brown B. Alex, *Neutron Radii in Nuclei and the Neutron Equation of State*, Phys. Rev. Lett. 85, 5296 (2000).

[Bra15] Bracco A., Crespi F. C. L., and Lanza E. G., *Gamma decay of pygmy states from inelastic scattering of ions*, Eur. Phys. J. A 51 (2015).

[Bru77] Brussaard P. and Glaudemans P., *Shell-model applications in nuclear spectroscopy* (North-Holland, Amsterdam, 1977).

[Brz69] Brzosko J. S., Gierlik E., Soltan A., Wilhelmi Z., *Effect of the pigmy resonance on the calculations of the neutron capture cross section*, Can. J. Phys. 47, 2849 (1969).

[Car10] Carbone A., Colò G., Bracco A., Cao L.-G., Bortignon P. R., Camera F, and Wieland O., *Constraints on the symmetry energy and neutron skins from pygmy resonances in Ni68 and ^{132}Sn*, Phys. Rev. C 81, 041301I.

[Cre07] Crespi F. C. L., Camera F. , Wieland O., Benzoni G., Brambilla S., Million B., Montanari D., *A pulse shape analysis algorithm for HPGe detectors*, Nucl. Instr. And Meth. A 570, 3, 459-466, (2007).

[Cre13] Crespi F. C. L., Avigo R., Camera F., Akkoyun S., Ataç A., Bazzacco D., Bellato M., Benzoni G., Blasi N., Bortolato D., Bottoni S., Bracco A., Brambilla S., Bruyneel B., Ceruti S., Ciemała M., Coelli S., Eberth J., Fanin C., Farnea E., Gadea A., Giaz A., Gottardo A., Hess A., Kmiecik M., Leoni S., Maj A., Mengoni D., Michelagnoli C., Million B., Montanari D., Nicolini R., Pellegri L., Recchia F., Reiter P., Riboldi S., Ur C.A., Vandone V., Valiente-Dobon J.J., Wieland O., Wiens A., *Response of AGATA segmented HPGe detectors to gamma rays up to 15.1 MeV*, Nucl. Instrum. And Meth. In Phys. Res. A 705, 47 (2013).

[Cre14] Crespi F. C. L., Bracco A., Nicolini R., Mengoni D., Pellegri L., Lanza E. G., Leoni S., Maj A., Kmiecik M., Avigo R., Benzoni G., Blasi N., Boiano C., Bottoni S., Brambilla S., Camera F., Ceruti S., Giaz A., Million B., Morales A.I., Vandone V., Wieland O., Bednarczyk P., Ciemała M., Grebosz J., Krzysiek M., Mazurek K., Zieblinski M., Bazzacco D., Bellato M., Birkenbach B., Bortolato D., Calore E., Cederwall B., Charles L., de Angelis G., Désesquelles P., Eberth J., Farnea E., Gadea A., Görgen A. , Gottardo A., Isocrate R., Jolie J., Jungclaus A., Karkour

N., Korten W., Menegazzo R., Michelagnoli C., Molini P., Napoli D. R., Pullia A., Recchia F., Reiter P., Rosso D., Sahin E., Salsac M. D., Siebeck B., Siem S., Simpson J., Söderström P.-A., Stezowski O., Theisen Ch., Ur C, and Valiente-Dobón J. J., *Isospin Character of Low-Lying Pygmy Dipole States in Pb208 via Inelastic Scattering of O17 Ions*, Phys. Rev. Lett. 113, 012501 (2014).

[Cre15] Crespi F.C.L. , Bracco A., Nicolini R., Lanza E. G., Vitturi A., Mengoni A., Leoni S., Benzoni G., Blasi N., Boiano C., Bottoni S., Brambilla S., Camera F., Corsi A., Giaz A., Million B., Pellegri L., Vandone V., Wieland O., Bednarczyk P., Ciemała M., Kmiecik M, Krzysiek M., Maj A., Bazzacco D., Bellato M., Birkenbach B., Bortolato D., Calore E., Cederwall B., de Angelis G., Désesquelles P., Eberth J., Farnea E., Gadea A., Görgen A., Gottardo A., Hess H., Isocrate R., Jolie J., Jungclaus A., Kempley R. S., Labiche M., Menegazzo R., Michelagnoli C., Molini P., Napoli D. R., Pullia A., Quintana B., Recchia F., Reiter P., Sahin E., Siem S., Söderström P.-A., Stezowski O., Theisen Ch., Ur C., and Valiente-Dobón J. J., Phys. Rev. C 91, 024323 (2015).

[Cze05] Czermak A., private communication

[End09] Endres J., Savran D., M. van den Berg A., Dendooven P., Fritzsche M., Harakeh M. N., Hasper J., Wörtche H. J., and Zilges A., *Splitting of the pygmy dipole resonance in ^{138}Ba and ^{140}Ce observed in the (α,α') reaction*, Phys. Rev. C 80, 034302 (2009).

[End12] Endres J., Savran D., Butler P. A., Harakeh M. N., Harissopulos S., Herzberg R.-D., Krücken R., Lagoyannis A., Litvinova E., Pietralla N., Ponomarev V.Yu., Popescu L., Ring P., Scheck M., Schlüter F., Sonnabend K., Stoica V. I., Wörtche H. J., and Zilges A., *Structure of the pygmy dipole resonance in ^{124}Sn*, Phys. Rev. C 85, 064331 (2012).

[Fal03] Fallot M., Chomaz Ph., Andrés M.V., Catara F., Lanza E.G., Scarpaci J.A., *Anharmonic vibrations in nuclei*, Nucl. Phys. A 729, 699 (2003).

[Far10] Farnea E., Recchia F., Bazzacco D., Kröll Th., Podolyák Zs., Quintana B., Gadea A., *Conceptual design and Monte Carlo simulations of the AGATA array*, Nucl. Instrum. And Meth. In Phys. Res. 621, 331 (2010).

[Gad11] Gadea A., et al. (AGATA Collaboration), *Conceptual design and infrastructure for the installation of the first AGATA sub-array at LNL*, Nucl. Instr. And Meth. A 654, 88 (2011).

[Gia13] Giaz A., Pellegri L., Riboldi S., Camera F., Blasi N., Boiano C., Bracco A., Brambilla S., Ceruti S., Coelli S., Crespi F.C.L., Csatlòs M., Frega S., Gulyàs J., Krasznahorkay A., Lodetti S., Million B., Owens A., Quarati F., Stuhl L., Wieland O., *Characterization of large volume 3.5″×8″ LaBr3:Ce detectors*, Nucl. Instr. And Meth. A 729, 21, (2013).

[Gor98] Goriely S., *Radiative neutron captures by neutron-rich nuclei and the r-process nucleosynthesis*, Phys. Lett. B 436 (1998) 10.

[Gor04] Goriely S., Khan E., Samyn M., *Microscopic HFB + QRPA predictions of dipole strength for astrophysics applications*, Nuclear Phys. A 739 (2004) 331.

[Gra05] Grave X., Canedo R., Clavelin J.-F., Du S., and Legay E., *NARVAL a modular distributed data acquisition system with Ada 95 and RTAI*, in Real Time Conference, 2005. 14th IEEE-NPSS, 2005.

[Gri94] Grinberg M. and Stoyanov Ch., *Distribution of two-phonon strength in even N = 82 nuclei*, Nucl. Phys. A 573 (1994) 231.

[Har01] Harakeh M. and van der Woude A., *Giant Resonances: Fundamental High Frequency Modes of Nuclear Excitation*, (Oxford University Press, 2001).

[Her97] Herzberg R.-D., von Brentano P., Eberth J., Enders J., Fischer R., Huxel N., Klemme T., von Neumann-Cosel P., Nicolay N, Pietralla N., Ponomarev V.Yu., Reif J., Richter A., Schlegel C., Schwengner R., Skoda S., Thomas H.G., Wiedenhöver I., Winter G., Zilges A., *Fine structure of the E1 response in 140Ce below the particle threshold*, Phys. Lett. B 390 (1997) 49.

[Hor91] Horen D., Auble R. L., Beene J. R., Bertrand F. E., Halbert M. L., Satchler G. R., Thoennessen M., Varner R. L., Brown V. R., Anthony P. L., and Madsen V. A., *Isospin character of transitions to bound states in Pb-204,206,208 using inelastic scattering of O-17 ions*, Phys. Rev. C 44, 128 (1991).

[Iga86] Igashira M., Kitazawa H., Shimizu M., Komano H., and Yamamuro N., *Systematics of the pygmy resonance in keV neutron capture γ-ray spectra of nuclei with N ≈ 82–126*, Nucl. Phys. A 457, 301 (1986).

[Kha05] Khan E., Goriely S., Allard D., Parizot E., Suomijarvi T., Koning A. J., Hilaire S., Duijvestijn M. C., *Photodisintegration of Ultra-High-Energy Cosmic Rays revisited*, Astropart. Phys. 23, 191 (2005).

[Kim77] Kim W., Miller B. L., Calarco J. R., Cardman L. S., Connelly J. P., Fayans S. A., Frois B., Goutte D., Heisenberg J. H., Hersman F. W., Meot V., Milliman T. E., Mueller P., Papanicolas C. N., Platonov A. P., Ponomarev V. Yu., and Wise J. E., *Interplay between single-particle and collective degrees of freedom in the excitation of the low-lying states in Ce140*, Phys. Rev. C 45, 2290 (1992).

[Kra88] Krane K.S., *Introdudctory Nuclear Physics* (USA, John Wiley & Sons, 1988).

[Kli07] Klimkiewicz A., Adrich P., Boretzky K., Fallot M., Aumann T., Cortina-Gil D., Datta Pramanik U., Elze Th. W., Emling H., Geissel H.,Hellstroem M., Jones K.L., Kratz J.V., Kulessa R., Leifels Y., Nociforo C., Palit R., Simon H., Surowka G., Summerer K., Typel S., and Waluś W., *Dipole response of neutron-rich Sn isotopes*, Nucl. Phys. A 788, 145c–152c (2007).

[Kmax] http://www.sparrowcorp.com/products/software, "Kmax – Advanced Tools for Industry, Education and Research."

[Koj07] Kojouharov I., Tashenov S., Engert T, Gerl J., and Schaffner H., *The GSI HPGe detector scanner – a sophisticated device based on PET technique*, in IEEE Nuclear Science Symposium Conference Record, 2007. NSS '07, 3, 2213-2215 (2007).

[Krö01] Kröll T. and Bazzacco D., *Simulation and analysis of pulse shapes from highly segmented HPGe detectors for the Î3-ray tracking array MARS*, Nucl. Instr. And Meth. A 463, 227-249, (2001).

[Krö06] Kröll T. and Bazzacco D., *A genetic algorithm for the decomposition of multiple hit events in the γ-ray tracking detector MARS*, Nucl. Instr. And Meth. A 565, 691-703 (2006).

[Krz14] Krzysiek M., Kmiecik M., Maj A., Bednarczyk P., Ciemała M., Fornal B., Grębosz J., Mazurek K., Męczyński W., Ziębliński M., Crespi F.C.L., Bracco A., Benzoni G., Blasi N., Boiano C., Bottoni S., Brambilla S., Camera F., Giaz A., Leoni S., Million B., Morales A.I., Nicolini R., Pellegri L., Riboldi S., Vandone V., Wieland O., De Angelis G., Napoli D.R., Valiente-Dobon J.J., Bazzacco D., Farnea E., Gottardo A., Lenzi S., Lunardi S., Mengoni D., Michelagnoli C., Recchia F., Ur C., Gadea A., Huyuk T., Barrientos D., Birkenbach B., Geibel L., Hess H., Reiter P., Steinbach T., Wiens A., BürgerA., Görgen A., Guttormsen M., Larsen A.C. and Siem S., *Study of the soft dipole modes in ^{140}Ce via inelastic scattering of ^{17}O*, Phys. Scr. 89, 054016 (2014).

[Krz16a] Krzysiek M., Kmiecik M., Maj A.,Bednarczyk P., Bracco A., Crespi F.C.L, Lanza E.G., Litvinova E., Paar N., Avigo R., Bazzacco D., Benzoni G.,2 Birkenbach B., Blasi N., Bottoni S., Brambilla S., Camera F., Ceruti S., Ciemała M., de Angelis G., Desesquelles P., Eberth J., Farnea E., Gadea A., Giaz A., Gorgen A., Gottardo A., Grębosz J., Hess H., Isocarte R., Jungclaus A., Leoni S., Ljungvall J., Lunardi S., Mazurek K.,Menegazzo R.,Mengoni D., Michelagnoli C., Milion B., Morales A.I., Napoli D.R.,Nicolini R., Pellegri L., Pullia A.,Quintana B, Recchia F., Reiter P.,Rosso D.,Salsac M.D.,Siebeck B.,Siem S., Soderstrom P.-A.,Ur C., Valiente-Dobon J.J.,Wieland O. and Ziębliński M., *Study of the pygmy dipole resonance in ^{140}Ce via inelastic scattering of 17O*, Phys. Rev. C (2016) (accepted).

[Krz16b] Krzysiek M., Kmiecik M., Maj A., Bednarczyk P., Bracco A., Crespi F.C.L, Lanza E.G., Avigo R., Bazzacco D., Benzoni G., Birkenbach B., Blasi N., Bottoni S., Camera F., Ceruti S., Ciemała M., De Angelis G., Farnea E., Gadea A., Giaz A., Görgen A., Gottardo A., Grębosz J., Isocrate R., Leoni S., Lunardi S., Mazurek K., Mengoni D., Michelagnoli C., Million B., Morale A.I., Napoli D.R.,Nicolini R., Pellegri L., Recchia F., Siebeck B., Siem S., Ur C., Valiente-Dobon J.J., Wieland O., Ziębliński M., *Gamma decay of the possible two-phonon 1^- state in ^{140}Ce excited via inelastic scattering of ^{17}O*, Acta. Phys Pol B47, 3, 859 (2016).

[Lan15] Lanza E. G., Vitturi A., and Andrés M. V., *Microscopic nuclear form factors for the pygmy dipole resonance*, Phys. Rev. C 91, 054607 (2015).

[Laz01] Lazarus I., Appelbe E. E., Butler P. A., Coleman-Smith P. J, Cresswell J. R., Freeman S. J., Herzberg R. D., Hibbert I., Joss D. T, Letts S. C., Page R. D., Pucknell V. F. E., Regan P. H., Sampson J, Simpson J., Thornhill J., Wadsworth R, *The GREAT Triggerless Total Data Readout Method*, IEEE Transactions on Nuclear Science NS-48, 567(2001).

[Lip89] Lipparini E. and Stringari S., *Sum rules and giant resonances in nuclei*, Phys. Rep. 175,, 3-4, 103-261, (1989).

[Lit07] Litvinova E, Ring P., and Vretenar D., *Relativistic RPA plus phonon-coupling analysis of pygmy dipole resonances*, Phys. Lett. B 647, 111 (2007).

[Lit08] Litvinova E., Ring P. and Tselyaev V., *Relativistic quasiparticle time blocking approximation: Dipole response of open-shell nuclei*, Phys. Rev. C 78, 014312(2008).

[Lit09a] Litvinova E., Loens H.P., Langanke K, Martinez-Pinedo G., Rauscher T., Ring P., Thielemann F.-K., Tselyaev V., Nucl. Phys. A823, 26-37 (2009).

[Lit09b] Litvinova E, Ring P, Tselyaev V, Langanke K, *Relativistic quasiparticle time blocking approximation. II. Pygmy dipole resonance in neutron-rich nuclei*, Phys. Rev. C 79, 054312 (2009).

[Lit15] Litvinova E., private communication

[Lop04] Lopez-Martens A., Hauschild K., Korichi A., Roccaz J., and Thibaud J.-P., *γ-ray tracking algorithms: a comparison*, Nucl. Instr. And Meth. A 533, 3, 454-466, (2004).

[Mar99] Van der Marel J. and Cederwall B, *Backtracking as a way to reconstruct Compton scattered γ rays*, Nucl. Instr. And Meth. A 437, 2-3, 538-551 (1999).

[Men14] Mengoni D., Dueñas J.A., Assié M., Boiano C., John P.R., Aliaga R.J., Beaumel D., Capra S., Gadea A., Gonzáles V., Gottardo A., Grassi L., Herrero-Bosch V., Houdy T., Martel I., Parkar V.V., Perez-Vidal R., Pullia A., Sanchis E., Triossi A., Valiente Dobón J.J., *Digital pulse-shape analysis with a TRACE early silicon prototype*, Nucl. Instr. and Meth. A 764, 241(2014).

[Moh71] Mohan R., Danos M., Biedenharn L.C., *Three-Fluid Hydrodynamical Model of Nuclei*, Phys. Rev. C 3, 1740(1971).

[Mor77] Morinaga H., *In-Beam Gamma-Ray Spectroscopy* (Elsevier Science Ltd, 1977).

[mgs] http://mgs2005.in2p3.fr/Mgs.php, "Mgs software."

[Nic12] Nicolini R., *Pygmy structures in ^{208}Pb and ^{90}Zr studied with the inelastic scattering of 17O at 20 MeV/u*, PhD thesis, University of Milan (2012).

[Ola06] Olariu A., Desesquelles P., Diarra C., Medina P., Parisel C. and C. S. O. Collaboration, *Pulse shape analysis for the location of the γ-interactions in AGATA*, IEEE Transactions on Nuclear Science, 53, 3, 1028- 1031, (2006).

[Paa05] Paar N., Nikšić T., Vretenar D., Ring P., *Isotopic dependence of the pygmy dipole resonance*, Phys. Lett. B 606, 288 (2005).

[Paa07] Paar N., Vretenar D., Khan E., and Colo G., *Exotic modes of excitation in atomic nuclei far from stability*, Rep. Prog. Phys. 70, 691 (2007).

[Paa09] Paar N., Niu Y. F., Vretenar D., and Meng J., *On the isoscalar-isovector splitting of pygmy dipole structures*, Phys. Rev. Lett. 103, 032502 (2009).

[Pel14a] Pellegri L., Bracco A., Crespi F.C.L., Leoni S., Camera F., Lanza E.G., Kmiecik M., Maj A., Avigo R., Benzoni G., Blasi N., Boiano C., Bottoni S., Brambilla S., Ceruti S., Giaz A., Million B., Morales A.I., Nicolini R., Vandone V., Wieland O., Bazzacco D., Bednarczyk P., Bellato

M., Birkenbach B., Bortolato D., Cederwall B., Charles L., Ciemala M., De Angelis G., Désesquelles P., Eberth J., Farnea E., Gadea A., Gernhäuser R., Görgen A., Gottardo A., Grebosz J., Hess H., Isocrate R., Jolie J., Judson D., Jungclaus A., Karkour N., Krzysiek M., Litvinova E., Lunardi S., Mazurek K., Mengoni D., Michelagnoli C., Menegazzo R., Molini P., Napoli D.R., Pullia A., Quintana B., Recchia F., Reiter P., Salsac M.D., Siebeck B., Siem S., Simpson J., Söderström P.-A., Stezowski O., Theisen Ch., Ur C., Valiente Dobon J.J., Zieblinski M., *Pygmy dipole resonance in ^{124}Sn populated by inelastic scattering of ^{17}O*, Phys. Lett. B 738, 519 (2014).

[Pel14b] Pellegri L., *On the Nature of the Pygmy Dipole Resonance in ^{124}Sn via Inelastic Scattering of ^{17}O,* PhD Thesis, University of Milan (2014).

[Pie99] Pietralla N., *Empirical correlation between two-phonon E1 transition strengths in vibrational nuclei*, Phys. Rev. C 59, 5, 2941 (1999).

[Piek11] Piekarewicz J., *Pygmy resonances and neutron skins*, Phys. Rev. C 83, 034319 (2011).

[Piek12] Piekarewicz J., Agrawal B.K., Colò G., Nazarewicz W., Paar N., Reinhard P.-G., Roca-Maza P.-G., Vretenar D., *Electric dipole polarizability and the neutron skin*, Phys. Rev. C 85, 041302 (2012).

[Pit79] Pittan R., Hass H., Meyer D. H., Buskirk F. R. and Dyer J. N., *Electric dipole polarizability and the neutron skin*, Phys. Rev. C 19, 1251 (1979).

[Pug10] Puglierin G., *Accelerator facilities for pure and applied physics at Legnaro Italian Nuclear Physics National Lab*, Nucl. Phys. A, 834, 1-4, 713c-716c (2010).

[Rei10] Reinhard P.-G., Nazarewicz W., *Information content of a new observable: The case of the nuclear neutron skin*, Phys. Rev. C 81, 051303 (2010).

[Rep13] Repko A., Reinhard P.G., Nesterenko V.O., Kvasil J., *Toroidal nature of the low-energy E1 mode*, Phys Rev C 87, 024305 (2013).

[Rec09] Recchia F., Bazzacco D., Farnea E., Gadea A., Venturelli R., Beck T., Bednarczyk P., Buerger A., Dewald A., Dimmock M., Duchêne G., Eberth J., Faul T., Gerl J., Gernhaeuser R., Hauschild K., Holler A., Jones P., Korten W., Kröll Th., Krücken R., Kurz N., Ljungvall J., Lunardi S., Maierbeck P., Mengoni D., Nyberg J., Nelson L., Pascovici G., Reiter P., Schaffner H., Schlarb M., Steinhardt T., Thelen O., Ur C.A., Valiente-Dobon J.J., Weißhaar D., *Position resolution of the prototype AGATA triplecluster detector from an in-beam experiment*, Nucl. Instr. And Meth. A 604, 3, 555-562 (2009).

[Sar04] Sarchi D., Bortignon P.F., Colò G., *Dipole states in stable and unstable nuclei*, Phys. Lett. B 601, 27 (2004).

[Sat83] Sathler G. R., *Direct Nuclear Reactions*, (Oxford University Press, 1983).

[Sav06] Savran D., Babilon M., van den Berg A. M., Harakeh M. N., Hasper J., Matic A., Wörtche H. J., and Zilges A., *Nature of the Pygmy Dipole Resonance in ^{140}Ce studied in (α,α') experiments*, Phys. Rev. Lett. 97, 172502 (2006).

[Sav13] Savran D., Aumann T., Zilges A., *Experimental studies of the Pygmy Dipole Resonance*, Progress in Particle and Nuclear Physics 70, 210-245 (2013).

[Sch99] Schmid G. J., Deleplanque M.A., Lee I.Y., Stephens F.S., Vetter K., Clark R.M., Diamond R.M., Fallon P., Macchiavelli A.O., MacLeod R.W., *A γ-ray tracking algorithm for the GRETA spectrometer*, Nucl. Instr. And Meth. A 430, 69-83 (1999).

[Sjo84] Sjoreen T. P., Bertrand F. E., Auble R. L., Gross E. E., Horen D. J., Shapira D., Wright and D. B., *Inelastic excitation of giant resonances by 400-MeV 16O*, Phys. Rev. C 29, 4, 1370 (1984).

[Son09] K. Sonnabend, J. Hasper, S. Müller, N. Pietralla, D. Savran, L. Schnorrenberger, A. Zilges, AIP Conf. Proc. 1090, 481(2009).

[Ste75] Steffen R. M. and Alder K., *The Electromagnetic Interaction in Nuclear Spectroscopy* ed J H Hamilton (Angular distributions and correlations of gamma rays) (1975, North Holland)

[Suz90] Suzuki Y., Ikeda K., and Sato H., *New Type of Dipole Vibration in Nuclei*, Prog. Theor. Phys. 83, 180 (1990).

[Tho88] Thompson I. J, *Coupled reaction channels calculations in nuclear physics*, Computer Physics Reports 7 (1988) URL http://www.fresco.org.uk

[Ton10] A.P. Tonchev, S.L. Hammond, J.H. Kelley, E. Kwan, H. Lenske, G. Rusev, W. Tornow, N. Tsoneva, Phys. Rev. Lett. 104, 072501 (2010).

[Tso04] Tsoneva N., Lenske H., and Stoyanov Ch., *Probing the nuclear neutron skin by low-energy dipole modes*, Phys. Lett. B 586, 213 (2004).

[Tso08] Tsoneva N. and Lenske H., *Pygmy dipole resonances in the tin region*, Phys. Rev. C 77, 024321 (2008).

[Uts03] H. Utsunomiya, H. Akimune, S. Goko, M. Ohta, H. Ueda, T. Yamagata, K. Yamasaki, H. Ohgaki, H. Toyokawa, Y.-W. Lui, T. Hayakawa, T. Shizuma, S. Goriely, Phys. Rev. C 67, 015807 (2003).

[Uts06] H. Utsunomiya, P. Mohr, A. Zilges, M. Rayet, Nuclear Phys. A 777, 459 (2006).

[Vet00] Vetter K., Kuhn A., Deleplanque M.A., Lee I.Y., Stephens F.S., Schmid G.J., Beckedahl D., Blair J.J., Clark R.M., Cromaz M., Diamond R.M., Fallon P., Lane G.J., Kammeraad J.E., Macchiavelli A.O., Svensson C.E., *Three-dimensional position sensitivity in two-dimensionally segmented HP-Ge detectors*, Nucl. Instr. And Meth. A 452, 1-2, 223-238 (2000).

[Vol06] Volz S., Tsoneva N., Babilon M., Elvers M., Hasper J., Herzberg R.-D., Lenske H., Lindenberg K., Savran D., Zilges A., *The photoresponse of stable N=82 nuclei below 10 MeV*, Nucl. Phys. A 779, 1–20 (2006).

[Vre01] Vretenar D., Paar N., Ring P. and Lalazissis G. A., *Collectivity of the low-lying dipole strength in relativistic random phase approximation*, Nucl. Phys. A 692, 496 (2001).

[Wie09] O. Wieland, A. Bracco, F. Camera, G. Benzoni, N. Blasi, S. Brambilla, F.C.L. Crespi, S. Leoni, B. Million, R. Nicolini, A. Maj, P. Bednarczyk, J. Grebosz, M. Kmiecik, W. Meczynski, J. Styczen, T. Aumann, A. Banu, T. Beck, F. Becker, L. Caceres, P. Doornenbal, H. Emling, J. Gerl, H. Geissel, M. Gorska, O. Kavatsyuk, M. Kavatsyuk, I. Kojouharov, N. Kurz, R. Lozeva, N. Saito, T. Saito, H. Schaffner, H.J. Wollersheim, J. Jolie, P. Reiter, N. Warr, G. deAngelis, A. Gadea, D. Napoli, S. Lenzi, S. Lunardi, D. Balabanski, G. LoBianco, C. Petrache, A. Saltarelli, M. Castoldi, A. Zucchiatti, J. Walker, A. Bürger, Phys. Rev. Lett. 102, 092502 (2009).

[Wil98] Wilhelm M, Kasemann S., Pascovici G., Radermacher E., von Brentano P., Zilges A*., Two-phonon character of the lowest electric dipole excitation in 142 Nd and in other nuclei near shell closures*, Phys. Rev. C 57, 577 (1998).

[Wur69] Wurm J. P., Heusler A., Von Brentano P., *Generalized neutron particle-hole states in ^{140}Ce*, Nucl. Phys A 128, 2, 433-456 (1969).